



AMERICAN UNIVERSITY OF BEIRUT

A BIOMIMETIC THREE-DIMENSIONAL MODEL OF THE  
BLOOD-BRAIN BARRIER UTILIZING POLYETHYLENE  
GLYCOL HYDROGELS FUNCTIONALIZED WITH  
LAMININ AND FIBRONECTIN MIMETIC PEPTIDES

by  
NESRINE HUSSEIN AHMAD

A thesis  
submitted in partial fulfillment of the requirements  
for the degree of Master of Science  
to the Biomedical Engineering Program  
of the Maroun Semaan Faculty of Engineering and Architecture  
and Faculty of Medicine  
at the American University of Beirut

Beirut, Lebanon  
May 2021

AMERICAN UNIVERSITY OF BEIRUT

A BIOMIMETIC THREE-DIMENSIONAL MODEL OF THE  
BLOOD-BRAIN BARRIER UTILIZING POLYETHYLENE  
GLYCOL HYDROGELS FUNCTIONALIZED WITH  
LAMININ AND FIBRONECTIN MIMETIC PEPTIDES

by  
NESRINE HUSSEIN AHMAD

Approved by:



Digitally signed by Rami Mhanna  
DN: cn=Rami Mhanna, o, ou,  
email=rm136@aub.edu.lb, c=US  
Date: 2021.05.07 14:33:00 +03'00'

---

[Dr. Rami Mhanna, Assistant Professor]  
[Biomedical Engineering Program]  
Maroun Semaan Faculty of Engineering and Architecture

Advisor



---

[Dr. Marwan El-Sabban, Vice Chair, Professor]  
[Department of Anatomy, Cell Biology and Physiological Sciences]  
Faculty of Medicine

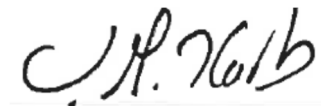
Co-Advisor



---

[Dr. Arij Daou, Assistant Professor]  
[Biomedical Engineering Program]  
Maroun Semaan Faculty of Engineering and Architecture

Member of Committee



---

[Dr. Mohammad Harb, Assistant Professor]  
[Department of Mechanical Engineering]  
Maroun Semaan Faculty of Engineering and Architecture

Member of Committee

Date of thesis defense: May 4, 2021

# AMERICAN UNIVERSITY OF BEIRUT

## THESIS RELEASE FORM

Student Name: \_\_\_\_\_ Ahmad \_\_\_\_\_ Nesrine \_\_\_\_\_ Hussein \_\_\_\_\_  
Last First Middle

I authorize the American University of Beirut, to: (a) reproduce hard or electronic copies of my thesis; (b) include such copies in the archives and digital repositories of the University; and (c) make freely available such copies to third parties for research or educational purposes:

- As of the date of submission
- One year from the date of submission of my thesis.
- Two years from the date of submission of my thesis.
- Three years from the date of submission of my thesis.



May 10, 2021

---

Signature

Date

## ACKNOWLEDGEMENTS

In the Name of Allah, the Most Beneficent, the Most Merciful

First and foremost, I would like to thank Allah (swt) for his countless blessings throughout my life.

It is a genuine pleasure to express my profound gratitude to my advisor, Dr. Rami Mhanna, for his guidance and encouragement throughout this journey.

My sincere thanks go to my co-advisor, Dr. Marwan El-Sabban, for his valuable guidance and support, also for allowing me to complete this work in his lab.

I would like to further thank Dr. Arij Daou and Dr. Mohammad Harb for serving as my committee members.

A word of appreciation goes to my research mentor, John Saliba, as I am grateful for his day-to-day help and support along his journey. Many thanks go to all my friends and colleagues in Dr. Rami's and Dr. Sabban's labs.

To my parents, a million thanks for your love and guidance throughout my life. Thank you for giving me the opportunity and strength to chase my dreams. I am forever grateful for you. To my brothers, your love and support have always been appreciated. Lastly, my close friends deserve a wholehearted thanks as well.

# ABSTRACT OF THE THESIS OF

Nesrine Hussein Ahmad

for

Master of Science

Major: Biomedical Engineering

Title: A Biomimetic Three-Dimensional Model of the Blood-Brain Barrier Utilizing Polyethylene Glycol Hydrogels Functionalized with Laminin and Fibronectin Mimetic Peptides

The blood-brain barrier (BBB) is the unique microvasculature of the brain that regulates the flow of molecules between the circulating blood and the brain by tightly controlled mechanisms. Disruption of the BBB has been associated with several neurological diseases which encouraged the development of biomimetic *in vitro* BBB models for basic and applied investigations. Current *in vitro* models fail to resemble the cellular, molecular, and dimensionality aspects of the *in vivo* BBB milieu and consequently cannot be faithfully used to understand its functions and activity. In the current thesis, we engineered a three-dimensional (3D) co-culture system utilizing polyethylene glycol (PEG) hydrogels functionalized with brain-mimetic laminin and fibronectin peptides. PEG hydrogels were modified with different concentrations of laminin-mimetic IKVAV, fibronectin-mimetic RGD peptides, and combinations thereof, and then chemically crosslinked with matrix metalloprotease sensitive peptides via a Michael type-addition. Astrocytes were encapsulated within the hydrogel, whereas endothelial cells (ECs) were seeded on the surface to resemble the *in vivo* endothelium. The viability of encapsulated astrocytes was assessed via a Live/Dead assay. Barrier integrity and tight junction formation were evaluated qualitatively by immunostaining for ZO-1 tight junction protein, and quantitatively by measuring TEER and permeability of sodium fluorescein and Evan's blue bound to albumin tracers. The activity of astrocytes was assessed by GFAP immunohistochemistry. PEG hydrogels modified with 300  $\mu\text{M}$  IKVAV promoted the highest viability of astrocytes but failed to enable EC adherence. However, PEG hydrogels functionalized with both RGD and IKVAV (300  $\mu\text{M}$ :300  $\mu\text{M}$ ), or 600  $\mu\text{M}$  RGD solely induced cell attachment and monolayer formation. PEG hydrogels functionalized with RGD and IKVAV (300  $\mu\text{M}$ :300  $\mu\text{M}$ ) with encapsulated astrocytes and seeded ECs had a statistically higher TEER ( $55.33 \pm 1.47 \Omega \cdot \text{cm}^2$  at day 5), compared to other 3D and 2D controls ( $p\text{-value} \leq 0.001$ ). Evan's blue permeability at 120 mins ( $0.215 \pm 0.055 \mu\text{g/mL}$ ) was lowest in this condition, while the permeability of sodium fluorescein did not change significantly ( $p\text{-value} > 0.05$ ). ZO-1 expression showed a relatively more defined network in functionalized PEG hydrogels with encapsulated astrocytes compared to the 3D and 2D controls, while GFAP expression did not vary. PEG hydrogels functionalized with laminin and fibronectin mimetic peptides present a biomimetic tool to assess the efficiency of drug delivery for the treatment of neurological diseases and to understand the role of cell-cell and cell-matrix interactions on the BBB properties.

Keywords: Blood-Brain Barrier (BBB), Polyethylene Glycol (PEG), Laminin, IKVAV, Fibronectin, RGD, 3D, Hydrogel

## TABLE OF CONTENTS

ACKNOWLEDGEMENTS .....	1
ABSTRACT .....	2
ILLUSTRATIONS .....	5
TABLES.....	8
ABBREVIATIONS.....	9
INTRODUCTION.....	12
LITERATURE REVIEW .....	16
1. Overview of Neurological Diseases .....	16
1.1 Overview of Alzheimer’s Disease .....	16
1.2 Causes of Alzheimer’s Disease.....	17
2. The Blood-Brain Barrier (BBB) .....	18
2.1 The Building Blocks of the Blood-Brain Barrier.....	19
2.2 Perturbations of the Blood-Brain Barrier.....	29
3. Bio-mimicking the Blood-Brain Barrier.....	32
4. Hydrogels.....	36
4.1 Polyethylene Glycol (PEG) .....	38
RATIONAL AND HYPOTHESIS.....	41
MATERIALS AND METHODS .....	44

1.	Materials .....	44
2.	Methods .....	45
2.1	Fabrication of 4% PEG Hydrogels .....	45
2.2	Co-culturing of Endothelial Cells and Astrocytes .....	48
2.3	LIVE/DEAD Assay .....	53
2.4	Transendothelial Electrical Resistance (TEER) Measurement.....	56
2.5	Permeability Assay .....	59
2.6	Immunofluorescence Staining for ZO-1 and GFAP.....	62
3.	Statistical Analysis.....	66
<b>RESULTS AND DISCUSSION.....</b>		<b>67</b>
1.	Optimization of the PEG Hydrogels Functionalized with IKVAV .....	67
2.	Seeding of Endothelial Cells.....	73
3.	Transendothelial Electrical Resistance (TEER) .....	75
4.	Permeability Assay .....	77
5.	ZO-1 and GFAP Characterization .....	82
<b>CONCLUSION .....</b>		<b>88</b>
<b>REFERENCES .....</b>		<b>91</b>



## ILLUSTRATIONS

### Figure

1. Schematic illustration of the BBB [49].....	19
2. Schematic illustration of the BM assembly [24]. .....	24
3. Schematic illustration of the BM [123]. .....	29
4. Schematic illustration comparing the permeability across a healthy BBB vs. a diseased BBB [121]. .....	31
5. Schematic illustration of the developed static <i>in vitro</i> models to bio-mimic the BBB. <b>[A]</b> Monoculture of ECs on a porous membrane. <b>[B]</b> Non-contact co-culture of ECs on the inner side of the porous membrane and astrocytes on the bottom side of the well. <b>[C]</b> Contact co-culture of ECs on the inner side of the porous membrane and astrocytes on the bottom side of the porous insert. <b>[D]</b> Triple culture of ECs on the inner side of the porous insert, pericytes on the bottom side of the porous insert, and astrocytes on the bottom side of the well [30].....	34
6. Schematic illustration of the microfluidic BBB model [33]. .....	36
7. Schematic illustration of the polymerization process [166]. .....	39
8. Four-arm polyethylene glycol-vinyl sulfone (PEG-VS) polymer [171].....	40
9. Schematic illustration of the fabricated model. ....	42
10. Crosslinking PEG-VS with MMP-sensitive peptides via a Michael-type addition reaction.....	46
11. Schematic illustration of the PEG hydrogel fabrication process and astrocytes encapsulation. ....	50
12. Schematic illustration of <b>[A]</b> Astrocyte's encapsulation inside the PEG hydrogel <b>[B]</b> ECVs seeding on the PEG hydrogels with embedded NHA. ....	53
13. Illustration of the Live/Dead staining of NHAs embedded in the functionalized PEG hydrogels at different IKVAV concentrations (75, 150, 300, and 600 mM) at days 1,4, and 7 post hydrogel fabrication. ....	55
14. Schematic illustration of the TEER measurement system.....	57
15. Schematic illustration of electrodes positioning during TEER measurement [178].....	58
16. Schematic illustration of the permeability assay. ....	60
17. Schematic illustration of the ZO-1 and GFAP indirect immunofluorescences staining.....	63

18. Schematic illustration of the undirect immunofluorescence workflow [1]. ..... 66
19. Live/dead assay of NHA embedded in 4% PEG with different IKVAV concentrations (75  $\mu$ M, 150  $\mu$ M, 300  $\mu$ M, and 600  $\mu$ M) at days 1, 4, and 7. Live NHA were stained with Calcein-AM (Green). Dead NHA were stained with EthD-1 (Red). Images were taken using a confocal microscope with a 10X objective. Scale bar=100  $\mu$ m, (n=3). ..... 68
20. Percentage Viability (%) of NHA embedded in 4% PEG hydrogels functionalized with different IKVAV concentrations (75, 150, 300, and 600  $\mu$ M) at days 1, 4, and 7. No statistical significance found ( $p$ -value> 0.05). Error bars represent +/- SEM, (n=3). ..... 69
21. Number of Live NHA embedded in 4% PEG hydrogels functionalized with different IKVAV concentrations (75, 150, 300, and 600  $\mu$ M) at days 1, 4, and 7. No statistical significance was found ( $p$ -value> 0.05). Error bars represent +/- SEM, (n=3). ..... 70
22. A 3D 4% PEG hydrogel functionalized with [A] 75  $\mu$ M [B] 150  $\mu$ M [C] 300  $\mu$ M [D] 600  $\mu$ M laminin-mimetic peptide IKVAV. Astrocytes were embedded inside the hydrogel. Live NHAs were stained with Calcein-AM (Green). Dead NHA were stained with EthD-1 (Red). Z-stack images were taken using a confocal microscope with a 10X objective. Scale bar=100  $\mu$ m, (n=3). ..... 72
23. ECVs seeded on top of PEG hydrogel functionalized with [A] IKVAV-300  $\mu$ M [B] RGD-600  $\mu$ M [C] IKVAV:RGD-300. ECVs did not adhere when IKVAV was solely incorporated (Image A). ECVs adhered and formed a monolayer when RGD was solely (B) and combined with IKVAV (C). Images were taken using an inverted light microscope. Scale bar=1000  $\mu$ m, (n=3). ..... 74
24. Corrected TEER values ( $\Omega$ .cm<sup>2</sup>) for different samples recorded at days 1 to 5 using EVOM2 and STX2 electrodes. One-way ANOVA analysis was performed to determine the statistical difference between TEER at days 1 and 5 of each condition. One-way ANOVA was also performed to detect any statistically significant difference in TEER of different samples at day 5. TEER of IKVAV:RGD-300  $\mu$ M with encapsulated NHA was significantly higher than the other samples. TEER of functionalized PEG hydrogels controls was significantly higher than the 2D monoculture and co-culture controls.  $P$ -value  $\leq$  0.05 was considered significant.  $P$ -value  $\leq$  0.001 was marked with (\*\*\*). Error bars represent +/- SEM, (n=3). ..... 77
25. EBA Permeability Assay: Log10 concentration of the Evan's Blue Bound to Albumin (EBA;  $\mu$ g/mL) under different functionalized PEG conditions at four time-points (30, 60, 90, and 120 mins). Two-way ANOVA analysis was performed to determine any statistical difference between the same sample at 30 mins and 120 mins; and at a particular time-point for all PEG hydrogels relative to 8  $\mu$ m blank, monoculture and co-culture relative to each other and the 0.4  $\mu$ m blank, samples with/without NHA, IKVAV:RGD-300  $\mu$ M, and RGD-600  $\mu$ M. Functionalized PEG hydrogels (with/without astrocytes) showed a significantly

- lower EBA permeability. P-value  $\leq 0.05$  was considered significant. P-value  $\leq 0.001$  was marked with (\*\*\*) . Error bars represent +/- SEM, (n=2)..... 80
26. Na-F Permeability Assay: Log10 concentration of the Sodium Fluorescein (Na-F; ng/mL) under different functionalized PEG conditions at four time-points (30, 60, 90, and 120 mins). Two-way ANOVA analysis was performed to determine any statistical difference between the same sample at 30 mins and 120 mins; and at a particular time-point for all PEG hydrogels relative to 8  $\mu\text{m}$  blank, monoculture and co-culture relative to each other and the 0.4  $\mu\text{m}$  blank, samples with/without NHA, IKVAV:RGD-300  $\mu\text{M}$ , and RGD-600  $\mu\text{M}$ . P-value  $\leq 0.05$  was considered significant. P-value  $\leq 0.001$  was marked with (\*\*\*) . Error bars represent +/- SEM, (n=2). ..... 82
27. ZO-1 staining of ECVs in **[A]** ECV monoculture control; negative control **[B]** ECV and NHA co-culture control **[C]** RGD-600  $\mu\text{M}$  control **[D]** IKVAV:RGD-300  $\mu\text{M}$  control **[E]** RGD-600  $\mu\text{M}$  with encapsulated astrocytes **[F]** IKVAV:RGD-300  $\mu\text{M}$  with encapsulated NHA. Images were taken using a confocal laser scanning microscope (63x). Scale bar=10  $\mu\text{m}$ , (n=2). ..... 85
28. ZO-1/DAPI intensity ratio of each condition quantified using ImageJ. Functionalized PEG hydrogels with encapsulated astrocytes show the highest intensity. One-way ANOVA analysis was used to determine any statistical difference in ZO-1/DAPI intensity between samples. Results show that IKVAV:RGD-300  $\mu\text{M}$  and RGD-600  $\mu\text{M}$  (with/without astrocytes) had a significantly greater expression of ZO-1/DAPI compared to 2D controls. IKVAV:RGD-300  $\mu\text{M}$  and RGD-600  $\mu\text{M}$  with encapsulated NHA had a significantly greater expression of ZO-1/DAPI compared to 2D and 3D controls. P-value  $\leq 0.05$  was considered significant (\*). P-value  $\leq 0.001$  was marked with (\*\*\*) . Error bars represent +/- SEM. .... 86
29. GFAP immunostaining of NHA in **[A]** IKVAV:RGD-300  $\mu\text{M}$  with encapsulated NHA **[B]** RGD-600  $\mu\text{M}$  with encapsulated astrocytes **[C]** ECV and NHA co-cultured on insert. Images were taken using a confocal laser scanning microscope (63x). Scale bar=10  $\mu\text{m}$ , (n=2). ..... 87
30. GFAP/DAPI intensity ratio of each condition quantified using ImageJ. No difference was found between samples. No significant difference was detected. Error bars represent +/- SEM. .... 87

## TABLES

### Table

31. Preparation of 4% PEG-IKVAV hydrogels with different concentrations of IKVAV peptide ( $V_{\text{total}}=100 \mu\text{L}$ ). .....	47
32. Statistical analysis convention followed by GraphPad Prism 9. ....	66

## ABBREVIATIONS

### **A:**

ABM: Astrocytes Basal Medium

AD: Alzheimer's Disease

### **B:**

BBB: Blood-Brain Barrier

BCECs: Brain Capillary Endothelial Cells

BM: Basement Membrane

BSA: Bovine Serum Albumin

bFGF: Basic Fibroblast Growth Factor

### **C:**

CAA: Cerebral Amyloid Angiopathy

CNS: Central Nervous System

### **D:**

DAPI: 4',6-diamino-2-phenylindole, dihydrochloride

DMEM: Dulbecco's Modified Eagle's Medium

DDW: Double Distilled Water

DW: Distilled Water

### **E:**

EBA: Evan's Blue-Albumin

EC: Endothelial Cells

ECM: Extracellular Matrix

ECV: Immortalized Human Aortic Endothelial Cells

EthD-1: Ethidium Homodimer

EVOM2: Electronic Voltohmmeter

**G:**

GDNF: Glial-Derived Neurotrophic Factor

GFAP: Glial Fibrillary Acidic Protein Antibody

**H:**

hMSC: Human Mesenchymal Stem Cells

HSPG: Heparan Sulfate Proteoglycan

**I:**

IKVAV: Isoleucine-Lysine-Valine-Alanine-Valine Peptide

IKVAV-75  $\mu$ M: PEG Hydrogels Functionalized with 75  $\mu$ M IKVAV

IKVAV-150  $\mu$ M: PEG Hydrogels Functionalized with 150  $\mu$ M IKVAV

IKVAV-300  $\mu$ M: PEG Hydrogels Functionalized with 300  $\mu$ M IKVAV

IKVAV-600  $\mu$ M: PEG Hydrogels Functionalized with 600  $\mu$ M IKVAV

IKVAV:RGD-300  $\mu$ M: PEG Hydrogels Functionalized with IKVAV and RGD  
(300 $\mu$ M:300 $\mu$ M)

**J:**

JAMs: Junctional Adhesion Proteins

**M:**

MMP: Matrix Metalloprotease

**N:**

Na-F: Sodium Fluorescein

NHA: Normal Human Astrocytes

NGS: Normal Goat Serum

NVU: Neurovascular Unit

**P:**

PBS: Phosphate Buffer Saline

PEG: Polyethylene Glycol

PEG-VS: Polyethylene Glycol-Vinyl Sulfone

PFA: Paraformaldehyde

PLL: Poly-L-Lysine

PNS: Peripheral Nervous System

**R:**

RGD: Arginine-Glycine-Aspartic Acid Peptide

RGD-600  $\mu$ M: PEG Hydrogels Functionalized with 600  $\mu$ M RGD

RPMI: Roswell Park Memorial Institute Medium

**T:**

TE: Trypsin

TEER: Transendothelial Electrical Resistance

TEOA: Triethanolamine

TGF- $\beta$ : Transforming Growth Factor-B

TJ: Tight Junctions

TRED: Texas Red

**W:**

WHO: World Health Organization

**Z:**

ZO-1: Zonula Occludens-1

ZO-2: Zonula Occludens-2

ZO-3: Zonula Occludens-3

# CHAPTER I

## INTRODUCTION

Neurological disorders are chronic diseases that affect over 1 billion individuals globally. Nearly 1 out of 6 people suffer from at least one neurological disease [2, 3]. With the increase in life expectancy, the rate of people with neurological diseases is predicted to significantly increase in the coming years [4]. Several neurological disorders, such as stroke, Alzheimer's Disease (AD), multiple sclerosis, and brain tumor metastasis, have been associated with disruption of the blood-brain barrier (BBB). For example, BBB breakdown has been detected in the early stages of AD in which amyloid  $\beta$ -peptide accumulates in the central nervous system (CNS) [5-7].

In brief, the BBB is a highly selective dynamic interface that separates the brain from the circulatory system. It protects the brain by isolating it from the surrounding environment. The BBB further maintains the CNS homeostasis by controlling the flow of molecules between the two systems and preventing the flux of toxins and pathogens [8, 9]. A complex and well-developed network of cells and molecules, defined as the neurovascular unit (NVU), interact to generate and maintain a healthy BBB [10]. Specifically, each component uniquely contributes to the maintenance of the BBB integrity [11]. As such, the downregulation of any of the major components of the BBB initiates pathogenesis [12]. Having said that, the BBB is primarily composed of endothelial cells (ECs), pericytes, astrocytes, and a basement membrane (BM) [8].

Brain capillary endothelial cells (BCECs) are joined together by tight junctions (TJs) to form a tight monolayer, known as the endothelium [13]. The assembled TJs act as a physical barrier by restricting the paracellular flow of molecules across the endothelium and into the brain. TJs also polarize the BCECs to further control the



transcellular flow of molecules between the apical and basal sides of the endothelium [14]. The transcellular flow is characterized by specialized transports and efflux pumps located on the apical side. While small lipophilic molecules and gases (i.e. O<sub>2</sub> and CO<sub>2</sub>) can diffuse across the endothelium, small hydrophilic molecules can only pass into the brain via these specialized transporters. Accordingly, this forms a transport barrier that enables the influx of the required nutrients and molecules only [15, 16]. The BBB restricts the access of all large-molecule drugs and 98% of small molecule drugs issuing a major challenge in CNS pharmacotherapy [17]. On the other hand, efflux pumps are responsible for wastes removal, as well as prevent the passage of neurotoxins, pathogens, and cells into the brain [18]. This is supported by the activation of intracellular and extracellular enzymes that degrade neurotoxins and metabolize peptides, respectively [8, 19].

Astrocytes, defined as specialized star-shaped glial cells, interact via their endfeet with the ECs and BM molecules to maintain the BBB's integrity [20]. Specifically, astrocytes secrete soluble factors that enhance the expression of TJ proteins, reflecting their role in increasing the tightness of the BBB. Astrocytic endfeet line the majority of the endothelium, emphasizing their crucial role in regulating the BBB [10, 21]. Similarly, pericytes interact with astrocytes, ECs, and BM molecules to maintain the BBB integrity [22, 23].

The BM is the unique ECM surrounding the endothelium. It is described as a highly organized protein network composed primarily of laminin, fibronectin, and collagen-IV. The various cellular interactions occurring in the BBB, primarily between astrocytes, ECs, and pericytes, synthesize and deposit the major ECM proteins, forming the BM [24]. In turn, the BM peptides interact with the cells to promote cellular

adhesion, growth, migration and signaling. It also serves as structural support for the endothelium as these peptides indirectly upregulate the expression of TJs [25-28]. Accordingly, there exists a bidirectional relation between the BBB cells and the BM, where the proteins secreted by the cells of the BBB further interact to induce and maintain the integrity of the BBB [6, 29]. Therefore, any perturbation in the composition or interactions of the BBB will affect its permeability. Understanding how the different components of the BBB functions and the impairments that may happen, is crucial for developing accurate diagnostic techniques, and effective targeted drugs for neurological disorders.

To understand the BBB in physiology and pathophysiology, several approaches were followed to recapitulate the complex aspects of the BBB. While *in vivo* models are favored in studying pharmacokinetics under a natural complexity, results have shown that 50% of the testing results are inconsistent with human responses. Such outcome is expected due to the differences in the BBB across different species. *In vivo* models are also limited as they are expensive low throughput screening assays that spark a major ethical concern [30, 31]. For this reason, *in vitro* models were considered as promising substitutes for *in vivo* testing.

In an attempt to study the BBB *in vitro*, pure and intact rat brain capillaries were isolated [32]. Primary rat BCECs were then isolated from the rat brain capillaries, and monocultures were seeded onto porous inserts. This approach failed to resemble the BBB's dimensionality, cell-cell and cell-matrix interactions, and cell and molecular complexity. While co-culturing rat-derived BCEC and astrocytes on porous inserts slightly enhanced the tightness, the planar dimensionality and absence of the BM molecules remained a major disadvantage of this model. Dynamic *in vitro* models

relatively enhanced the tightness and decreased the permeability of the model.

However, such approaches did not overcome the previously mentioned limitations of the static models such as dimensionality, and cell and matrix biomimicry [33].

Hydrogels, defined as hydrophilic three-dimensional (3D) networks of crosslinked polymer chains, are often used in biomedical applications [34]. Their significant water content resembles that of natural tissues, where water constitutes up to 60% of the human body [35]. Hydrogels are specifically used in tissue engineering as they are flexible and reproducible scaffolds [36]. Polyethylene glycol (PEG), described as an inert synthetic polymer, is commonly used in the field of neural tissue engineering as it is biodegradable, biocompatible, and inexpensive [37, 38]. Specifically, 4-arm PEG-vinyl sulfone (PEG-VS), a more reactive modified version of PEG, has shown to have greater hydrolytic stability, lower immunogenicity, successful cell encapsulation during gelation, and ability to be modified with biological motifs, such as arginine-glycine-aspartate tripeptide (RGD), a fibronectin-mimetic peptide [39]. As such, functionalized PEG-VS hydrogel can be considered as a promising scaffold for developing an *in vitro* BBB model.

## CHAPTER II

### LITERATURE REVIEW

#### **1. Overview of Neurological Diseases**

Neurological diseases, such as Alzheimer's, Parkinson's, multiple sclerosis, stroke, and cancer, are chronic diseases that affect over 1 billion individuals globally. Nearly 1 out of 6 people suffer from at least one neurological disease [2, 3]. According to the World Health Organization (WHO), 50 million individuals suffer from dementia, with around 10 million newly diagnosed cases annually [40]. Specifically, 60-70% of these cases suffer from Alzheimer's disease (AD), the most common form of dementia [41-43].

##### ***1.1 Overview of Alzheimer's Disease***

According to the National Institute of Aging, AD is a progressive irreversible neurodegenerative disease that occurs when the brain nerve cells die [44]. This in turn causes deterioration in the cognitive function of patients such as memory, thinking, and behavior. The loss in brain mass, visualized by CT scans, can be correlated to this decline. Although AD does not cause death, it severely damages the brain as it affects the basic body functions, such as breathing and swallowing, leading to death. According to the Alzheimer's Association, more than 120 thousand patients died from AD in the USA in 2018, making it the sixth leading cause of death [43]. Worldwide, AD ranked as the seventh leading death cause in 2019 [45]. While the death rates of stroke, heart disease, and HIV decreased over the past 20 years, the reported death rate of AD increased by 146.2% [45]. Due to the increasing life expectancy, and other health and

socio-economic factors, the rate of people with AD is predicted to increase significantly over the years. By year 2050, dementia is estimated to affect 152 million individuals worldwide [5, 6, 40, 43].

### ***1.2 Causes of Alzheimer's Disease***

While the direct AD leading factor remains unknown, scientists suspect that a combination of age-related, genetic, environmental, and lifestyle factors, causes AD. The National Institute of Aging further suggests that the neuroinflammatory responses and abnormal protein deposits in the brain are critical factors of AD initiation. AD is characterized by the pathological accumulation of amyloid  $\beta$ -peptide in the CNS, the presence of neurofibrillary tangles containing hyperphosphorylated tau filaments, chronic brain inflammation, and cerebrovascular changes that lead to cerebral amyloid angiopathy (CAA). CAA is a major contributor to AD pathogenesis and progression through the accumulation of amyloid proteins on the walls of arteries [5, 7, 24, 42].

Interestingly, BBB breakdown is detected in the early stages of AD. This causes disruptions in the TJs and interruptions in the expression of transport proteins, such as GLUT1, leading to altered brain permeability. Consequently, this will lead to the acclimation of free radicals and neurotoxins in the brain, cerebral hypoperfusion, and neuroinflammatory responses. Under physiological conditions, the BBB regulates the flow of plasma-derived amyloid  $\beta$ -peptide into the CNS and the removal of the brain-derived amyloid  $\beta$ -peptide through specialized receptors. Yet, in a pathological state, these processes are deregulated leading to the accumulation of amyloid  $\beta$ -peptide in the brain and cerebral blood vessels. In previous studies, AD patients recorded increased levels of amyloid  $\beta$ -peptide in the brain [5-7]. The process of deregulation of the BBB

and the deposition of the amyloid  $\beta$ -peptide are currently poorly understood due to the limited knowledge about the complex structure of the BBB.

## **2. The Blood-Brain Barrier (BBB)**

The BBB is the unique dynamic microvasculature of the CNS. It is a highly selective semipermeable interface separating the brain from the circulatory system [8, 9]. The BBB plays a major role in the proper neural functioning by protecting the brain. The BBB phenotype develops under the collective influence of cells, molecules, and specialized transport mechanisms [46]. The NVU, defined as the group of closely related cells and surrounding components, operates in coordination and precision to maintain the proper functioning of the BBB [10]. The NVU constitutes of vascular cells, mainly ECs and pericytes, glial cells, such as astrocytes, microglia, and oligodendroglia, in addition to neurons and the surrounding matrix [8, 47]. Every component of the NVU contributes to the induction and maintenance of the BBB [11]. The downregulation of any component leads to the disruption of the tight BBB, leading to neurological disorders [12]. Developing targeted drugs for a specific neurological disease will require a thorough understanding of the disease-causing atrophy [21, 46]. Although the BBB is crucial for maintaining CNS homeostasis, the highly controlled and tight nature hinders the drug delivery to the CNS [6, 48].

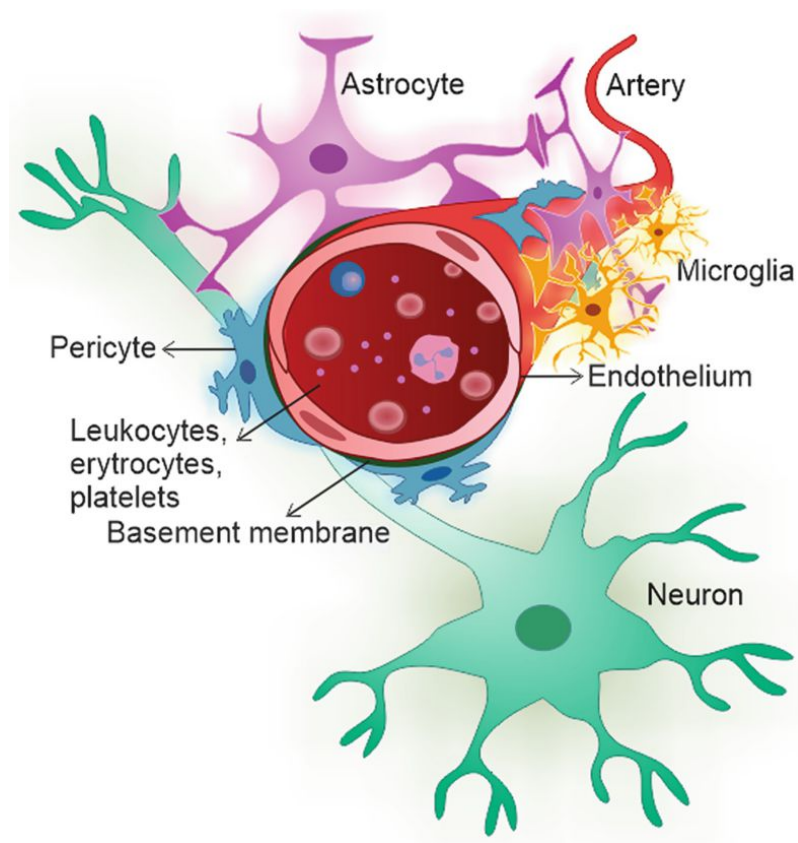


**Figure 1:** Schematic illustration of the BBB [49].

## ***2.1 The Building Blocks of the Blood-Brain Barrier***

### **a. Endothelial Cells**

The BBB is mainly composed of BCECs, astrocytes, pericytes, and a BM [9]. The restrictive nature of the BBB is attributed to the various interactions of these functional components. Specifically, ECs are held together by TJs to form a unique specialized monolayer called the endothelium [13]. TJs are plasma membrane multiprotein complexes that form a continuous impermeable barrier between two adjacent ECs. The transmembrane proteins claudins, occludins, and tricellulin interact and form tight junction strands that maintain and develop the TJs [46, 47]. Also, junctional adhesion proteins (JAMs) play a role in both the assembly of these strands and ECs polarization [13, 50]. Peripheral proteins, such as zonula occludins (ZO-1, ZO-

2, and ZO-3) interact with the transmembrane proteins to further organize and modulate the TJs [8, 13]. Accordingly, the downregulation of any of these proteins is associated with the breakdown of the BBB via disrupting the integrity of the endothelium [51].

Once the TJs are generated between adjacent ECs, the formed endothelium will develop specific transport systems to control the influx of energy and nutrients into the brain, and the efflux of metabolic wastes out of the brain [13, 52]. Specifically, the TJs act as a physical barrier that restricts the paracellular transport of ions, hydrophilic molecules, and cells across this endothelium and into the brain [14]. The TJs of the BBB are more complex than the peripheral TJs as they significantly limit the paracellular flow of molecules, even small ions such as  $\text{Na}^+$  and  $\text{Cl}^-$  [8, 51, 53]. On the contrary, most molecules move paracellularly in the peripheral endothelia. Flow across the BBB is mostly confined to transcellular flow. TJs further trigger the polarization of the BCECs, a critical trait for regulating the transport of molecules between the apical and basal sides of the cells via establishing a barrier and maintaining directionality [6, 14, 50, 51, 54].

The transcellular transport is mediated by specialized transporters and efflux pumps, located on the apical side of the BCEC. Small lipophilic molecules (<400 Da), in addition to small gaseous molecules such as  $\text{O}_2$  and  $\text{CO}_2$ , can easily diffuse through the lipid membranes [15]. Small polar molecules required for the proper functioning of the brain are rather transported by specific carriers [16]. Although large hydrophilic molecules are transported across peripheral endothelia via transcytosis, the BBB endothelium has a much lower degree of transcytosis. Certain peptides are transported by a receptor-mediated system, else-wise such large molecules cannot cross a healthy BBB [15, 16]. Accordingly, such a transport system forms a selective transport barrier



that facilitates the influx of required nutrients only and maintains the ionic composition required for neural synaptic signaling. Besides waste removal, efflux pumps enable the outflow of lipophilic molecules, potential neurotoxins, pathogens, and cells into the brain [18]. However, the high expression of efflux pumps and limited transport act as pharmaceutical constraints by hindering the flow of drugs into the brain [52]. Studies have shown that AD patients have a decreased expression of efflux pumps, contributing to the accumulation of amyloid  $\beta$ -peptide in the brain [24, 51, 55].

A third constraint is a metabolic barrier composed of a combination of intracellular and extracellular enzymes. Intracellular enzymes are capable of inactivating neurotoxins, whereas extracellular enzymes metabolize ATP and peptides. Consequently, the BBB greatly controls the flow and exchange of molecules between the two interfaces: the brain and the blood capillaries. This mechanism supplements the brain with the needed molecules only while facilitating the removal of wastes and toxins [8, 19, 51, 56, 57].

The distinguishable properties of the BCECs compared to peripheral ECs explain the unique barrier integrity of the BBB. The previously mentioned characteristics of the BCECs significantly increase the BBB's electrical resistance, a reflective measure of the barrier permeability. High electrical resistance across a membrane reflects the low flow of ions across it. Indeed, the BBB's high resistance and low permeability resemble that of the epithelial membranes and not peripheral endothelia [42, 58, 59]. The electrical resistance across the BBB's endothelium is in the range of 1500-2000  $\Omega \cdot \text{cm}^2$ , where peripheral endothelia have a resistance of 3-33  $\Omega \cdot \text{cm}^2$ . [59, 60] Besides the abundance of TJs and the expression of specialized transporters in the BBB's endothelium, the BCECs lack any fenestrations, a trait usually

observed in peripheral ECs [61]. Lack of fenestration does not only enhance the barrier function but also increases the cell's mitochondria to further amplify energy production and reduce pinocytosis [51, 62]. Although all of these internal factors (TJs, transporters, enzymes, and cell morphology) greatly support the barrier's integrity, external factors, such as astrocytes and ECM proteins, play a crucial role in further maintaining this barrier.

b. Astrocytes

The BBB is a dynamic structure, greatly influenced by the surrounding cell interactions and ECM signaling. All BBB constituents contribute to its normal functioning and stability. While the specialized endothelium is thought to be behind the BBB's great tightness, astrocytic endfeet enclosing the brain capillaries play a crucial role in supporting the BBB's structural integrity.

Astrocytes are specialized star-shaped glial cells abundantly found in the CNS [20]. Through extending their endfeet, astrocytes interact with the basement membrane surrounding the BBB's endothelium. It has been estimated that 80% to 99% of the basement's membrane surface area is covered by the astrocytic endfeet, reflecting their crucial role in regulating the BBB [21]. The broad role of astrocytes is to protect the brain and maintain neuronal signaling and synapses. Astrocytes secrete soluble factors such as glial-derived neurotrophic factor (GDNF), transforming growth factor- $\beta$  (TGF- $\beta$ ), and basic fibroblast growth factor (bFGF). Collectively, these factors boost the formation of TJs, promote specialized barrier-promoting enzyme systems, and polarize endothelial transporters [10, 21, 50, 63]. Accordingly, astrocytes induce the unique phenotype of BCECs to upregulate the physical, metabolic, and transport barrier

functions. While astrocytes massively contribute to the maintenance of a healthy BBB, they are not the sole regulators where other factors are needed to preserve the barrier integrity.

c. Pericytes

Pericytes are mural cells lining the abluminal side of the BBB's endothelium. This coverage is much higher than any other peripheral tissue [64]. It is thought that pericytes interact with astrocytes and ECs to further support the BBB's early formation and integrity [22, 23]. Pericytes communicate with surrounding astrocytes to induce their polarization and extension of processes, while they interact with BCECs to secrete certain proteins. The deficiency in pericytes increases the permeability of the BBB, by allowing the crossing of large molecules (i.e. immunoglobulins) via transcytosis [22, 65]. As previously mentioned, this mechanism is very limited in the BBB's endothelium, suggesting the role of pericytes in maintaining the tightness of the abluminal side of the endothelium [66]. It has also been found that pericytes enhance the tightness of the BBB by inducing the expression of occludin TJ proteins and improving the assembly of TJs [51, 67].

d. Basement Membrane (BM)

The basement membrane (BM) is a unique form of ECM surrounding the microvasculature. In the BBB, there exist two types of BM: Endothelial BM and Parenchymal BM, separated by pericytes [29]. Under physiological conditions, these two layers are indistinguishable and appear as a single thin sheet-like structure with highly organized protein networks. The complex and heterogeneous macromolecular

network is mainly composed of water and various proteins. The different cell interactions induced in the BBB, primarily between astrocytes, ECs, and pericytes, synthesize and deposit the major ECM proteins, forming the BM. Proteins, such as laminin, fibronectin, and collagen IV, form crosslinked heterogeneous networks connected by nidogen and heparan sulfate proteoglycans (HSPGs; Argin and Perlecan) [24]. Briefly, after the laminins self-assemble into a sheet, nidogen and HSPGs first bind to laminin and then are linked to collagen IV [68]. This stabilizes and supports the formed sheet-like structure [51, 69].

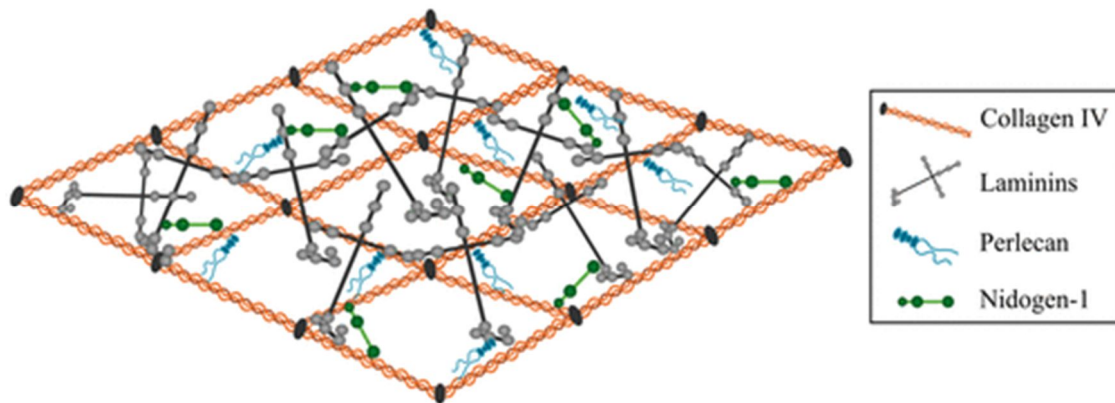


**Figure 2:** Schematic illustration of the BM assembly [24].

The interaction of the embedded cells with the ECM is also crucial in maintaining a healthy BBB. There are at least 50 types of proteins that interact with the different cells embedded in the BBB to provoke cell adhesion, migration, and signaling. The BM does not only exert a field for cell anchorage and migration, signaling transduction, but also structural support of the endothelium [11]. Interestingly, the synthesized ECM proteins indirectly upregulate the formation of TJs by enhancing the synthesis of molecules, such as cAMP, involved in the signal transduction for the

formation of TJs [25-28]. The BM networks further prevent the passage of large macromolecules from the blood capillaries and through the endothelium. The position of the BM between astrocytes and ECs creates an additional barrier [69]. Accordingly, there exists a bidirectional relation between the BBB cells and the BM, where the proteins secreted by the cells of the BBB further interact to induce and maintain the integrity of the BBB [6, 29].

Changes in the molecular and structural composition of the BM have been seen in several neurological disorders. For example, the thickening of the BM, along with the accumulation of amyloid- $\beta$  peptides and the formation of neurofibrillary tangles containing hyperphosphorylated tau filaments, are the hallmarks of AD. Disruption in the BM is also observed in patients suffering from a stroke. Although the mechanism is still unknown, studies suggest that the upregulation of proteases in the BM during a stroke degrades the ECM proteins, such as laminin, fibronectin, and collagen-IV [24, 70]. The role of the main ECM proteins in preserving the BM and the barrier property of the BBB is explained below.

i. Laminin

Laminin is a trimeric glycoprotein consisting of three cross chains  $\alpha$ ,  $\beta$ , and  $\gamma$  [71]. Until now, five  $\alpha$ , four  $\beta$ , and three  $\gamma$  chains are identified, bringing the total number of laminin isoforms to sixteen. All of these isoforms are abundant in both the CNS and peripheral nervous system (PNS). Specifically, the BBB's BM consists of laminin  $\alpha 1\beta 1\gamma 1$ ,  $\alpha 2\beta 1\gamma 1$ ,  $\alpha 4\beta 1\gamma 1$ , and  $\alpha 5\beta 1\gamma 1$  [71-73]. Each laminin isoform is synthesized predominantly, and sometimes exclusively, by a certain cell type. While astrocytes exclusively generate laminin 111 and laminin 211, BCECs synthesize laminin 411 and laminin 511.[74, 75] Pericytes, on the other hand, express all of these

laminins [75]. Interestingly, what characterizes the roles of laminin is the interaction of the  $\alpha$ -chain with the different cells [51, 72]. Laminin plays a major role in the early development and regulation of the BBB [76-79]. Studies suggest that laminin is enough for the early development of the BM [79]. Laminin's presence affects the electrical resistance of endothelium, thus affects the barrier's function [80]. Since laminin 111 and laminin 211 are exclusively expressed in the BBB's BM, astrocytic laminins (i.e. laminin 111 and laminin 211) are crucial for maintaining the BBB [75, 77, 81, 82]. The loss of astrocytic laminin, primarily due to mutations in  $\alpha 1$  and  $\alpha 2$  chains, reduces the expression of tight junction proteins and pericytes coverage, therefore causing the BBB's breakdown [83-86]. The role of endothelial and pericytic laminins remains controversial [77, 82].

Isoleucine-Lysine-Valine-Alanine-Valine (IKVAV) peptide is one the most active motifs in laminin 111 [87]. Its location on the  $\alpha 1$  chain clarifies how it determines the laminin function [88]. IKVAV has a crucial role in BM assembly, cell differentiation, migration, and growth [70, 89, 90]. With ECs, IKVAV promotes angiogenesis and revascularization [91, 92]. It further improves cell adhesion when combined with other adhesive peptides [87, 90, 93].

## ii. Fibronectin

Fibronectin, a di-sulfide dimer, is another multifunctional glycoprotein in the ECM [69]. It has critical roles in embryogenesis, wound healing, tissue repair, cell adhesion, migration, growth, and differentiation [94-96]. A unique feature of fibronectin is its ability to bind to different adhesive and signaling molecules in the ECM, such as collagen and HSPGs [95, 97]. Collagen binds to the collagen-binding domain in fibronectin to be deposited and maintained in the ECM [98, 99].

Arginine-Glycine-Aspartic Acid (RGD) is a major binding motif that promotes cell adhesion through integrin-mediated cell attachment signaling. The RGD recognition site was first identified in fibronectin but is commonly found in other ECM proteins [94, 100-102]. Although RGD is quite conserved, different integrins bind to different RGD containing proteins, triggering unique conformations. This is critical in specifying the role of RGD [103-105]. Besides their role in cell adhesion, fibronectin-derived RGD has been found to increase the electrical resistance across the endothelium and trigger the BCECs proliferation and spreading especially during embryogenesis [80, 106]. Studies have shown that any mutation in the fibronectin generally, and RGD specifically, can lead to impaired BM by massively reducing the cell adhesion [102, 106, 107]. Different amino acid conformations also affect the activity of the peptide by either activating or deactivating RGD [108]. Accordingly, the secretion of fibronectin is crucial for the cell attachment in the BM needed to maintain the BBB's integrity.

iii. Collagen-IV

Collagen, a family of at least 29 identified members, is the most abundant protein type in the body. Specifically, collagen-IV is vital for BM stability [79]. Collagen-IV is a trimeric protein, consisting of three  $\alpha$ -chains derived from six different  $\alpha$  conformations [109, 110]. The predominant isoform in the BBB's BM is that formed from two  $\alpha$ -1 chains and one  $\alpha$ -2 chain [68, 111]. Similar to the role of laminin and fibronectin, collagen-IV affects the barrier function in the BBB by increasing the electrical resistance of the BCECs [80]. Collagen-IV interacts with endothelial integrins enhances the expression of claudin-5 tight junction protein [112]. Interestingly, collagen-IV is crucial for maintaining the integrity, stability, and function of the BBB [79]. Mutations in the  $\alpha$ -1 and/or  $\alpha$ -2 chains of collagen-IV disrupt the BM structure as

its associated with the production of fragile vessels and leading to cerebrovascular diseases and embryonic lethality [113, 114].

iv. Nidogens

Nidogen, also known as enactin, is another protein component of the ECM that exists (nidogen-1 and nidogen-2). It links collagen-IV to laminin in the BM. The loss of nidogen leads to severe defects in the BM structure. Like loss of collagen-IV, the absence of nidogen affects the vascularization in the brain [115-118].

v. Heparan Sulfate Proteoglycans (HSPGs)

Similar to nidogens, HSPGs are found in the BM and commonly link to collagen-IV. Argin, a common type of HSPGs, is exclusively localized across the vascular endothelium that specifically has a barrier function. This suggests the role of argin in the barrier development in the BBB [119-121]. Specifically, argin is thought to be involved in the adhesion of astrocytes and BCECs to the BM [121, 122]. Perlecan is another common type of HSPGs commonly incorporated within the laminin-collagen-IV networks. Its location supports its role in maintaining the BM integrity and ability to interact with other molecules [123, 124]. Loss of perlecan causes vessel bleeding similar to strokes [125, 126]. Therefore, it is suggested that perlecan helps stabilize the BM [113, 127, 128].



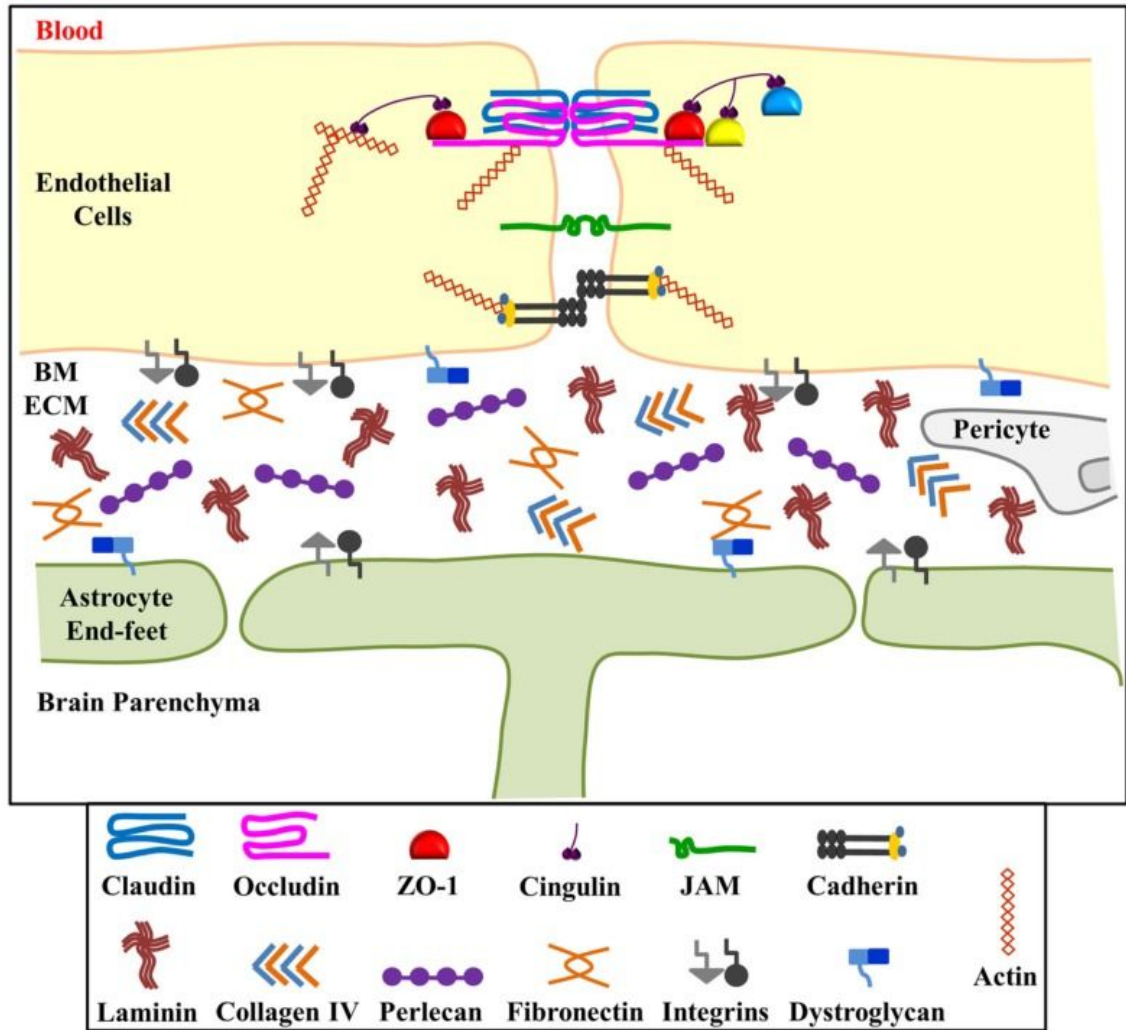


**Figure 3:** Schematic illustration of the BM [123].

## 2.2 Perturbations of the Blood-Brain Barrier

Failure of the BBB is critical in the initiation and progression of several CNS diseases. Although the BBB is a dynamic structure, any alteration in its homeostasis can ultimately develop a pathological condition. Hypoxia, for example, increases the permeability of the BBB by disrupting the TJ expression, specifically by downregulating the synthesis of occludin and upregulating the synthesis of nitric oxide and vascular endothelial growth factor (VEGF). Accordingly, the increased

expression of VEGF, a signaling protein that promotes the formation of new blood vessels in hypoxic tissues, is correlated with ischemic stroke [129-133].

Inflammation is another major insult that disrupts the homeostasis of the BBB. Inflammatory mediators adjust the BBB permeability by reducing the TJ proteins expression (e.g. occludin) and affecting the cell-matrix interactions [53, 134]. The increased expression of cytokines and enzymes, for example, upregulates the expression of matrix-metalloproteases (MMPs). MMPs, a family of zinc-endopeptidases, degrade ECM proteins. Specifically, MMP-2 and MMP-9 have a binding domain that enables them to bind to BM proteins, such as laminin, fibronectin, and collagen-IV to degrade them via proteolysis [135, 136]. This loss in BM proteins disrupts the assembly of TJs leading to the abnormally elevated permeability of the BBB. The limited activation of MMPs under physiological conditions is reflected by the enhanced BBB integrity [137-140].

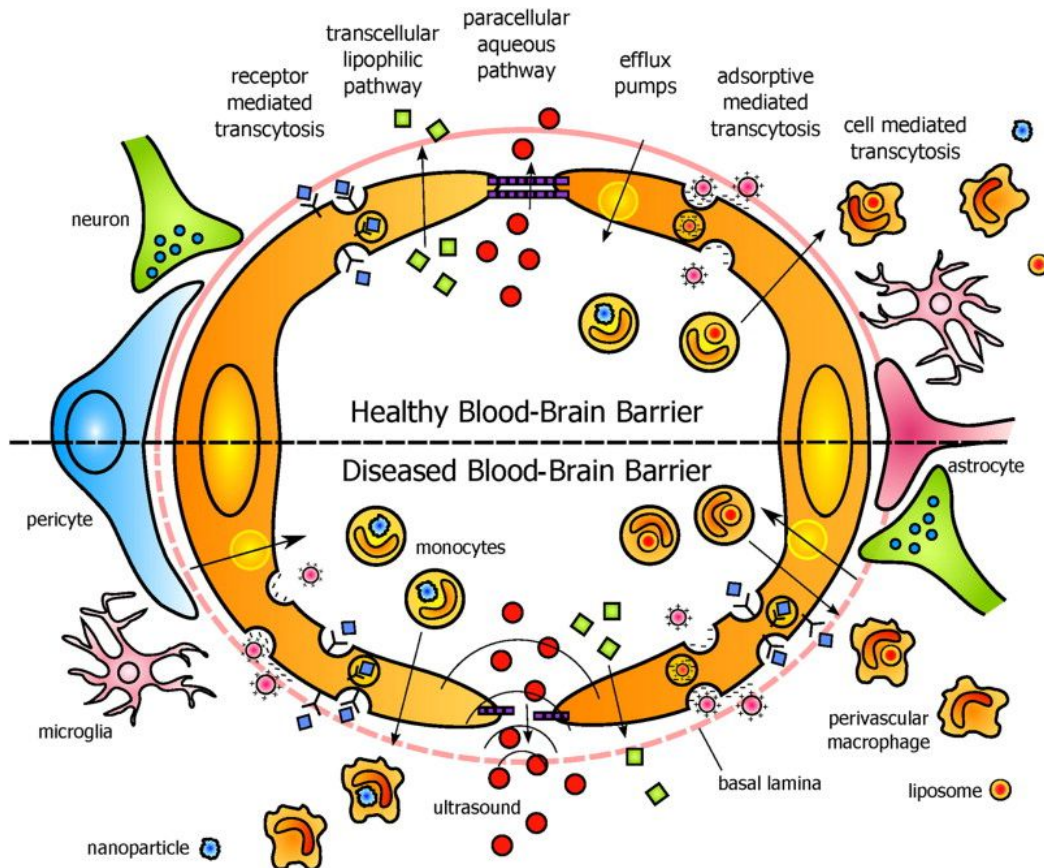


**Figure 4:** Schematic illustration comparing the permeability across a healthy BBB vs. a diseased BBB [121].

The consumption of certain drugs triggers the breakdown of the BBB. The intake of drugs, such as nicotine, cocaine, heroin, morphine, and alcohol promote BBB remodeling and activation of the immune system, affecting the neuroinflammatory pathways and signaling. These compounds increase the permeability of the BBB by decreasing the expression and distribution of ZO-1 [141, 142]. Alcohol, for example, elevates the expression of cytokines and other inflammatory mediators which proved to disrupt the BBB integrity [143]. All of these effects will eventually lead to neurotoxicity, a great disturbance of the CNS [144].

The challenges in treating these neurological diseases at an early stage involve facilitating the drug entry into the brain in addition to understanding the events during the onset of the disease. As previously mentioned, most neurological diseases are caused by the increased permeability of the BBB due to the interrupted expression of TJs. Although the final cascade events in most cases involve disrupting the TJs formation by proteases and free radicals, the specificity of the disease is determined by the dysfunction induced during the early stages of the molecular cascade. Accordingly, it is critical to define the molecular factors underlying a specific neurological disease to develop targeted drugs that are not only efficient in stopping the molecular abnormality and reversing the disrupted BBB integrity but also capable of crossing the highly selective BBB during physiology and pathophysiology [145].

### **3. Bio-mimicking the Blood-Brain Barrier**

Over the past 50 years, various models have been generated to bio-mimic the different and complex aspects of the BBB [30]. The ultimate goal for bio-mimicking the BBB is to understand the physiological and pathological states of the BBB. This enables researchers to develop and test targeted drugs that are capable of crossing the BBB in addition to develop efficient diagnostic techniques for these neurological diseases.

While *in vivo* testing is a good approach to study pharmacokinetics under a natural complexity, the difference in the BBB across different species restricts this approach. Additionally, *in vivo* models are considered expensive low throughput screening assays that trigger a major ethical concern. These limitations support the need for a biomimetics *in vitro* model that recapitulate the *in vivo* human BBB microenvironment [30, 31].

The first approach in developing *in vitro* BBB models started with the isolation of pure and intact rat brain capillaries, followed by culturing primary rat BCECs on porous inserts [32]. A major limitation of this approach is that primary cell line extraction requires animal sacrifice. Also, it is tricky to isolate a high yield of pure rat BCEC [11, 30, 31]. These restrictions, in addition to the almost negligible BBB phenotype in this monoculture model, triggered the need for co-culturing rat-derived BCECs with astrocytes. This astrocyte and BCEC co-culture enhanced the tightness and decreased the permeability of the model, reflected by the increased expression of tight junction proteins (e.g. ZO-1, claudin-5, and occludins). Interestingly, greater resistance was directly associated with culturing astrocytes on the bottom of the porous insert and the ECs on the top of the same porous inserts. This was attributed to the enhanced interaction between ECs and astrocytic endfeet. To further resemble the BBB NVU, triple culturing of ECs, astrocytes, and pericytes was later developed. Similar to co-culturing of astrocytes and BCEC, the tightness increased while the permeability decreased. This approach further induced the differentiation of the ECs. The best results were obtained when ECs were cultured on top of the porous inserts and the pericytes and astrocytes cultured on the bottom of the porous inserts. However, the planar dimensionality and absence of the ECM molecules that are crucial in maintaining the BBB *in vivo*, remain two major disadvantages for co-culturing and triple culturing on porous inserts [11, 30, 31].

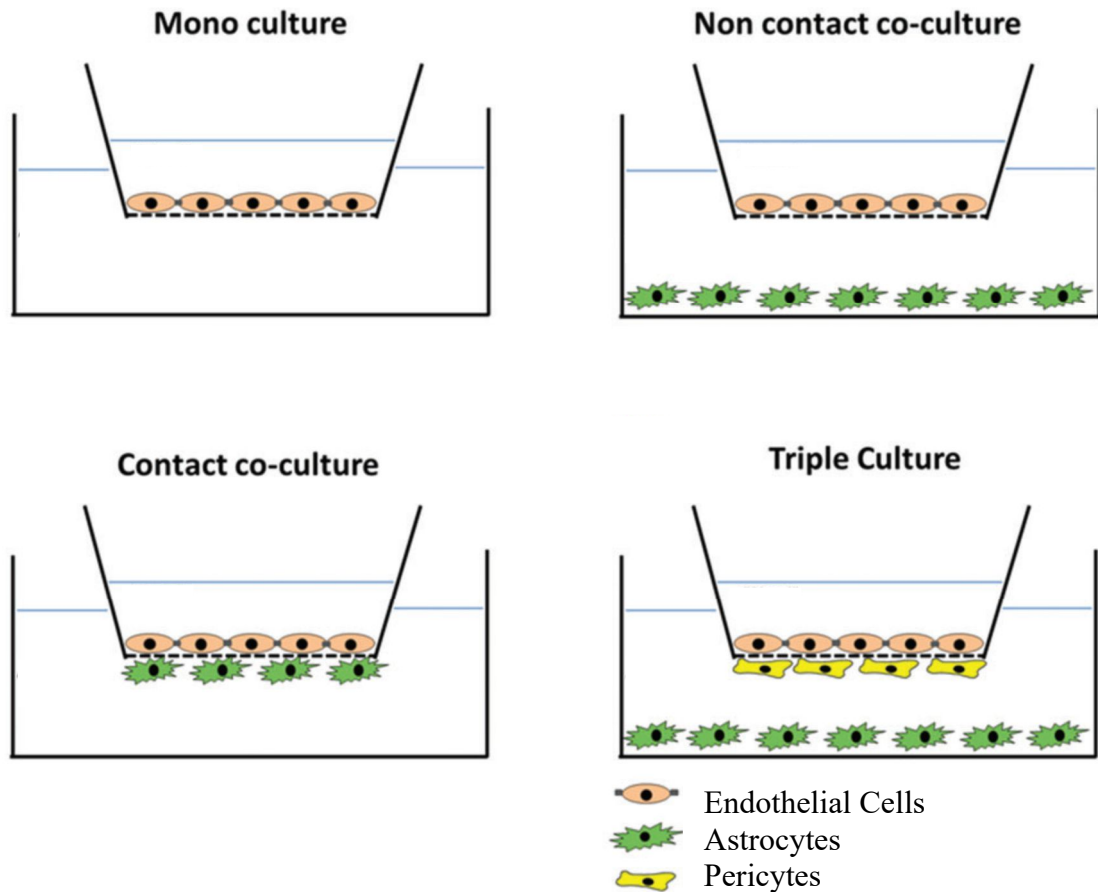


**Figure 5:** Schematic illustration of the developed static *in vitro* models to bio-mimic the BBB. **[A]** Monoculture of ECs on a porous membrane. **[B]** Non-contact co-culture of ECs on the inner side of the porous membrane and astrocytes on the bottom side of the well. **[C]** Contact co-culture of ECs on the inner side of the porous membrane and astrocytes on the bottom side of the porous insert. **[D]** Triple culture of ECs on the inner side of the porous insert, pericytes on the bottom side of the porous insert, and astrocytes on the bottom side of the well [30].

Another attempt to imitate the BBB *in vitro* was through developing a dynamic *in vitro* model that incorporates both shear stress and co-culturing of ECs and astrocytes. In summary, ECs were cultured in hollow fibers, and culture media was circulated to create tunable shear stress. Astrocytes were cultured on the other side of the porous material to allow direct contact between the astrocytes and ECs. Shear stress induced by the blood flow has been shown to enhance the barrier properties of the ECs

[146]. Similarly, co-culturing astrocytes with ECs further increases the tightness of the model. This was reflected by the significantly higher transendothelial resistance and significantly lower permeability of this *in vitro* model compared to the 2D co-culture model mentioned earlier. However, the dynamic *in vitro* model does not provide high throughput results, requires specific technical skills and high cell number to be loaded, and does not allow the visualization of the cell morphology. Another major limitation is that the thickness of the hollow fibers separating the ECs from the astrocytes is relatively thick compared to that of the BM *in vivo* [30, 31, 147, 148].

A microfluidic BBB model had been developed to address the disadvantages of the dynamic *in vitro* models. This approach generates shear stress by allowing the flow of culture media across two perpendicular channels. At the interface of these channels, ECs were co-cultured with astrocytes across a thin, porous membrane. The microfluidic system requires less cell numbers and allows the continuous measurement of the transendothelial resistance by the built-in electrodes. While several microfluidic models have been generated to enhance the resemblance to the *in vivo* microenvironment, there is still no well-established model that bio-mimics the complex aspects of the BBB BM [30, 31, 149, 150].

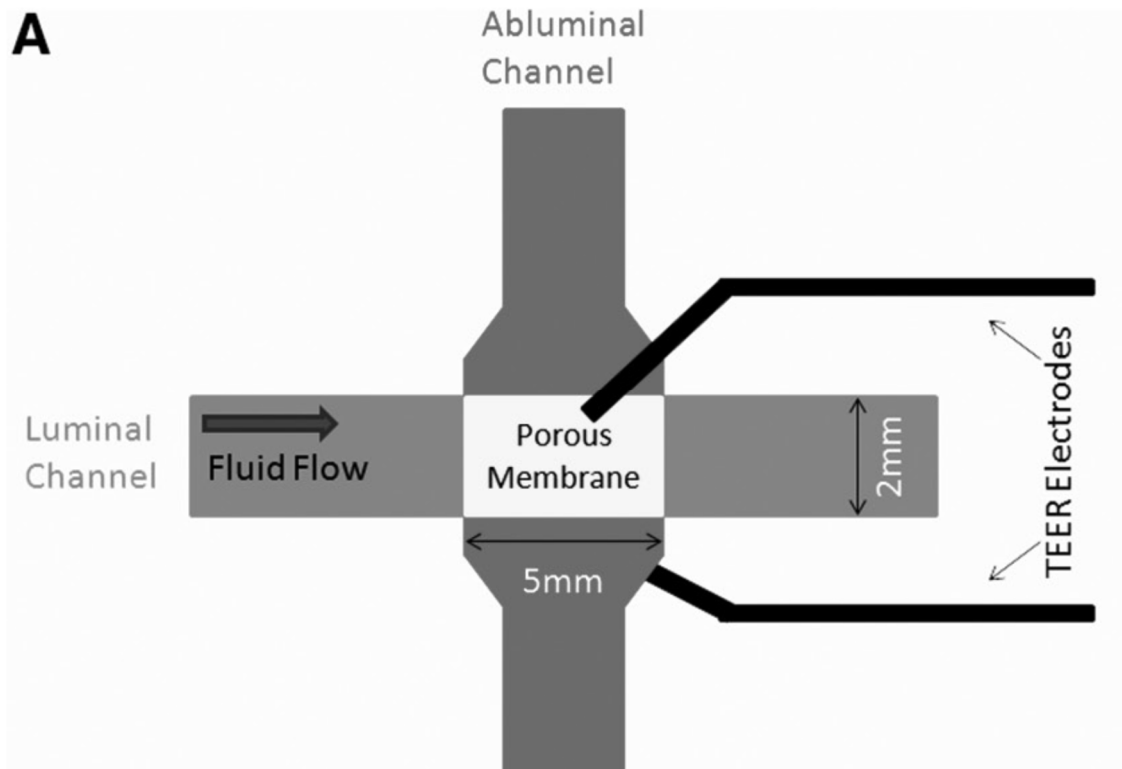


**Figure 6:** Schematic illustration of the microfluidic BBB model [33].

As mentioned earlier, the BM plays a major role in the maintenance of the BBB, where the downregulation of a single molecule may initiate certain neurological diseases. As such, it is crucial to include the major BM proteins, such as laminin, fibronectin, and collagen-IV in the developed models. To further bio-mimic the BBB, astrocytes must be allowed to grow and expand their processes in 3D, in which astrocytic endfeet interact with not only ECs but also ECM molecules to maintain the integrity of the BBB. Thus, hydrogel scaffold is a promising approach that can integrate various and complex aspects of the BBB [37].

#### 4. Hydrogels

Hydrogels, defined as hydrophilic 3D networks of crosslinked polymer chains, are often used in biomedical applications [34]. Their significant water content resembles



that of natural tissues, where water constitutes up to 60% of the human body [35]. Other advantages of hydrogels are their biodegradability, porosity, and tunable properties [36]. Consequently, the hydrogel scaffold could present a favorable milieu that arranges cells in 3D while inducing the tissue properties by enhancing cellular growth and communication. Interestingly, hydrogels are often referred to as ‘smart scaffolds’ where they can serve versatile functions and bio-mimic different tissues through adapting to the desired conditions [34, 151, 152].

Various natural and synthetic polymers are normally used to synthesize hydrogels. During the last two decades, naturally formed hydrogels were gradually replaced with synthetic ones, as the latter showed greater strength, water absorption capacity, and longer lifespan [153, 154]. Additionally, the well-defined structure of synthetic hydrogels is relatively more stable under severe conditions such as temperature and pH fluctuations. Similar to natural polymers, the properties of synthetic polymers can be adjusted to serve a certain function [35]. Yet, what significantly favors synthetic hydrogels over natural ones is their reproducibility and ability to control their physical and chemical properties (i.e. molecular weight, material, crosslinking, degradation, density). More specifically, understanding the hydrogel’s dynamics, degradation modes, and crosslinking approach is crucial as these properties determine the structural integrity of the fabricated hydrogel [37, 155]. Yet, the choice of polymer and the fabrication process (i.e. chemical crosslinking, thermal crosslinking, physical crosslinking, or photopolymerization) depends on the application of interest. In tissue engineering, the scaffolds should serve as a nontoxic environment for cellular growth and interactions. Also, the physical and chemical properties of the hydrogel should resemble that of the tissue or ECM of interest, should be degradable, and biocompatible

[156-159]. Having said that, polyethylene glycol (PEG) is a synthetic polymer extensively utilized in the field of tissue engineering as it serves as a promising scaffold for bio-mimicking specific tissues [37].

#### ***4.1 Polyethylene Glycol (PEG)***

As previously mentioned, PEG is an inexpensive FDA-approved synthetic polymer commonly used in biomedical applications, including drug delivery and tissue engineering [37]. PEG hydrogels are widely used in neural tissue engineering as they readily mimic the hydrated neural milieu without triggering an immune reaction. This can be attributed to the inert, biocompatible, and biodegradable properties of PEG, in addition to its high reproducibility and flexibility [38].

In brief, PEG is a hydrophilic inert material having the following general molecular formula:  $\text{H}(\text{OCH}_2\text{CH}_2)_n\text{OH}$  [38]. Depending on the application, PEG can be synthesized into a wide variety of structures, ranging from linear PEG, multi-arm PEG, and Y-shaped PEG [160]. Interestingly, both linear and Y-shaped PEGs are commonly utilized in PEGylation, the process in which PEG is covalently bonded to another molecule, such as drugs, peptides, or proteins [161, 162]. This approach is promising in pharmacokinetics and targeted therapy [163]. For tissue engineering multi-arm PEG crosslink into hydrogels to serve as suitable scaffolds to mimic a certain tissue [164]. Specifically, 4-arm PEG crosslinked hydrogels have been shown to induce relatively faster gelation, enhanced cell adhesion, and water uptake [165].

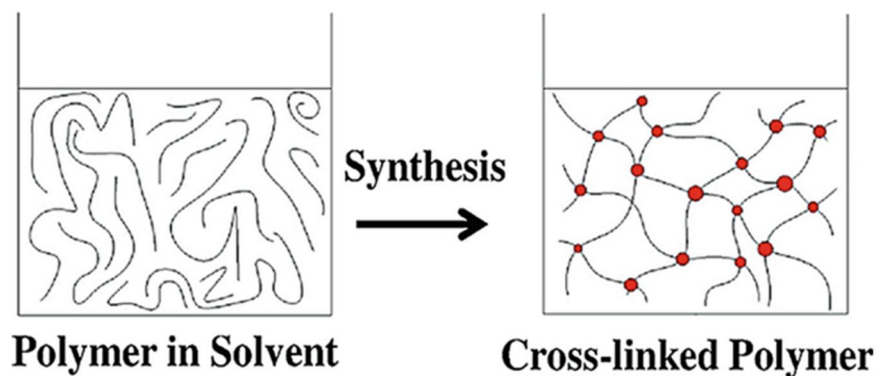


**Figure 7:** Schematic illustration of the polymerization process [166].

To increase the reactivity of the inert PEG to stimulate crosslinking, reactive functional groups, such as amine, carboxyl, and carbonyl are commonly added to the PEG terminal end [167]. PEG-vinyl sulfone (PEG-VS) is widely used to chemically crosslink hydrogels for biological applications via a Michael-type addition of thiol in the presence of cysteine-containing enzyme sensitive peptides (e.g. MMP-sensitive peptides) to form proteolytically degradable crosslinked networks [164, 168, 169]. Chemically crosslinking hydrogels for biological applications is vital since crosslinking via photo-polymerization requires UV rays and photo-initiators which may be toxic for the cells [170]. PEG-VS utilization in tissue engineering is also popular due to the relatively greater hydrolytic stability, lower immunogenicity, successful cell encapsulation during gelation, and ability to be modified with biological motifs, such as RGD, compared to other functionalized PEG hydrogels (i.e. PEG functionalized with acrylate, maleimide, or amine end groups) [39].

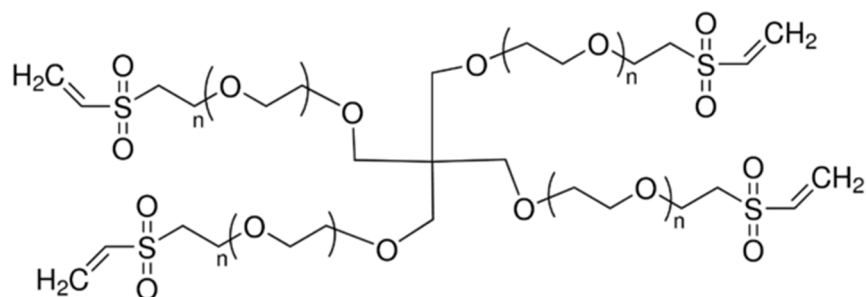


**Figure 8:** Four-arm polyethylene glycol-vinyl sulfone (PEG-VS) polymer [171].

Accordingly, PEG, particularly PEG-VS, can act as a promising approach for bio-mimicking the BBB *in vitro* as it can be functionalized with the major BM peptides. Additionally, the physiochemical and mechanical properties of the hydrogel can be tuned to resemble the *in vivo* BBB [164]. As mentioned earlier, PEG hydrogel is hydrolytically and enzymatically biodegradable, which provides a temporary 3D environment for the encapsulated and adhered cells to grow, interact, and secrete natural ECM molecules, without the accumulation of the degradation products. This advantage, as well as being biocompatible, decreases the immunogenicity of the model, allowing better biomimicry of the *in vivo* BBB [39, 172, 173].

## CHAPTER III

### RATIONAL AND HYPOTHESIS

Understanding the causes behind CNS diseases and the development of effective therapies remain limited due to the absence of an *in vitro* model that fully replicates the physiological properties of the BBB. A proposed approach is to reproduce the BBB by integrating a biocompatible hydrogel with the major components of the ECM, along with co-culturing ECs with astrocytes. This will enable the proper encapsulation and spreading of astrocytes in a 3D environment similar to *in vivo*, in the presence of the major BM peptides. The BBB *in vivo* endothelium will be mimicked by seeding the ECs on the hydrogels, allowing them to interact and form a monolayer. The different cell-cell and cell-matrix interactions are critical for maintaining the *in vivo* BBB. Thus, it is important to integrate the dimensionality, major cellular components, and major BM peptides in a milieu that resembles the *in vivo* microenvironment.

This project aimed to develop an *in vitro* model that closely resembles the main components of the BBB. A 3D co-culture BBB model was fabricated using PEG hydrogels functionalized with laminin and fibronectin-mimetic peptides. Specifically, PEG-VS polymer, modified with IKVAV and/or RGD peptides, was chemically crosslinked with MMP-sensitive peptides to enable polymerization and hydrogel formation. For this work, PEG functionalized with IKVAV, RGD, and IKVAV-RGD (1:1) was fabricated. Astrocytes were encapsulated within the fabricated PEG hydrogels and allowed to grow and protrude their endfeet. ECs were seeded on the hydrogel's surface to adhere and form a monolayer. The viability, spreading, and morphology of the astrocytes embedded in the functionalized PEG hydrogel were assessed.

Additionally, the activation of the ECs in this model was evaluated via measuring the expression of TJ proteins and assessing the transendothelial resistance and permeability. Accordingly, the role of astrocytes, laminin, and fibronectin in interacting with the ECs and regulating the tightness and permeability of the BBB was determined.

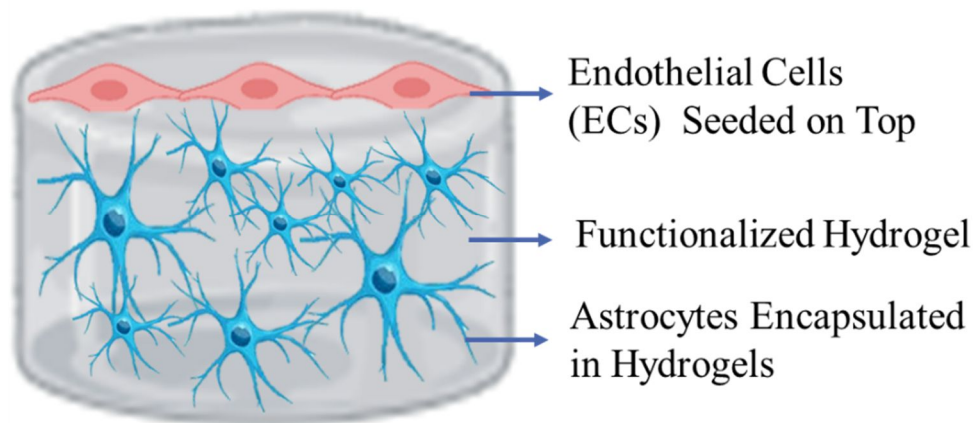


**Figure 9:** Schematic illustration of the fabricated model.

**Aim 1: Characterization and optimization of PEG hydrogels with IKVAV and MMP-sensitive peptides and their effect on viability, proliferation, and spreading of astrocytes by Live/Dead assay.**

**Hypothesis:** Viability is an important determinant of the success of the hydrogel. IKVAV is known to promote astrocytic processes' outgrowth, migration, and differentiation. Therefore, the viability of astrocytes embedded in the PEG hydrogel is expected to increase in the presence of IKVAV.

**Aim 2: To evaluate the role of ECs and astrocytes co-cultures, dimensionality, and the defined BM-mimetic peptides IKVAV and RGD on TJ formation by measuring the transendothelial electrical resistance (TEER), barrier functionality through a permeability assay of sodium fluorescein and albumin bound Evan's blue, and immunofluorescence staining of ZO-1. Assess astrocytes activation by GFAP immunohistochemistry.**

**Hypothesis:** The BBB model utilizing functionalized PEG hydrogels closely resembles the *in vivo* architecture of the BBB. Co-culturing ECs with astrocytes, in the presence of IKVAV and RGD, will enhance the formation of TJs, causing a higher expression of ZO-1, increase in TEER, and decrease in permeability. BM peptides will promote the activation of the astrocytes cultured in the functionalized 3D PEG hydrogel, leading to a higher expression of GFAP [24].

# CHAPTER IV

## MATERIALS AND METHODS

### 1. Materials

4-arm Poly(ethylene glycol)- vinyl sulfone (MW 20000) was obtained from JenKem Technologies, China. MMP-sensitive peptides (MW 2699.16), IKVAV peptides (MW 1007.22), and RGD Peptides (MW 346.34) were obtained from GL Biochem Shanghai, China. Phosphate Buffered Saline (PBS) Solution 10X was obtained from Lonza, Switzerland. Acetic Acid (100%) was obtained from AnalaR NORMAPUR, France. Fetal Bovine Serum (FBS), Trypsin Solution 10X, Tween-20, Penicillin-Streptomycin, Roswell Park Memorial Institute Medium (RPMI-1640 Medium), Dulbecco's Modified Eagle's Medium-High Glucose (DMEM-High Glucose), Bovine Serum Albumin (BSA A9418-50G), Ethidium Homodimer-I (2 mM in DMSO), Paraformaldehyde (100% PFA), Fluorescein Sodium Salt, and Evan's Blue were obtained from Sigma-Aldrich, USA. Astrocyte Basal Medium (ABM) was obtained from iXCells Biotechnologies, USA. Calcein-AM (1 mg/mL) was obtained from Molecular Probes, USA. Methanol (100%) was obtained from Honeywell Riedel-de Haen, Germany. Mouse Anti-GFAP Antibody (2 mg/mL) was obtained from Abcam, UK. Rabbit Anti-ZO-1 Antibody (0.25 mg/mL), Alexa Fluor 488 Goat Anti-rabbit IgG (2 mg/mL), Texas Red Goat Anti-mouse IgG (2 mg/mL), and DAPI (5 mg/mL) were obtained from ThermoFisher Scientific, USA. Triethanolamine (99%+; MW 149.19) was obtained from Arcos Organics, USA. Normal Goat Serum (S26-100 mL) was obtained from Chemicon International, USA. EVOM<sup>2</sup> and STX<sup>2</sup> Electrodes were obtained from World Precision Instruments (WPI), USA. 12-well plate inserts of pore-size 0.4  $\mu\text{m}$  and 8  $\mu\text{m}$  were obtained from FALCON, USA.



## 2. Methods

### 2.1 Fabrication of 4% PEG Hydrogels

#### a. Preparation of Solvents

The synthesized hydrogels are 4% PEG hydrogels functionalized with IKVAV and/or RGD peptides, then crosslinked with MMP-sensitive peptides. PEG, RGD, and MMP-sensitive peptides are soluble in TEOA buffer (pH=8, 0.3M), whereas IKVAV is soluble in acetic acid (0.01M). TEOA buffer (0.3M) was prepared by mixing DW (9.6 mL) with stock TEOA (397  $\mu$ L) and then setting the pH to 8. Acetic acid was prepared by adding stock acetic acid (143  $\mu$ L) to DDW (250 mL), bringing the final concentration to 0.01 M.

#### b. Preparation of Solutions

PEG was dissolved in TEOA buffer (pH=8, 0.3M), at a concentration of 4% of the final volume, by weight. So, for every 100  $\mu$ L total hydrogel volume, 4 mg of PEG were dissolved in TEOA. MMP-sensitive peptides constituted 10% of the total hydrogel volume, such that each 1mg of MMP-sensitive peptides was dissolved in 10  $\mu$ L TEOA buffer (pH=8, 0.3M). Peptides (RGD/IKVAV) were added according to a specific concentration. To prepare stock IKVAV solution (3 mM), IKVAV (1 mg) was dissolved in 10 mM acetic acid (331  $\mu$ L). . To prepare stock RGD solution (6 mM), RGD (1 mg) was dissolved in TEOA buffer (pH=8, 0.3M; 481.22  $\mu$ L). The solutes were dissolved in their respective solvents on the day of the hydrogel's fabrication.

### c. Formation of Hydrogels

PEG hydrogels were fabricated by a Michael-type addition of thiol-containing peptide onto a 4-armed PEG-VS, illustrated in fig. 10 [164]. In brief, adhesion peptides (RGD/IKVAV), at a certain concentration, were mixed with the dissolved PEG-VS and then vortexed for 30 seconds. After incubating this mixture for 15 mins at 37 °C, MMP-sensitive peptides (10%), acting as crosslinkers, were added to the functionalized PEG to bring the final molar ratio of VS:SH to 1:1 [173]. The crosslinked and functionalized PEG was vortexed for 5-10 seconds and pipetted into the corresponding membrane. The hydrogels were then incubated at 37 °C for 10 mins to polymerize and become viscous. To retain moisture, a sufficient amount of complete medium was added onto the hydrogels and then stored in the incubator at 37 °C and 5% CO<sub>2</sub>. The encapsulation of the astrocytes (NHA) and seeding of immortalized human aortic endothelial cells (ECV) will be explained later.

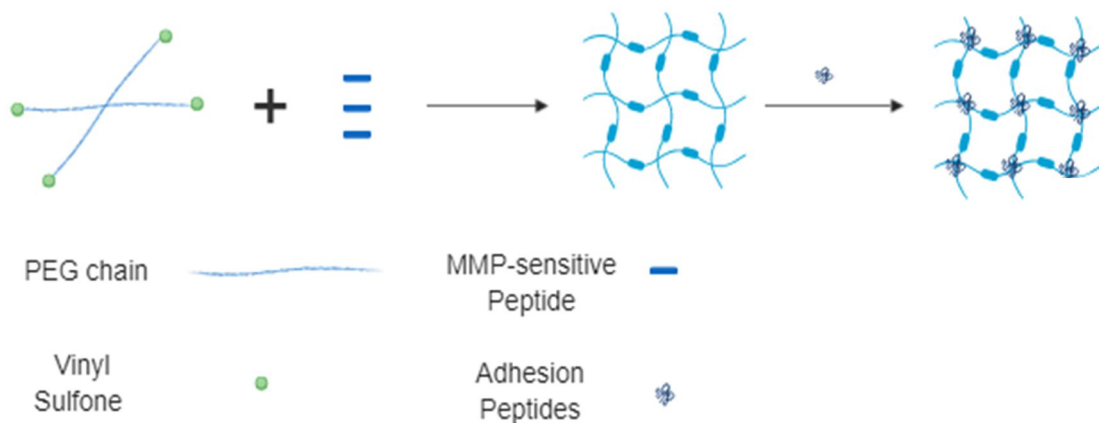


**Figure 10:** Crosslinking PEG-VS with MMP-sensitive peptides via a Michael-type addition reaction.

To investigate the effect of different IKVAV concentrations on the viability of the astrocytes in 4% PEG hydrogels, 75  $\mu\text{M}$ , 150  $\mu\text{M}$ , 300  $\mu\text{M}$ , and 600  $\mu\text{M}$  PEG-IKVAV hydrogels were fabricated according to the quantities mentioned in table 1 [174]. The values below are per 100  $\mu\text{L}$  of hydrogels ( $V_{\text{total}}=100 \mu\text{L}$ ).

<b>IKVAV Concentration</b>	<b>4% PEG</b>	<b>IKVAV (3mM stock solution)</b>	<b>MMP (10% final volume)</b>
75 $\mu\text{M}$	4 mg dissolved in 87.5 $\mu\text{L}$ TEOA	2.5 $\mu\text{L}$	1 mg dissolved in 10 $\mu\text{L}$ TEOA
150 $\mu\text{M}$	4 mg dissolved in 85 $\mu\text{L}$ TEOA	5 $\mu\text{L}$	1 mg dissolved in 10 $\mu\text{L}$ TEOA
300 $\mu\text{M}$	4 mg dissolved in 80 $\mu\text{L}$ TEOA	10 $\mu\text{L}$	1 mg dissolved in 10 $\mu\text{L}$ TEOA
600 $\mu\text{M}$	4 mg dissolved in 70 $\mu\text{L}$ TEOA	20 $\mu\text{L}$	1 mg dissolved in 10 $\mu\text{L}$ TEOA

**Table 1:** Preparation of 4% PEG-IKVAV hydrogels with different concentrations of IKVAV peptide ( $V_{\text{total}}=100 \mu\text{L}$ ).

Based on previous work, 600  $\mu\text{M}$  RGD is the optimal concentration for the viability and spreading of the astrocytes embedded within the 4% PEG hydrogels. PEG hydrogels functionalized with 600  $\mu\text{M}$  RGD (RGD-600  $\mu\text{M}$ ;  $V_{\text{total}}=100 \mu\text{L}$ ) were prepared by mixing RGD (10  $\mu\text{L}$  from 6 mM stock solution) with 4% PEG (4 mg dissolved in 80  $\mu\text{L}$  TEOA buffer). After vortexing the mixture for 30 seconds and incubating it for 15 mins at 37  $^{\circ}\text{C}$  and 5%  $\text{CO}_2$ , 10% MMP-sensitive peptides (1 mg dissolved in 10  $\mu\text{L}$  TEOA buffer) was added to PEG functionalized with RGD, allowing the PEG to crosslink and polymerize. After the PEG became viscous, a complete medium was added in an adequate amount to fully cover the fabricated hydrogel.

Likewise, to fabricate PEG hydrogels functionalized with 300  $\mu\text{M}$ :300  $\mu\text{M}$  IKVAV and RGD (IKVAV:RGD-300  $\mu\text{M}$ ), IKVAV (10  $\mu\text{L}$  of 3 mM stock solution)

and RGD (5  $\mu$ L of 6 mM stock solution) were added to 4% PEG (4mg dissolved in 75  $\mu$ L TEOA). After vortexing, the mixture for 30 seconds and incubating it for 15 mins at 37°C and 5% CO<sub>2</sub>, 10% MMP-sensitive peptides (1 mg dissolved in 10  $\mu$ L TEOA) was added to IKVAV:RGD-300  $\mu$ M, allowing it to crosslink and polymerize to form a hydrogel within 10 mins. As mentioned above, a complete medium was then added in an adequate amount to fully cover the hydrogel.

## ***2.2 Co-culturing of Endothelial Cells and Astrocytes***

### **a. Cell Culture**

Normal Human Astrocytes (NHA) cell line was used in all in vitro studies. The cells were cultured in a PLL-coated T-25 flask using ABM complete medium supplemented with 10% FBS and 1% antibiotics at 37°C and 5% CO<sub>2</sub>. To coat the T-25 flask, an adequate amount of PLL (1:20) was added to cover the surface of the flask. The PLL was then removed completely, and the flask was allowed to dry for at least 30 mins before washing. To remove residual PLL, the flask was washed with DW (3X; 5 mins between every wash) and allowed to dry for 30 mins before seeding NHA cells. After reaching approximately 90% confluency at around day 4, the cells were subcultured. In all experiments, cells were used between passages 4 and 7.

ECVs were also used in the in vitro studies. In vitro culture was carried out at 37°C and 5% CO<sub>2</sub> in a T-25 flask using RPMI complete medium supplemented with 10% FBS and 1% penicillin-streptomycin. After reaching approximately 90% confluency at around day 2, the cells were subcultured.

After reaching the desired confluency, cells were prepared for experiments by removing the Medium then washing them with PBS (1X) to remove any traces of the Medium. Trypsin solution (1X; 1mL) was added to the flask and swirled over the whole

surface. Then the flasks containing NHA and ECV cells were incubated for 30 seconds and 1 min, respectively, at 37 °C to enable the cells to fully detach. A minimum amount of about double the trypsin volume of the corresponding complete medium is added to deactivate the effect of trypsin. After that, the cells were collected in a separate 15 mL conical tube to be counted using a hemocytometer. A 50 µL sample was collected from the 15 mL conical tube and an equal volume of trypan blue, a diazo dye that is absorbed by viable cells with an intact membrane, was added [175]. Then, 10-15 µL of this cell suspension was added between the hemocytometer and cover glass, where cells were counted in all the outer squares of the hemocytometer. The total cell count was calculated by the following equation:

$$Total\ Cell\ Count = \frac{Total\ Count * Dilution\ Factor * Total\ Volume\ in\ 15\ mL\ Conical * 10,000}{Number\ of\ Counted\ Quadrants}$$

The needed volume of the desired cell count per condition was pipetted in 2 mL tubes via the following equation:

$$Volume\ to\ be\ taken = \frac{Needed\ Cell\ Count * Total\ Volume\ in\ 15\ mL\ Conical}{Total\ Cell\ Count}$$

The cells were then collected by centrifugation at 100 XG for 4 mins at 24 °C. Accordingly, NHAs were encapsulated within the PEG hydrogel at the desired cell density depending on the experiment. Similarly, ECVs were seeded on the hydrogels at the desired seeding density depending on the experiment.

## b. Encapsulation of Astrocytes

Before the addition of 10% MMP-sensitive peptides, NHA was resuspended within the PEG-Peptide mixture, and vortexed for 5 seconds. A cell density of 10,000 cells/10  $\mu$ L hydrogel was aimed for in each experiment.

The functionalized and crosslinked PEG hydrogel (20  $\mu$ L) with encapsulated NHAs was pipetted and spread thoroughly on the coverslip. Under this condition, the cell density was 20,000 NHA per coverslip. After pipetting the hydrogels, all coverslips were placed in a 24-well plate and incubated at 37  $^{\circ}$ C for 10 mins to speed the gelation process. When the hydrogels become viscous, ABM complete medium (500  $\mu$ L) was loaded into the well to fully cover the fabricated hydrogels. The 24-well plate was then placed in the incubator at 37  $^{\circ}$ C and 5% CO<sub>2</sub> to be used in further experiments. (Fig. 11)

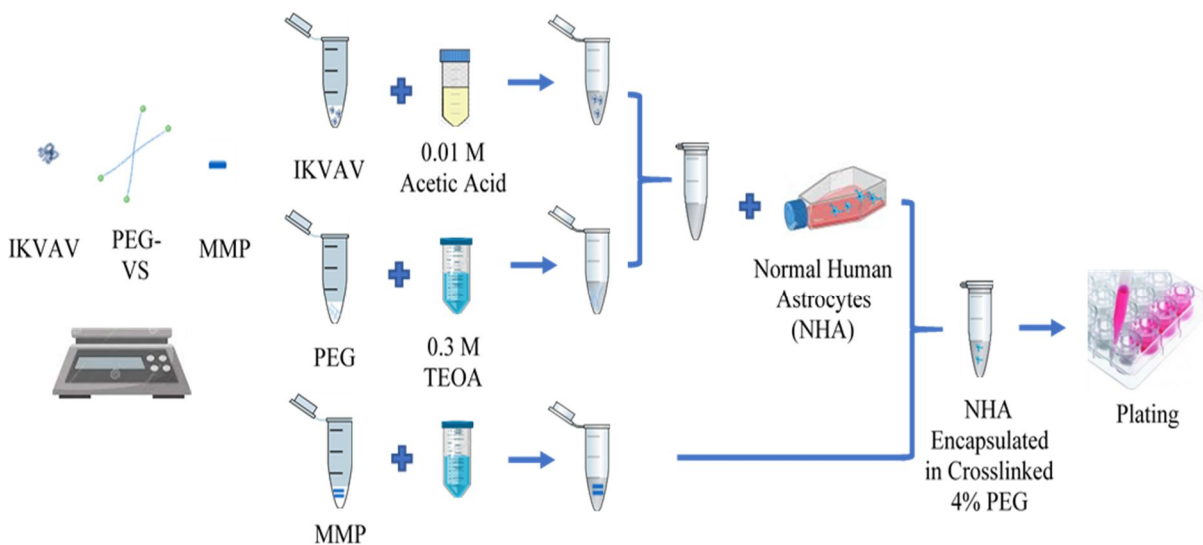


**Figure 11:** Schematic illustration of the PEG hydrogel fabrication process and astrocytes encapsulation.

To co-culture ECVs and NHAs, PEG hydrogels (40  $\mu\text{L}/\text{sample}$ ) were pipetted on 12-well inserts (8  $\mu\text{m}$  pore-size) with a cell density of 40,000 NHA per insert. 10% MMP-sensitive peptide was added to the functionalized PEG hydrogel with encapsulated NHAs. The total mixture was vortexed for 5 seconds and then pipetted to cover the inner surface of the insert. The 12-well plate containing the inserts was then incubated at 37 °C for 10 mins to speed up the gelation process. Once the hydrogels became viscous, ABM complete medium was added to the inserts (300  $\mu\text{L}$ ) and wells (1000  $\mu\text{L}$ ). The 12-well plate was then incubated at 37 °C and 5% CO<sub>2</sub> to be used in further experiments.

For the co-culture control, astrocytes were seeded on the bottom side of the 12-well insert (0.4  $\mu\text{m}$  pore-size). After centrifugation, NHAs were resuspended in ABM complete medium (300  $\mu\text{L}$ ) and seeded on the PLL-coated bottom side of an insert at a density of 10,000 cells per insert. The insert was then placed in the incubator for 3 hours to allow the cells to adhere. After that, the insert was flipped in a 12-well containing ABM complete medium (900  $\mu\text{L}$ ). The 12-well plate containing the insert was incubated at 37 °C and 5% CO<sub>2</sub> to be used in future experiments.

For RGD, previous work has shown that 600  $\mu\text{M}$  is the optimal concentration for the growth and spreading of the astrocytes inside the fabricated PEG hydrogels. For IKVAV, the optimal concentration for the growth and spreading of the astrocytes inside the fabricated PEG hydrogels was determined by the LIVE/DEAD assay explained below. These concentrations were used in the fabrication of hydrogels for co-culture experiments.

c. Seeding of Endothelial Cells

To obtain a monolayer, ECVs were seeded on the fabricated PEG hydrogel scaffolds at a seeding density of around 500,000 cells per insert. The PEG hydrogels were fabricated under these conditions: PEG hydrogels functionalized with RGD and/or IKVAV, and with or without encapsulated NHA. Before seeding, ABM complete medium found on the PEG hydrogels with encapsulated NHA (300  $\mu\text{L}$ /insert; 1000  $\mu\text{L}$ /well) was replaced with RPMI complete medium. RPMI complete medium was added to the inserts (300  $\mu\text{L}$ /insert) and wells (1000  $\mu\text{L}$ /well) of the PEG hydrogels without NHA.

NHA was given four days to grow and extend. On day 4 post-fabrication, ECVs were seeded into the samples. Following subculturing, counting, and centrifugation of ECVs, the desired seeding density was resuspended in RPMI complete medium (200  $\mu\text{L}$ /sample) and evenly seeded on the functionalized PEG hydrogel, bringing the total volume per insert to 500  $\mu\text{L}$ . The 12-well plate containing the inserts was then incubated at 37 °C and 5% CO<sub>2</sub> to enable the ECVs to form a 2D monolayer. (Fig. 12)



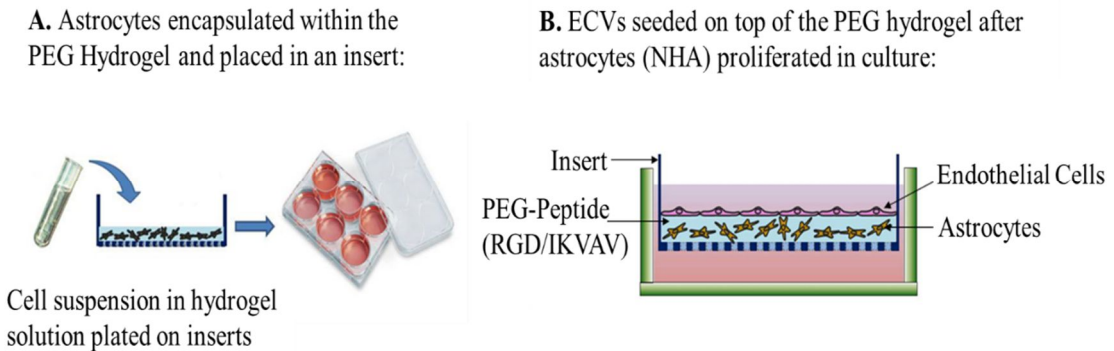


**Figure 12:** Schematic illustration of **[A]** Astrocyte's encapsulation inside the PEG hydrogel **[B]** ECVs seeding on the PEG hydrogels with embedded NHA.

As controls, ECVs were both monocultured and co-cultured with NHAs on 12-well inserts (0.4  $\mu\text{m}$  pore-size) at a seeding density of 25,000 cells per insert. ECVs and NHAs are cultured on the opposite sides of the porous insert since studies have shown that indirect contact culture results in better interaction between the two cell types.[176] As previously mentioned, NHAs were seeded on the bottom side of the porous insert and incubated for four days at 37 °C and 5% CO<sub>2</sub>. Before seeding, the ABM complete medium was replaced with RPMI complete medium (300  $\mu\text{L}$ /insert; 1000  $\mu\text{L}$ /well). To seed the ECVs on the inner membrane of the insert, 25000 cells were resuspended in RPMI complete medium (200  $\mu\text{L}$ /insert) and evenly seeded on the porous membrane, bringing the total volume in the inner compartment of the insert to 500  $\mu\text{L}$ .

RPMI complete medium in the inner compartment of the inserts was changed every 24 hours and every 48 hours for the wells. The 12-well plate containing the fabricated PEG hydrogels and the controls were incubated at 37 °C and 5% CO<sub>2</sub> to be later used in the experiments.

### 2.3 LIVE/DEAD Assay

To determine the optimal IKVAV concentration needed for the growth and spreading of the astrocytes encapsulated within the fabricated PEG hydrogels, a LIVE/DEAD assay was performed. As previously mentioned, PEG hydrogels were functionalized with IKVAV at four different concentrations: 75  $\mu\text{M}$ , 150  $\mu\text{M}$ , 300  $\mu\text{M}$ , and 600  $\mu\text{M}$ . NHAs were encapsulated in the functionalized 3D PEG hydrogels as described above.

For this experiment, PEG hydrogels functionalized with different concentrations of IKVAV (75, 150, 300, and 600  $\mu\text{M}$ ) and containing encapsulated NHAs (20  $\mu\text{L}$ ) were pipetted on coverslips at a cell density of 20,000 cells per sample, in triplicates. The 24-well plate containing the coverslips was incubated at 37°C and 5% CO<sub>2</sub>. The viability of the astrocytes was assessed at days 1, 4, and 7 post-fabrication by co-staining for live and dead cells.

### Staining

At each time-point (days 1, 4, and 7), one sample out of the triplicate fabricated hydrogels for each concentration (75, 150, 300, and 600  $\mu\text{M}$ ) was transferred into a new 24-well plate. To initiate the assay, the medium was removed, and the samples were washed (3X; 5 mins between every wash), with PBS (1X) to remove residual RPMI. Calcein-AM (2  $\mu\text{M}$ ) and EthD-1 (1  $\mu\text{M}$ ) dyes were used to stain the live and dead cells, respectively. Calcein-AM fluoresces green when cleaved by the intracellular esterases of living cells via an acetoxymethyl ester hydrolysis. EthD-1 fluoresces red when bound to the DNA of dead cells whose plasma membrane is disrupted [177]. For proper staining, an adequate amount of the diluted dyes was added to fully cover the hydrogels.

DMEM incomplete medium (400  $\mu$ L) containing Calcein-AM (2  $\mu$ M) and EthD-1 (1  $\mu$ M) was added to the fabricated PEG hydrogel and incubated for 30 mins at 37°C and 5% CO<sub>2</sub>. After 30 mins, the dye was removed, and samples were washed twice with PBS (1X) to remove any traces of the dye. Samples were then fixed with 4% PFA (400  $\mu$ L) and stored in the dark at room temperature. After 25 mins, the 4% PFA was removed, and samples were washed three times with PBS (1X). To retain the hydrogel's hydration during storage, PBS (1X; 700  $\mu$ L/sample) was added. Fluorescent images were taken using a Zeiss LSM710 confocal microscope and analyzed using ImageJ. (Fig. 13)

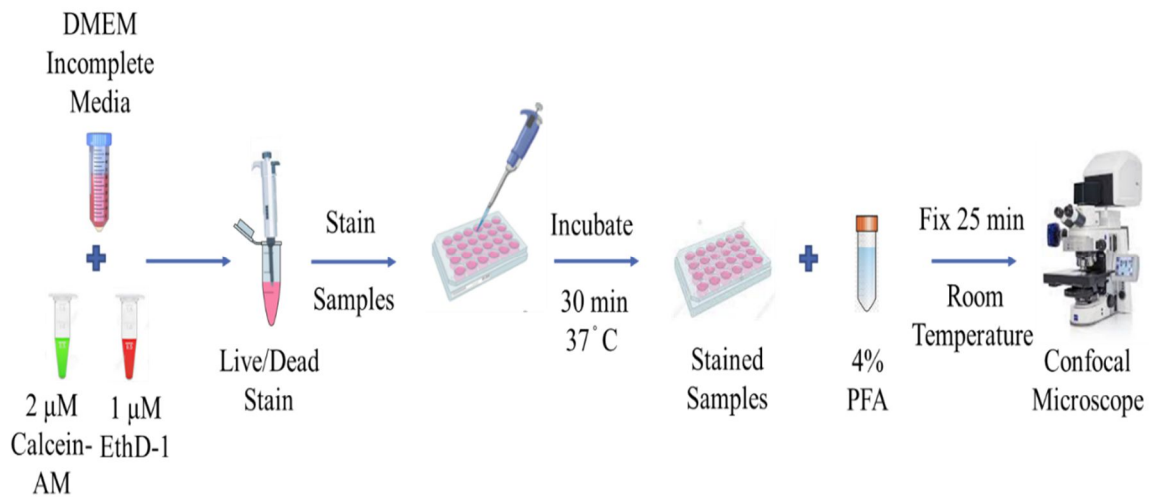


**Figure 13:** Illustration of the Live/Dead staining of NHAs embedded in the functionalized PEG hydrogels at different IKVAV concentrations (75, 150, 300, and 600 mM) at days 1,4, and 7 post hydrogel fabrication.

### Percentage Viability

The % viability of the astrocytes embedded inside the stained PEG hydrogels, under the different IKVAV concentrations (75, 150, 300, and 600  $\mu\text{M}$ ) at days 1, 4, and 7, was determined by the following formula:

$$\% \text{ Viability} = \frac{\text{Number of Live Cells}}{\text{Total Number of Cells}} * 100$$

### ***2.4 Transendothelial Electrical Resistance (TEER) Measurement***

To evaluate the tightness of the ECV monolayer, TEER, a reflective measure of the flux of ions across the monolayer, was measured using STX2 electrodes and EVOM2 [30]. For this study, the fabricated PEG hydrogels were: PEG functionalized with RGD and/or IKVAV, and with or without encapsulated NHA. Functionalized PEG hydrogels with RGD and/or IKVAV were fabricated to determine the effect of the astrocytes on the tightness of the BBB, reflected by TEER.

PEG hydrogels (40 $\mu\text{L}$  /sample) were pipetted into 12-well inserts (8  $\mu\text{m}$  pore-size) as per the protocol mentioned above. ECVs were then seeded on the scaffolds at day 4 post-fabrication, as described above. The two controls, ECVs monocultured and co-cultured with NHAs on 12-well inserts (0.4  $\mu\text{m}$  pore-size) following the protocol mentioned above. RPMI medium was added to the 8  $\mu\text{m}$  and 0.4  $\mu\text{m}$  pore-size blank inserts (300  $\mu\text{L}$ ) and corresponding wells (1000  $\mu\text{L}$ ) to prevent any discrepancies in the recordings. TEER was measured at days 1 to 5 post-seeding. (Fig. 14)

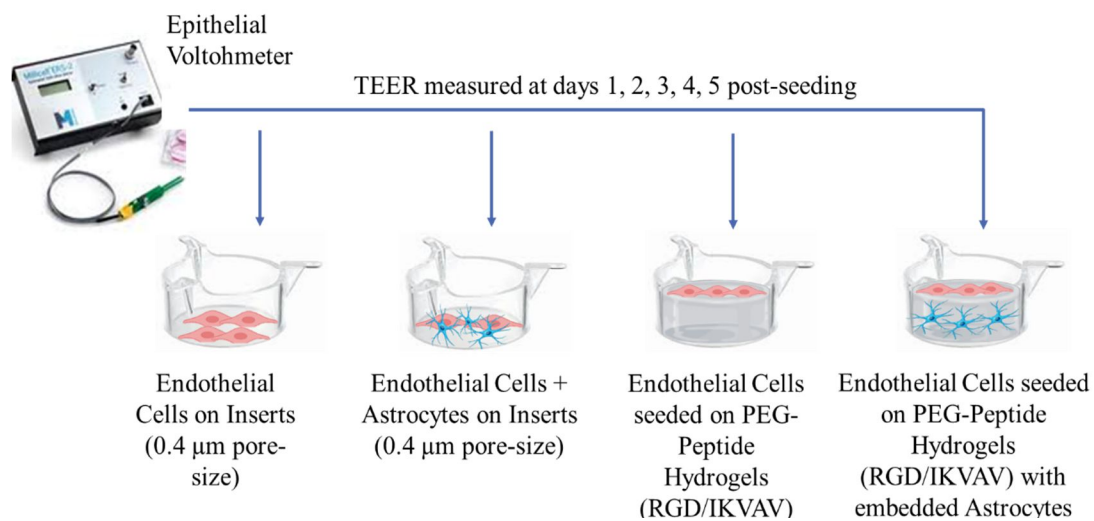


**Figure 14:** Schematic illustration of the TEER measurement system.

The STX2 electrodes were initially washed with 6 mL PBS (1X) for at least 5 mins. In the meantime, EVOM2 was calibrated to obtain consistent values when measuring. The electrodes were then connected to EVOM2 and placed in a 15 mL conical containing 4 mL PBS (1X). To further ensure that the measurements obtained were consistent, the TEER reading of the 4 mL PBS in this conical was recorded and was expected to be between 8-12  $\Omega$ . The electrodes were then clamped and positioned correctly, not angled and slightly touching the bottom of the well, with the shorter probe placed inside the inner compartment of the insert, and the longer probe placed outside the insert. (Fig. 15)

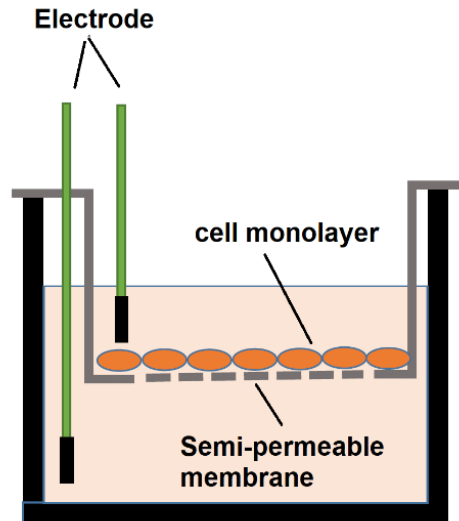


**Figure 15:** Schematic illustration of electrodes positioning during TEER measurement [178].

The TEER readings of the samples were recorded in a consistent order, starting with the blank (8  $\mu\text{m}$  pore-size), fabricated PEG hydrogels (8  $\mu\text{m}$  pore-size), the other blank (0.4  $\mu\text{m}$  pore-size), ECVs and NHAs co-culture (0.4  $\mu\text{m}$  pore-size), and ending with the ECVs monoculture (0.4  $\mu\text{m}$  pore-size). Between each measurement, the electrodes were placed for 30 seconds in the 15 mL conical containing 4 mL PBS to prevent any discrepancies in the readings. The 4 mL PBS in the 15 mL conical was changed after recording the TEER values for all the samples, whereas the 6 mL PBS (for washing) was changed every other day. The RPMI complete medium loaded into the inner (500  $\mu\text{L}$ ) and the outer compartments (1000  $\mu\text{L}$ ) of the insert were changed after recording the TEER values for all the samples.

To find the true resistance across the monolayer in a specific sample, the TEER reading of the blank was first subtracted from the TEER reading of the sample, and then multiplied by the insert's surface area (surface area of the 12-well insert=0.9  $\text{cm}^2$ ) according to the following equation:

*TEER* ( $\Omega \cdot \text{cm}^2$ )

= (*Reading Across the Sample*

– *Reading Across the Relative Blank*) \* 0.9

### **2.5 Permeability Assay**

The permeability of the ECV monolayer was further assessed using two commonly used inert permeability tracers, EBA and Na-F. Evan's blue dye (MW 961) was bound to bovine serum albumin (2% BSA; MW 69,000) to become a high molecular weight protein marker, known as EBA. Whereas Na-F (MW 376), a freely diffusible low molecular weight tracer, was left unbound.[13, 179, 180] The flux of EBA and Na-F across the ECV monolayer was determined at day 5 post-seeding. A permeability assay buffer consisting of PBS (1X), 10 mM HEPES, 25 mM Glucose, 1.2 mM MgCl<sub>2</sub>, and 1.3 mM CaCl<sub>2</sub> was used to prepare the permeability dye (EBA/Na-F).

To initiate the assay, RPMI medium was removed from all inserts and respective wells, and the samples were then washed (2X; 5 mins between every wash) with PBS (1X). Permeability assay buffer (400  $\mu\text{L}$ ) containing Na-F (10 mg/mL stock) and 2% BSA mixed with Evan's blue dye (17 mg/mL stock) was added to the inner compartment of the inserts. The inserts were then transferred into new 12-wells containing permeability assay buffer (1000  $\mu\text{L}$ /well). Samples (220  $\mu\text{L}$ ) were collected from the lower compartments (wells) at 30, 60, 90, and 120 mins, and directly replaced with fresh permeability assay buffer (220  $\mu\text{L}$ ). (Fig. 16)

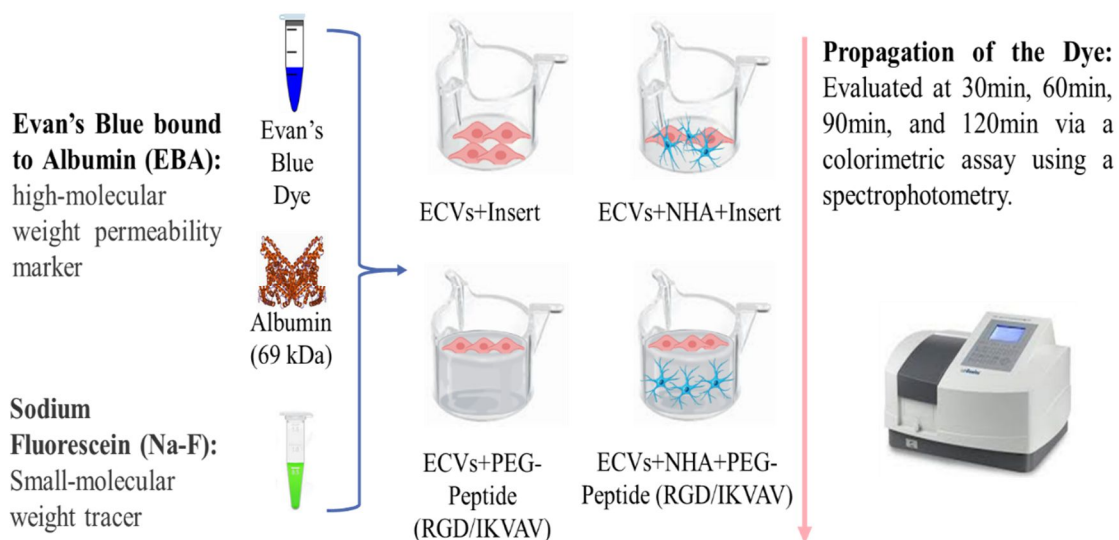


**Figure 16:** Schematic illustration of the permeability assay.

The concentrations of EBA that crossed the fabricated *in vitro* BBB hydrogel model were determined by reading the absorbance of the collected aliquots with a MULTISKAN EX Spectrophotometer using a 630 nm optical filter. The sample content of EBA was quantified based on a linear standard curve plotted from known concentrations of the dye. Aliquots (200  $\mu$ L/sample) from collected samples were pipetted into a 96-well plate, along with the aliquots of the standardized curve, and the well plate was put in the multi-plate reader.

After reading the plate, the corrected concentrations ( $\mu$ g/mL) of EBA were found by:

1. Subtracting the obtained blank absorbance (1X PBS) from the sample's absorbance at 30, 60, 90, and 120 mins.
2. The concentration C ( $\mu$ g/mL) of a sample at a certain time-point was then calculated by the following equation:

$$C_{time\ t} (\mu\text{g/mL}) = \frac{(\text{Absorbance}_{time\ t} - \text{Blank}) + 0.0013}{0.0223}$$



3. The corrected concentration  $CC$  ( $\mu\text{g/mL}$ ) at a certain time-point was then calculated by the following equation:

$$CC_{30 \text{ minutes}} = C_{30 \text{ minutes}}$$

$$CC_{60 \text{ minutes}} (\mu\text{g/mL}) = C_{60 \text{ minutes}} + (C_{30 \text{ minutes}} * 0.22)$$

$$CC_{90 \text{ minutes}} (\mu\text{g/mL}) = C_{90 \text{ minutes}} + (C_{60 \text{ minutes}} * 0.22)$$

$$CC_{120 \text{ minutes}} (\mu\text{g/mL}) = C_{120 \text{ minutes}} + (C_{90 \text{ minutes}} * 0.22)$$

The concentrations of Na-F that crossed the fabricated in vitro BBB hydrogel model were analyzed by measuring the fluorescence intensity of Na-F via a Tristar<sup>2</sup> S LB 942 Filter-Based Multimode Plate Reader using a fluorescent excitation and emission filter pair [Ex(k)  $485 \pm 10$  nm; Em(k)  $530 \pm 12.5$  nm]. The sample content of Na-F was quantified based on a linear standard curve plotted from known concentrations of the dye. Aliquots (5  $\mu\text{L}$ /sample) from the collected samples were pipetted into a black 96-well plate containing PBS (1X; 95  $\mu\text{L}$ /well), bringing the total volume per well to 100  $\mu\text{L}$ . Aliquots of the standardized curve were also prepared and pipetted into the same 96-well plate.

After reading the plate, the final concentrations (ng/mL) of Na-F were calculated by:

1. Subtracting the obtained blank fluorescence (1X PBS) from the sample's absorbance at 30, 60, 90, and 120 mins.
2. The concentration  $C$  (ng/mL) of a sample at a certain time-point was then calculated by the following equation:

$$C_{time \ t} (\text{ng/mL}) = \frac{(\text{Fluorescence}_{time \ t} - \text{Blank}) + 28634}{74227}$$

3. The corrected concentration  $CC$  (ng/mL) at a certain time-point was then calculated by the following equation:

$$CC_{30 \text{ minutes}} = C_{30 \text{ minutes}}$$

$$CC_{60 \text{ minutes}} \text{ (ng/mL)} = C_{60 \text{ minutes}} + (C_{30 \text{ minutes}} * 0.22)$$

$$CC_{90 \text{ minutes}} \text{ (ng/mL)} = C_{90 \text{ minutes}} + (C_{60 \text{ minutes}} * 0.22)$$

$$CC_{120 \text{ minutes}} \text{ (ng/mL)} = C_{120 \text{ minutes}} + (C_{90 \text{ minutes}} * 0.22)$$

4. The final concentration  $FC$  (ng/mL) at a certain time-point was then calculated by the following equation:

$$FC_{30 \text{ minutes}} \text{ (ng/mL)} = CC_{30 \text{ minutes}} * 20$$

$$FC_{60 \text{ minutes}} \text{ (ng/mL)} = CC_{60 \text{ minutes}} * 20$$

$$FC_{90 \text{ minutes}} \text{ (ng/mL)} = CC_{90 \text{ minutes}} * 20$$

$$FC_{120 \text{ minutes}} \text{ (ng/mL)} = CC_{120 \text{ minutes}} * 20$$

## ***2.6 Immunofluorescence Staining for ZO-1 and GFAP***

Zonula occludin-1 (ZO-1), a peripheral membrane phosphoprotein, belongs to the family of TJ proteins [13]. The higher the formation of TJs, the higher the expression of ZO-1. To analyze the formation of TJs between ECVs seeded on the fabricated PEG hydrogels, immunohistochemical staining of ZO-1 was performed as per the protocol described below.

Glial fibrillary acidic protein, known as GFAP, is a type III intermediate filament protein expressed by the astrocytes of CNS [181]. To analyze the spreading of the NHAs embedded in the fabricated PEG hydrogels, immunohistochemical staining of GFAP was performed as per the protocol described below.

For this experiment, the fabricated PEG hydrogels were as follows: PEG functionalized with RGD and/or IKVAV, and with or without encapsulated NHA. Functionalized PEG hydrogels with RGD and/or IKVAV were fabricated to determine the effect of the astrocytes on the expression of ZO-1, hence the formation of TJs. The same protocol previously explained was used to fabricate these hydrogels, encapsulate NHAs, seed ECVs, and culture the two controls. Upon the formation of an ECVs monolayer at day 5 post-seeding, immunohistochemical staining was initiated. Briefly, indirect immunohistochemical staining consists of 5 main steps: fixation and permeabilization, blocking, incubating with primary antibody, fluoresces labeling with secondary antibody, and finally DAPI staining. (Fig. 17)

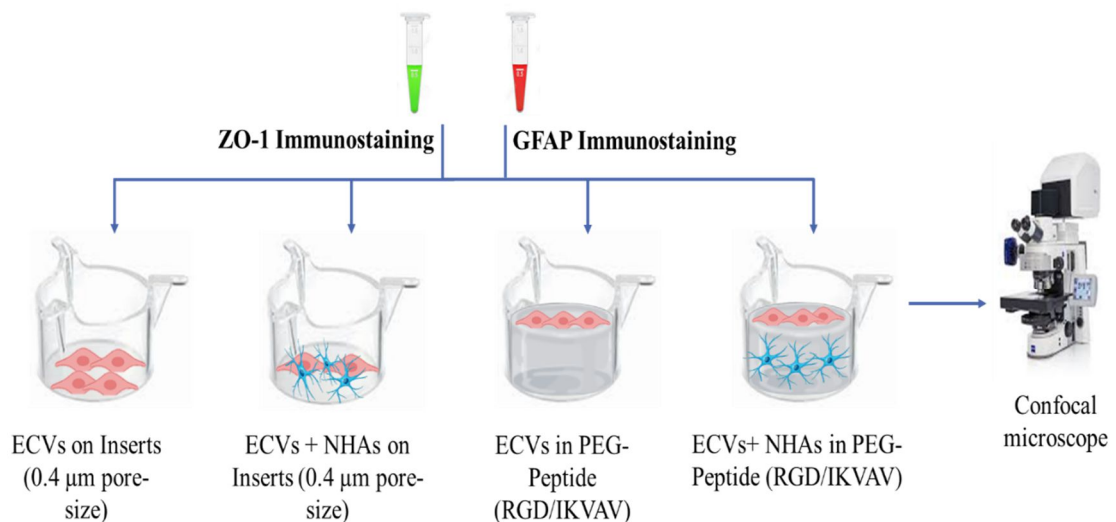


**Figure 17:** Schematic illustration of the ZO-1 and GFAP indirect immunofluorescence staining.

To initiate this experiment, RPMI medium was removed from all inserts and respective wells, and the samples were then washed (2X; 5 mins between every wash) with PBS (1X). To fix the samples, 4% PFA (800 μL/well and 200 μL/insert) was added for 20 mins at room temperature. Then, permeabilize the cells, 100% Methanol

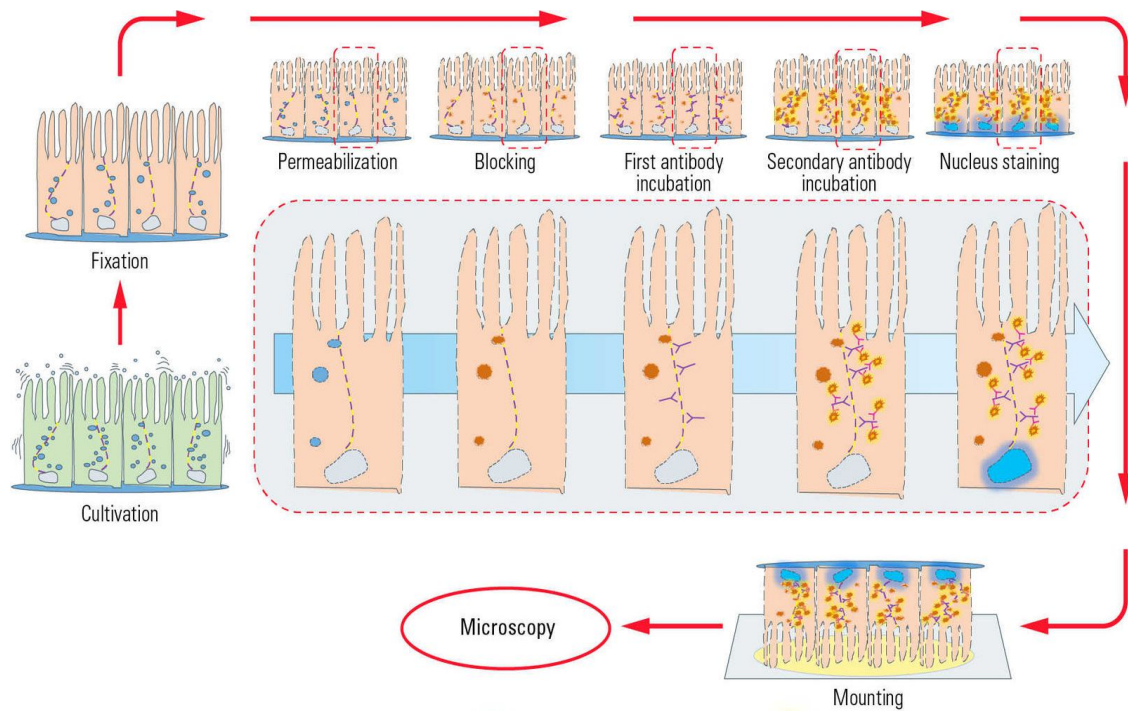
(800  $\mu$ L/well and 200  $\mu$ L/insert) was added for 1 hour at -20 °C. The samples were then washed (2X) with PBS and the blocking solution consisting of 3% bovine serum albumin (BSA) and 3% normal goat serum (NGS) was prepared. This blocking solution (100 $\mu$ L) was added for 1 hour at room temperature to the inner chamber of all inserts except the ECV-NHA control. For this control, 3% NGS-BSA was added to both the inner and outer compartments of the insert.

In the meantime, the primary antibodies were prepared by separately mixing 1% blocking solution (1% BSA-NGS) with rabbit anti-ZO-1 antibody (0.25 mg/mL stock; dilution 1:250) and with mouse anti-GFAP antibody (2 mg/mL stock; dilution 1:500). Different primary antibodies can be concurrently added to the samples. To stain for ZO-1, the inserts were incubated overnight at 4 °C with diluted rabbit anti-ZO-1 antibody (100  $\mu$ L/sample), added to the inner compartment of all the inserts. To stain for GFAP, the inserts were incubated for 48 hours at 4 °C with diluted mouse anti-GFAP antibody (100  $\mu$ L/sample), added to the inner compartment of the following inserts: PEG-Peptide (IKVAV/RGD) with embedded NHA; and to the outer compartment of the following insert: ECV-NHA co-culture control.

After 24 hours, samples with no encapsulated NHA were washed (2X; 5 mins in between washes) with PBS-Tween and incubated in the dark for 1 hour at room temperature with Alexa Flour 488 goat anti-rabbit IgG (2 mg/mL stock; dilution 1:1000; 100  $\mu$ L/sample) to fluorescently label ZO-1. To prepare this secondary antibody, a 1% blocking solution was mixed with Alexa Flour 488 goat anti-rabbit IgG and added to the inner compartment of the inserts. The samples were then washed (3X) with PBS-Tween, and DAPI (5 mg/mL stock; dilution 1:5000; 100  $\mu$ L/sample) was added for 10

mins at room temperature. After two more washes with PBS, the inserts were shaped to fit in the confocal dishes and mounted with antifade reagent (20 $\mu$ L /sample).

A similar protocol was followed to stain the samples containing NHA cells, with the secondary antibody. However, secondary antibodies were added successively. After 48 hours, the samples were washed (2X; 5 mins in between washes) with PBS-Tween and incubated in the dark for 1 hour at room temperature with Alexa Fluor 488 goat anti-rabbit IgG (2 mg/mL stock; dilution 1:1000; 100  $\mu$ L/sample) to fluorescently label ZO-1. The samples were then washed (3X) with PBS (1X), and Texas Red goat anti-mouse IgG (2 mg/mL stock; dilution 1:500; 100  $\mu$ L/sample) was added to the inner compartment of the PEG-Peptide (IKVAV/RGD) with embedded NHA samples and to the outer compartment of the ECV-NHA co-culture control to fluorescently label GFAP. After incubating the samples for 1 hour at room temperature, the Texas Red goat anti-mouse IgG was removed, and samples were washed (3X; 5 mins in between) with PBS-Tween. DAPI (5 mg/mL stock; dilution 1:5000; 100  $\mu$ L/sample) was then added as per the protocol mentioned before. The samples were then similarly washed, shaped, and mounted with an antifade reagent. Fluorescent images of all the samples were taken using a Zeiss LSM710 confocal microscope.



### 3. Statistical Analysis

**Figure 18:** Schematic illustration of the undirect immunofluorescence workflow [1].

All statistical tests were performed using GraphPad Prism software. When comparing more than two independent groups, One-Way ANOVA Tukey (HSD) Post-hoc test was used for parametric data. Two-Way ANOVA Tukey (HSD) Post-hoc test was used when independent groups were studied against two variables. A p-value less than or equal to 0.05 was considered significant according to the following:

Symbol	Meaning
ns	P-value > 0.05
*	P-value ≤ 0.05
**	P-value ≤ 0.01
***	P-value ≤ 0.001

**Table 2:** Statistical analysis convention followed by GraphPad Prism 9.

# CHAPTER V

## RESULTS AND DISCUSSION

### 1. Optimization of the PEG Hydrogels Functionalized with IKVAV

For this experiment, PEG hydrogels were functionalized with an increasing concentration of laminin-mimetic peptide IKVAV (75, 150, 300, and 600  $\mu\text{M}$ ). The goal was to study the effect of incorporating IKVAV in 4% PEG hydrogels on the viability of the encapsulated astrocytes. PEG is an inert polymer; thus the results reflected the role of IKVAV on the survival and proliferation of astrocytes. Cell viability of the astrocytes in the PEG hydrogels was determined by a Live/Dead assay. Live cells were stained with Calcein-AM, while dead cells were stained with EthD-1. A confocal laser scanning microscope was used to assess the cell fluorescence. The viability of the astrocytes inside the PEG-hydrogels functionalized with increasing IKVAV concentration was compared at days 1, 4, and 7.

Images showed that astrocytes were viable in all PEG hydrogels independent of the IKVAV concentration (75, 150, 300, and 600  $\mu\text{M}$ ). As seen in fig. 19, comparable live cell distribution was observed in all the samples per day. Jongpaiboonkit et al. previously proved that unfunctionalized PEG hydrogel induces cell death over an extended timeframe [182]. This shows that IKVAV is crucial in maintaining the survival of 3D encapsulated astrocytes by creating a nontoxic milieu that enhances cell viability. This is relevant to a previous study, where Gronthos et al. found that the incorporation of several ECM proteins, such as IKVAV and RGD, induce the proliferation of 2D bone marrow stromal cells culture [183]. Our finding was further supported by calculating the percentage viability (%) of the encapsulated astrocytes.

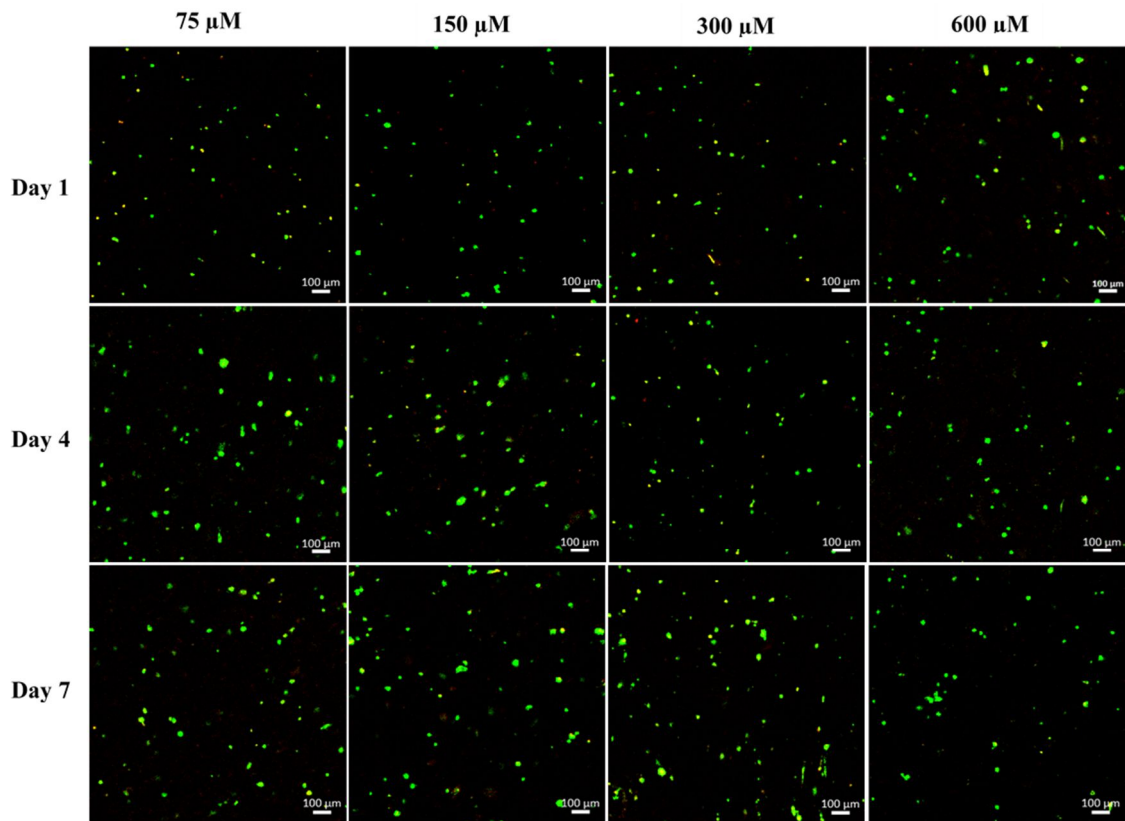


**Figure 19:** Live/dead assay of NHA embedded in 4% PEG with different IKVAV concentrations (75  $\mu\text{M}$ , 150  $\mu\text{M}$ , 300  $\mu\text{M}$ , and 600  $\mu\text{M}$ ) at days 1, 4, and 7. Live NHA were stained with Calcein-AM (Green). Dead NHA were stained with EthD-1 (Red). Images were taken using a confocal microscope with a 10X objective. Scale bar=100  $\mu\text{m}$ , (n=3).

Quantification of live cells and dead cells in the fabricated PEG hydrogels showed a viability percentage (%) of  $78.3 \pm 3.4\%$  in IKVAV-75  $\mu\text{M}$ ,  $71.4 \pm 4.0\%$  in IKVAV-150  $\mu\text{M}$ ,  $77.4 \pm 2.5\%$  in IKVAV-300  $\mu\text{M}$ , and  $76.5 \pm 3.0\%$  in IKVAV-600  $\mu\text{M}$  at day 1. This ratio of live astrocytes slightly increased at day 4 under all conditions, reaching a viability percentage (%) of  $81.2 \pm 3.5\%$  in IKVAV-75  $\mu\text{M}$ ,  $79.8 \pm 1.7\%$  in IKVAV-150  $\mu\text{M}$ ,  $80.8.4 \pm 2.8\%$  in IKVAV-300  $\mu\text{M}$ , and  $79.2 \pm 1.8\%$  in IKVAV-600  $\mu\text{M}$ . A similar pattern was further obtained at day 7, where the viability percentage (%) of astrocytes in the IKVAV-75  $\mu\text{M}$  reached  $82.0 \pm 2.5\%$ ,  $81.2.4 \pm 1.6\%$  in IKVAV-150  $\mu\text{M}$ ,  $86.6 \pm 2.8\%$  in IKVAV-300  $\mu\text{M}$ , and  $80.3 \pm 2.6\%$  in IKVAV-600  $\mu\text{M}$ . However, no



statistically significant difference in the percentage of viable astrocytes between the different IKVAV concentrations at days 1, 4, and 7 was observed. As seen in fig. 20, regardless of the IKVAV concentration, the viability of the astrocytes was high (>80%). This shows that incorporating laminin-mimetic peptide IKVAV alone supports the NHA viability for extended timeframes. This is consistent with a previous study done by Jongpaiboonkit et al. where they showed that the viability of encapsulated human mesenchymal stem cells (hMSC) increased, over 7 days, when IKVAV was combined within a PEG network [182]. This can be attributed to the role  $\alpha$ 1 chain of laminin-1 in inducing cell survival via the binding of IKVAV peptide to receptors in the astrocyte's membrane, triggering cell-matrix interactions needed to suppress apoptosis [70].

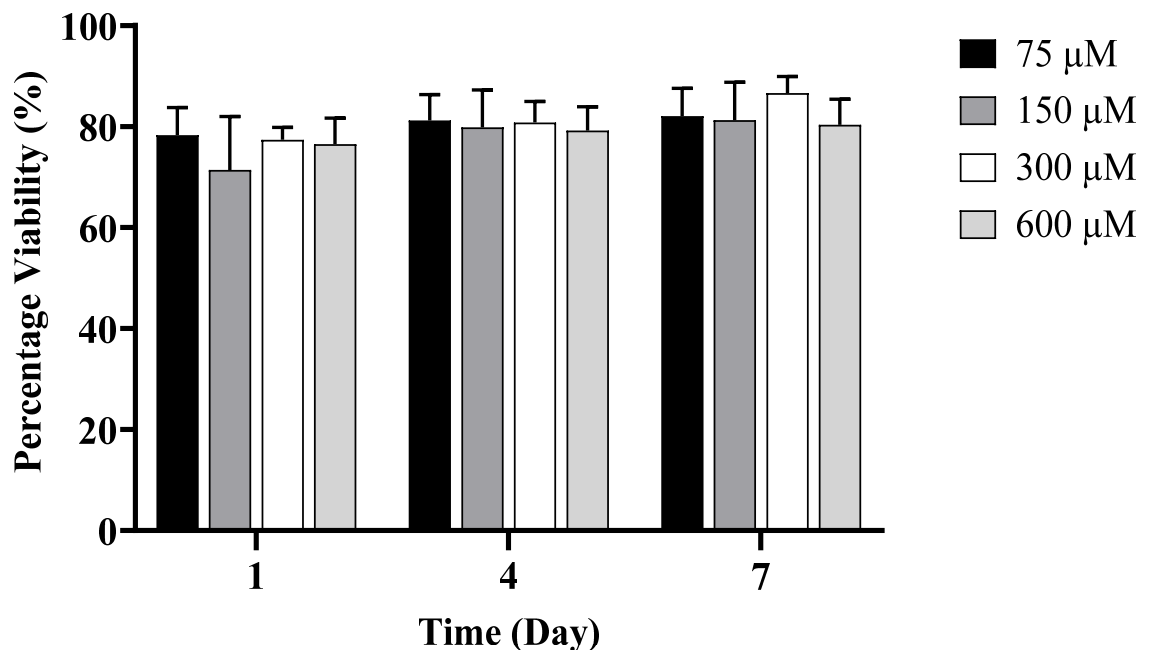


**Figure 20:** Percentage Viability (%) of NHA embedded in 4% PEG hydrogels functionalized with different IKVAV concentrations (75, 150, 300, and 600  $\mu$ M) at days 1, 4, and 7. No statistical significance found ( $p$ -value > 0.05). Error bars represent  $\pm$  SEM, ( $n=3$ ).

To confirm the ability of NHAs to proliferate in the fabricated hydrogels, the number of live cells for each concentration was determined and statistically analyzed using a two-way ANOVA. As illustrated in fig. 21, there was no significant difference in the number of live cells between the increasing IKVAV concentrations at the extended timeframe. However, NHA embedded in IKVAV-300  $\mu\text{M}$  showed an increasing number of live cells between days 1 and 7. This concentration further recorded the highest number of live cells among all samples on day 7.

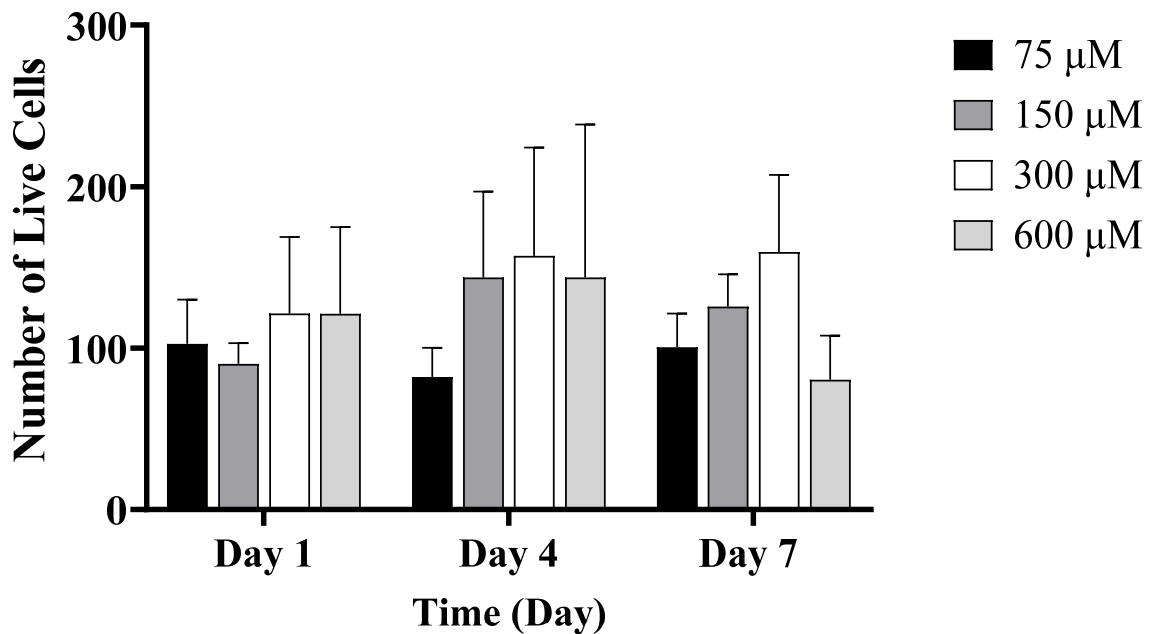


**Figure 21:** Number of Live NHA embedded in 4% PEG hydrogels functionalized with different IKVAV concentrations (75, 150, 300, and 600  $\mu\text{M}$ ) at days 1, 4, and 7. No statistical significance was found ( $p\text{-value} > 0.05$ ). Error bars represent  $\pm$  SEM, ( $n=3$ ).

Despite the increase in the viability between days 1 and 7, some astrocytes displayed a round morphology. This was observed qualitatively using the 3D images (Z-Stacks) obtained using a confocal laser scanning microscope (fig. 22). Such outcome is consistent with a previous finding where hMSC also displayed a round morphology

when encapsulated in a 3D PEG hydrogel [182]. This might be attributed to the mesh size and porosity of the PEG network. Hassan et al. propose that a highly cross-linked hydrogel network would block integrin receptors and attachment sites on cells [184]. This would restrict cell growth, interactions, and secretions. However, the porosity and mesh size of the fabricated 4% PEG hydrogels were not evaluated nor quantified in the current work. Still, it can be suggested that IKVAV significantly promotes cell survival, without interfering much in its spreading.

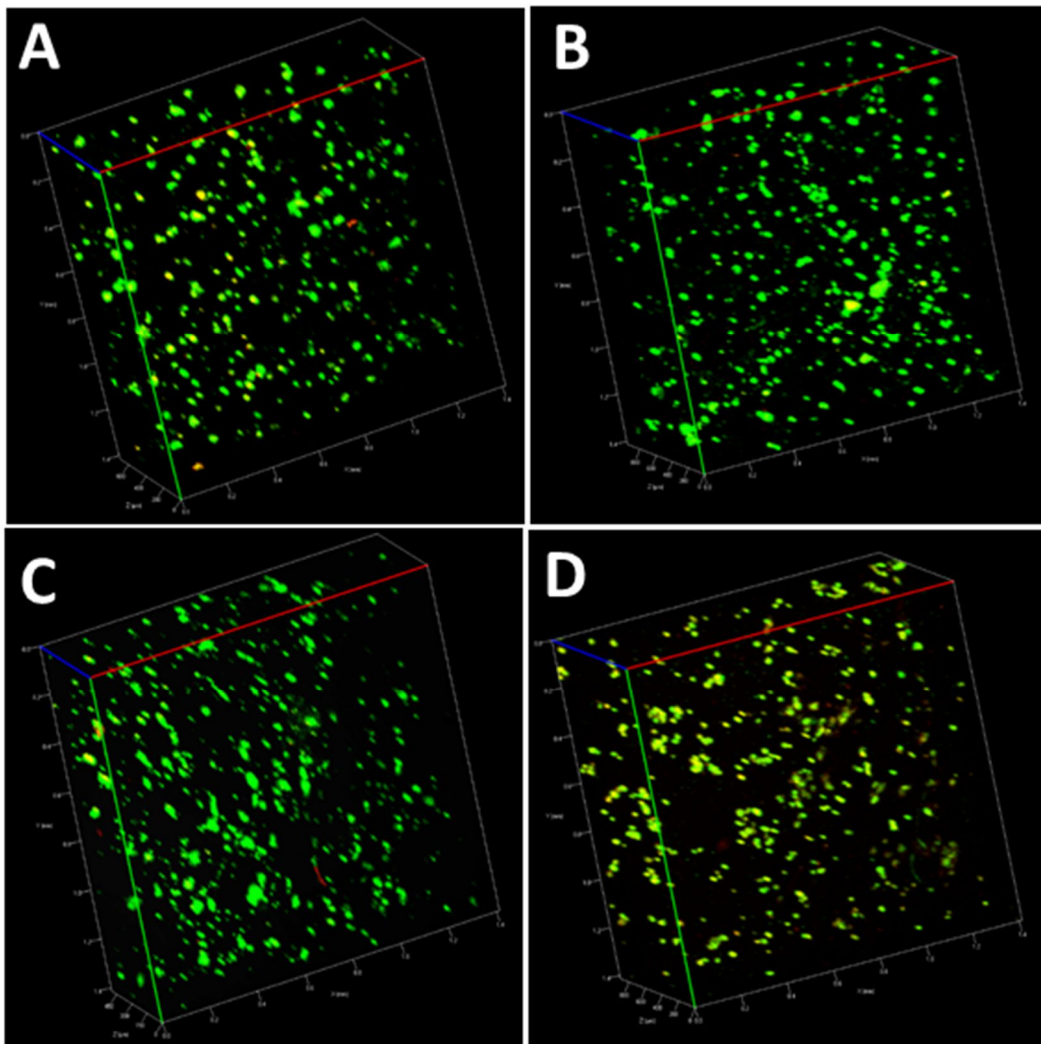


**Figure 22:** A 3D 4% PEG hydrogel functionalized with [A] 75  $\mu\text{M}$  [B] 150  $\mu\text{M}$  [C] 300  $\mu\text{M}$  [D] 600  $\mu\text{M}$  laminin-mimetic peptide IKVAV. Astrocytes were embedded inside the hydrogel. Live NHAs were stained with Calcein-AM (Green). Dead NHA were stained with EthD-1 (Red). Z-stack images were taken using a confocal microscope with a 10X objective. Scale bar=100  $\mu\text{m}$ , (n=3).

While there was no significant difference recorded in the astrocytic viability and proliferation between PEG hydrogels functionalized with increasing IKVAV concentrations (75, 150, 300, and 600  $\mu\text{M}$ ), IKVAV-300  $\mu\text{M}$  was chosen to be used in co-culturing. First, this concentration induced a slightly greater, yet insignificant, NHA viability. It further maintained an increasing number of live cells over an extended

timeframe. Additionally, 3D images (10X) taken by the confocal microscope showed a relatively enhanced astrocytic growth and extension. Thus, it can be thought that this concentration promotes signaling without oversaturating the cell membrane. Lam et al. previously showed that 300  $\mu\text{M}$  IKVAV concentration is optimal for cellular differentiation in 3D [174]. This is consistent with the current finding where 4% PEG hydrogel functionalized with 300  $\mu\text{M}$  of laminin-mimetic peptide IKVAV proved to provide an optimal milieu for astrocytic survival and proliferation.

## 2. Seeding of Endothelial Cells

The BBB barrier integrity is primarily induced by the formation of the endothelium. To mimic the *in vivo* setting, ECVs were seeded on top of the fabricated 4% PEG hydrogels. To assess the sole and cumulative effects of laminin-mimetic peptide IKVAV and fibronectin-mimetic peptide RGD on the activity of the ECs, PEG hydrogels were functionalized with the following concentrations: IKVAV-300  $\mu\text{M}$ , RGD-600  $\mu\text{M}$ , and IKVAV:RGD-300  $\mu\text{M}$ .

After seeding, the adherence of the ECVs and the establishment of the endothelial monolayer were evaluated using an inverted light microscope. As seen in fig. 23A, ECVs did not adhere to PEG hydrogel functionalized with IKVAV peptide. On the contrary, a monolayer was established when ECVs were seeded on PEG hydrogel functionalized with RGD, seen in fig. 23B. Macarak et al. claim that fibronectin promotes greater ECs adhesion than laminin-1 in 2D [185]. This is consistent with a previous study, where Salaszynk et al. concluded that each ECM protein binds to a certain integrin to induce cell differentiation and adhesion at varying affinities, with cells binding 6 folds greater in the presence of fibronectin rather than

laminin-1 [186]. Nuttelman et al. further suggest that the strongly hydrophilic PEG might restrict the activity of the less hydrophilic IKVAV, while attracting the more hydrophilic RGD [187]. Therefore, solely incorporating IKVAV in PEG networks might mask its ability to promote cell adhesion and migration. Rather IKVAV should be combined with another adhesion peptide, such as RGD, to enhance its signal within a PEG network. This is consistent with our finding, where the combination of RGD and IKVAV (1:1) positively influenced the formation of an endothelial monolayer, seen in fig. 23C.

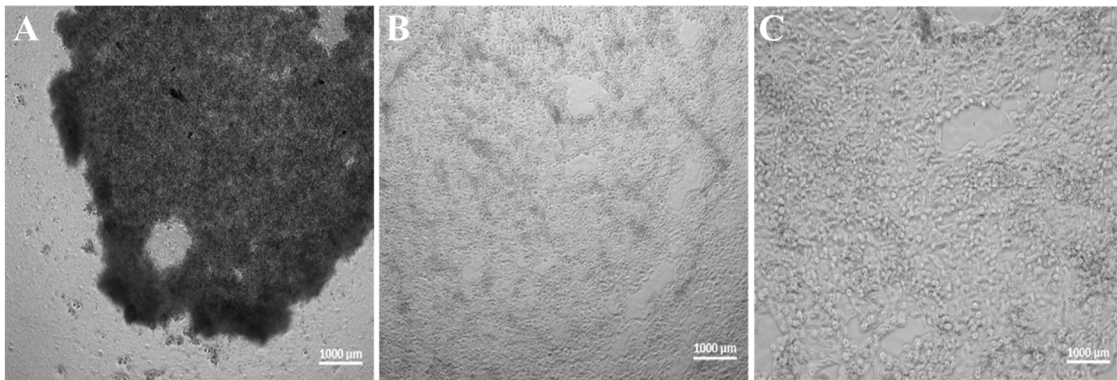


**Figure 23:** ECVs seeded on top of PEG hydrogel functionalized with [A] IKVAV-300 µM [B] RGD-600 µM [C] IKVAV:RGD-300. ECVs did not adhere when IKVAV was solely incorporated (Image A). ECVs adhered and formed a monolayer when RGD was solely (B) and combined with IKVAV (C). Images were taken using an inverted light microscope. Scale bar=1000 µm, (n=3).

The establishment of an endothelial monolayer via joining of adjacent ECs by TJs is critical for bio-mimicking the *in vivo* BBB microenvironment. Since the sole incorporation of IKVAV in PEG failed in doing so, this condition was excluded from further analysis.

### 3. Transendothelial Electrical Resistance (TEER)

To assess the barrier integrity of the model, TEER of the generated ECV monolayer was measured for 5 consecutive days. The conditions were: (1) IKVAV:RGD-300  $\mu\text{M}$  with encapsulated NHA, (2) RGD-600  $\mu\text{M}$  with encapsulated NHA, (3) IKVAV:RGD-300  $\mu\text{M}$  control, (4) RGD-600  $\mu\text{M}$  control, and (5-6) 2D controls (NHA and ECV co-culture; ECV monoculture).

As illustrated in fig. 24, a similar increase in TEER was observed in all conditions in the 5-days timeframe. One-way ANOVA analysis revealed a statistically significant difference in TEER of each sample at days 1 and 5 ( $p\text{-value}\leq 0.001$ ). Regardless of time, IKVAV:RGD-300  $\mu\text{M}$  with encapsulated NHA recorded the highest TEER among all conditions. Specifically, TEER significantly increased from  $29.83\pm 1.31 \Omega\cdot\text{cm}^2$  at day 1 to  $55.33\pm 1.47 \Omega\cdot\text{cm}^2$  at day 5. Likewise, RGD-600  $\mu\text{M}$  with encapsulated NHA recorded a significant increase in TEER from  $27.43\pm 1.09 \Omega\cdot\text{cm}^2$  at day 1 to  $50.46\pm 0.42 \Omega\cdot\text{cm}^2$  at day 5. TEER of IKVAV:RGD-300  $\mu\text{M}$  control significantly increased from  $18.33\pm 3.86 \Omega\cdot\text{cm}^2$  at day 1 to  $42\pm 0.82 \Omega\cdot\text{cm}^2$  at day 5. These values are comparable to TEER recorded for RGD-600  $\mu\text{M}$  control between days 1 and 5, where it increased from  $19.73\pm 1.32 \Omega\cdot\text{cm}^2$  to  $39\pm 0.42 \Omega\cdot\text{cm}^2$ . This shows that combining IKVAV and RGD (1:1) enhanced the barrier function of the monolayer relative to incorporating RGD alone. TEER recorded at days 1 and 5 for the 2D co-culture and monoculture controls also showed a significant increase from  $21.3\pm 0.4 \Omega\cdot\text{cm}^2$  to  $31.2\pm 0.4 \Omega\cdot\text{cm}^2$ , and from  $11.5\pm 2.3 \Omega\cdot\text{cm}^2$  to  $19.8\pm 2.2 \Omega\cdot\text{cm}^2$ , respectively. All of the established monolayers showed stability and enhanced tightness over this timeframe, until reaching a steady state by day 5, indicating the maximum formation of TJs [150].

To confirm the impact of co-culturing NHA and ECVs in a 3D scaffold in the presence of major BM peptides, one-way ANOVA analysis was performed to compare TEER at day 5 between all conditions. Interestingly, TEER of IKVAV:RGD-300  $\mu\text{M}$  with encapsulated NHA and RGD-600  $\mu\text{M}$  with encapsulated NHA, were significantly higher than all other conditions ( $p\text{-value} \leq 0.001$ ). Actually, TEER of all PEG hydrogels was significantly higher than the 2D culture systems ( $p\text{-value} \leq 0.001$ ). Likewise, co-culturing ECV with NHA, regardless of other variables, induced greater TEER compared to their relative controls ( $p\text{-value} \leq 0.001$ ). Relatedly, Zhang et al. previously found that co-culturing astrocytes and porcine BCECs enhanced TEER of the established endothelium [188]. This can be attributed to the role of astrocytes in secreting chemical signals that have been shown to induce the expression of BBB ECs phenotype [189]. Abbott et al. suggest that these secretions promote the polarization of ECs transporters and TJs expression, resulting in an enhanced barrier integrity [10]. The obtained results further reflect the effect of maintaining a nonplanar dimensionality on the activity astrocytes to induce cell-cell and cell-matrix interactions similar to the *in vivo* BBB milieu. Planar dimensionality has been shown to affect the astrocytes phenotype, as the activity of astrocytes in 2D would not resemble a physiological state due to their inability to interact with their surrounding [190].

Although no statistical significance in TEER was detected between IKVAV:RGD-300  $\mu\text{M}$  and RGD-600  $\mu\text{M}$ , conditions with a combined 300 $\mu\text{M}$ -300 $\mu\text{M}$  of peptides showed an enhanced TEER. This shows that the co-presence of fibronectin-mimetic peptide RGD and laminin-mimetic peptide IKVAV interfere in enhancing the expression of TJ proteins. This is consistent with a previous study, where Tilling et al. found that combining a (1:1) mixture of fibronectin and laminin significantly enhances



TEER of porcine BCECs [80]. Having said that, the cumulative effect of co-culturing astrocytes and ECs in 3D in the presence of IKVAV and RGD resulted in an improved barrier integrity.

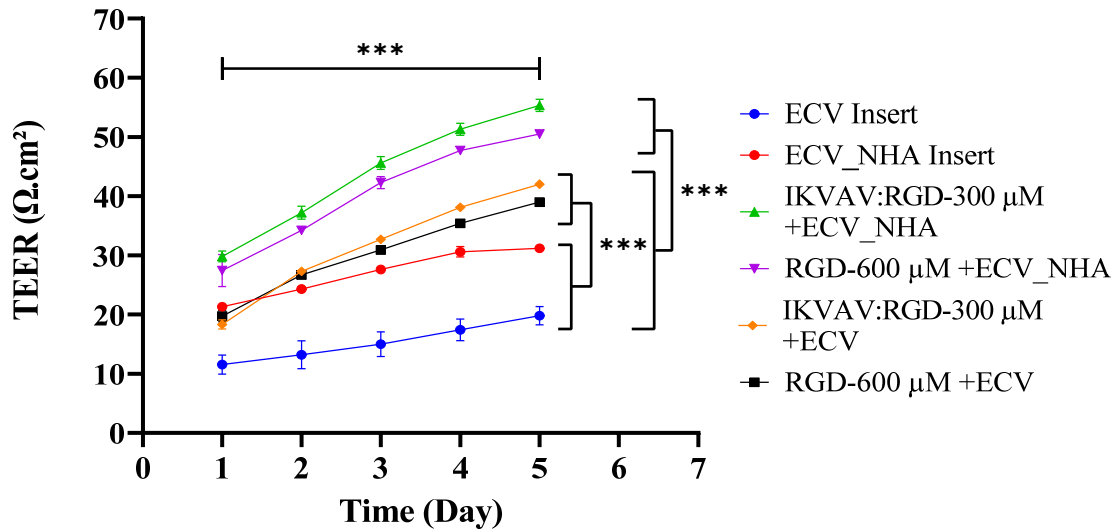


**Figure 24:** Corrected TEER values ( $\Omega \cdot \text{cm}^2$ ) for different samples recorded at days 1 to 5 using EVOM2 and STX2 electrodes. One-way ANOVA analysis was performed to determine the statistical difference between TEER at days 1 and 5 of each condition. One-way ANOVA was also performed to detect any statistically significant difference in TEER of different samples at day 5. TEER of IKVAV:RGD-300  $\mu\text{M}$  with encapsulated NHA was significantly higher than the other samples. TEER of functionalized PEG hydrogels controls was significantly higher than the 2D monoculture and co-culture controls. P-value  $\leq 0.05$  was considered significant. P-value  $\leq 0.001$  was marked with (\*\*\*) . Error bars represent +/- SEM, (n=3).

#### 4. Permeability Assay

An optimal *in vitro* BBB model is characterized by not only high TEER but also low permeability of molecules across the endothelium. The higher the expression of TJs, the stricter the paracellular transport of molecules, including small molecules such as Na-F. Similarly, the highly selective transport of molecules should restrict the flow of large molecules, such as albumin, across the endothelium. A permeability assay was

performed to the same conditions used in TEER measurements, to evaluate the ability of two tracers, EBA and Na-F, to cross the endothelium at four time-points (30 min, 60 min, 90 min, and 120 min). The concentrations across PEG hydrogels were compared to the concentration across an 8  $\mu\text{m}$  blank insert, while the concentrations across the 2D controls (monoculture and co-culture) were compared to that of a 0.4  $\mu\text{m}$  blank insert. Two-way ANOVA analysis was used to determine any statistical difference between the concentration obtained for all the conditions at the same time-point, and that obtained at 30 min and at 120 min for the same condition.

Regardless of time, fig. 25 demonstrates that EBA was least permeable when ECVs were co-cultured with NHA encapsulated in IKVAV:RGD-300  $\mu\text{M}$ . Expectedly, this condition had also recorded the highest TEER. EBA concentration increased from  $0.036\pm 0.022$   $\mu\text{g/mL}$  to  $0.216\pm 0.055$   $\mu\text{g/mL}$  between 30 min and 120 min, with no significant difference. In fact, EBA permeability for all conditions at this extended timeframe increased without any significance. EBA permeability RGD-600  $\mu\text{M}$  with encapsulated NHA increased from  $0.058\pm 0.045$   $\mu\text{g/mL}$  to  $0.32\pm 0.06$   $\mu\text{g/mL}$  during the timeframe. IKVAV:RGD-300  $\mu\text{M}$  control and RGD-600  $\mu\text{M}$  control, ranked the third ( $0.238\pm 0.09$   $\mu\text{g/mL}$  to  $0.49\pm 0.154$   $\mu\text{g/mL}$ ) and fourth ( $0.26\pm 0.112$   $\mu\text{g/mL}$  to  $0.63\pm 0.077$   $\mu\text{g/mL}$ ) lowest EBA permeability, respectively. While the permeability of EBA did not significantly differ between these samples, IKVAV:RGD-300  $\mu\text{M}$  with encapsulated NHA induced a better barrier. Cai et al. found that the loss of BM peptides, specially laminin, trigger BBB leakage [191]. Similarly, the downregulation of fibronectin contributes to the hyperpermeability of the BBB in pathophysiology [192]. Interestingly, these BM peptides generated by the endothelial cells and astrocytes, later adhere to these cells to maintain the barrier integrity [193]. Astrocytes further interact

with other molecules, such as angiotensin, to decrease the permeability of the BBB [194]. Accordingly, the disruption of any of these cell-cell or cell-matrix interactions increase the permeability.

EBA permeability across the 2D controls (monoculture and co-culture) were not only higher than that of PEG hydrogels but also insignificantly different from the permeability across their corresponding 0.4  $\mu\text{m}$  blank insert. EBA permeability of the 2D monoculture and co-culture increased from  $0.551 \pm 0.089 \mu\text{g/mL}$  to  $1.322 \pm 0.056 \mu\text{g/mL}$ , and from  $0.327 \mu\text{g/mL}$  to  $0.797 \pm 0.07 \mu\text{g/mL}$ , respectively. This can be attributed to the role of astrocytic-endfeet in interacting with its 3D surrounding to prevent hyperpermeability, similar to the *in vivo* BBB milieu [195].

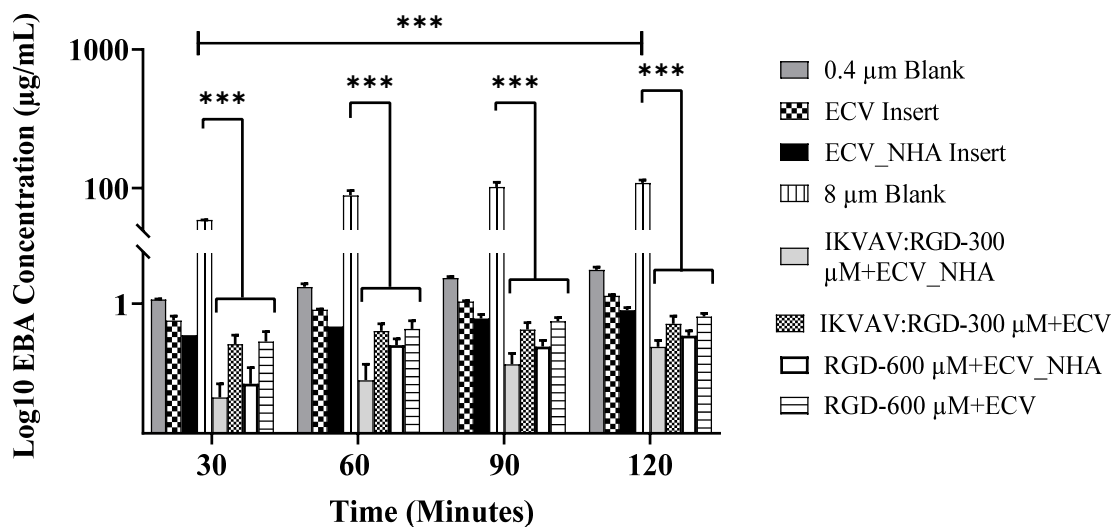


**Figure 25:** EBA Permeability Assay: Log<sub>10</sub> concentration of the Evan’s Blue Bound to Albumin (EBA; µg/mL) under different functionalized PEG conditions at four time-points (30, 60, 90, and 120 mins). Two-way ANOVA analysis was performed to determine any statistical difference between the same sample at 30 mins and 120 mins; and at a particular time-point for all PEG hydrogels relative to 8 µm blank, monoculture and co-culture relative to each other and the 0.4 µm blank, samples with/without NHA, IKVAV:RGD-300 µM, and RGD-600 µM. Functionalized PEG hydrogels (with/without astrocytes) showed a significantly lower EBA permeability. P-value ≤ 0.05 was considered significant. P-value ≤ 0.001 was marked with (\*\*\*). Error bars represent +/- SEM, (n=2).

A similar trend was seen with the permeability of Na-F across the monolayer of the various studied conditions at four time-points (fig. 26). However, Na-F permeability between all conditions did not change much. Among PEG hydrogels, Na-F was least permeable across IKVAV:RGD-300 µM with encapsulated NHA (140.437±0.441 ng/mL at 120 min), followed RGD-600 µM with encapsulated NHA (144.598±0.22 ng/mL at 120 min), RGD-600 µM control (164.882±6.108 ng/mL at 120 min), and then IKVAV:RGD-300 µM (165.668±11.943 ng/mL at 120 min). Na-F permeability in all functionalized PEG hydrogels (with/without astrocytes) was significantly lower than that across the 8 µm blank insert (p-value ≤ 0.001). Interestingly, 2D controls showed a more restricted Na-F flow, where 99.79615±1.202 ng/mL of Na-F crossed the 2D co-

culture control at 120 min, and  $118.968 \pm 3.942$  ng/mL crossed the 2D monoculture at 120 min, with no significance difference compared to the  $0.4\mu\text{m}$  blank insert. These findings show that even small polar molecules, such as Na-F, cannot freely cross the established endothelia.

These findings demonstrate that our suggested *in vitro* BBB model succeeds in creating a barrier that not only prevents the flow of large molecules but also limits the paracellular flow of Na-F. High TEER and low permeability concurrently characterized this promising model. This can be attributed to the cumulative effect of incorporating astrocytes and peptides in a 3D system on improving the barrier function [150].

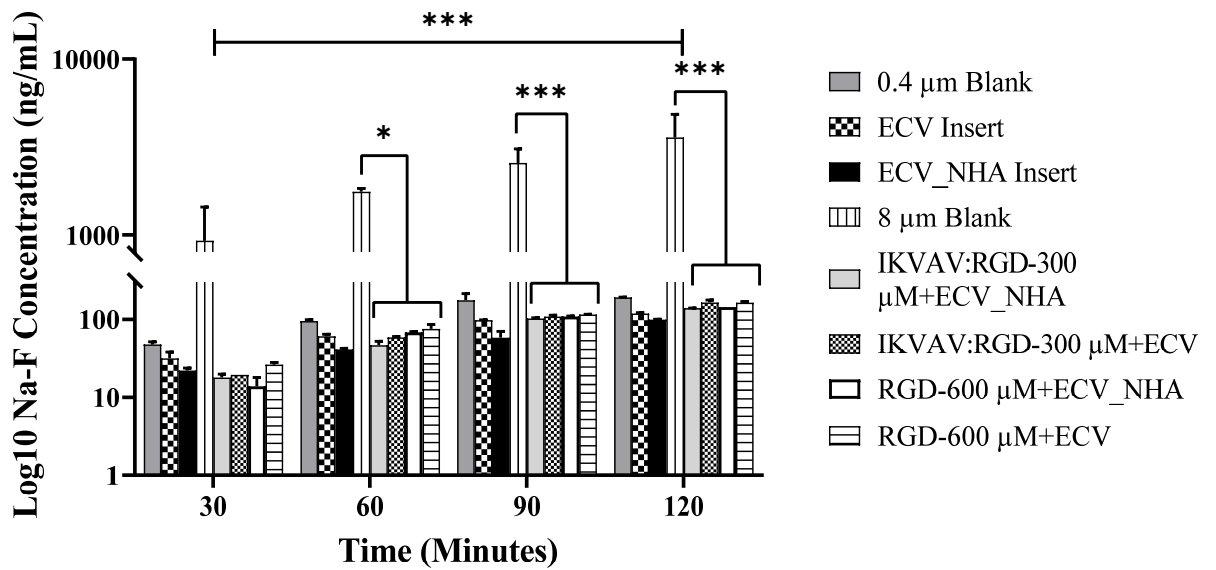


**Figure 26:** Na-F Permeability Assay: Log10 concentration of the Sodium Fluorescein (Na-F; ng/mL) under different functionalized PEG conditions at four time-points (30, 60, 90, and 120 mins). Two-way ANOVA analysis was performed to determine any statistical difference between the same sample at 30 mins and 120 mins; and at a particular time-point for all PEG hydrogels relative to 8 μm blank, monoculture and co-culture relative to each other and the 0.4 μm blank, samples with/without NHA, IKVAV:RGD-300 μM, and RGD-600 μM. P-value  $\leq 0.05$  was considered significant. P-value  $\leq 0.001$  was marked with (\*\*\*). Error bars represent +/- SEM, (n=2).

## 5. ZO-1 and GFAP Characterization

To evaluate the formation of TJs between adjacent ECVs, immunofluorescence staining of ZO-1 was done under the same conditions. Ideally, ZO-1 should form a continuous network surrounding ECs. As illustrated in fig. 27, ZO-1 expression in 3D PEG hydrogels was greater than that in 2D controls. Specifically, ECVs seeded on functionalized PEG hydrogels with encapsulated astrocytes expressed the highest ZO-1 expression, with a slightly better signal in IKVAV:RGD-300 μM (fig. 27F), compared to RGD-600 μM (fig. 27E). This trend was also observed when comparing the ZO-1 signal between IKVAV:RGD-300 μM control (fig. 27D), and RGD-300 μM control (fig. 27C). Accordingly, the combination of laminin-mimetic peptide IKVAV and

fibronectin-mimetic peptide RGD further induce the formation of tight junctions relative to the sole presence of RGD. This can be attributed to the role of laminin-mimetic peptide IKVAV in enhancing expression of TJs. Yao et al. showed that the loss of astrocytic laminin, especially laminin-1, halts the expression of TJs by disrupting the astrocytic polarization and signaling [83].

Comparing the ZO-1 signal between astrocyte-containing conditions and astrocytes-deprived conditions demonstrates the role of astrocytes in enhancing the barrier integrity, reflected by the enhanced expression of ZO-1. It can be suggested that astrocytes do so via neighboring cell-cell interaction and cell-matrix interactions, enabling them to release chemical factors crucial in TJs formation. For example, TGF- $\beta$  released by the astrocytic endfeet, after interacting with pericytes *in vivo*, has been shown to increase the expression of tight junction proteins, such as claudin-5 [66]. This is consistent with a previous study, where Gardner et al. claimed that astrocytes secrete integrins that enhance the barrier function and tight junction protein expression, demonstrated by high TEER and ZO-1 content [196]. Wu et al. further suggest that molecules, such as angiotensin, targets astrocytes to help restore the expression of ZO-1 and claudin-5 during pathology [194]. The 3D structure of PEG hydrogels had also proved to be critical in triggering the expression of ZO-1. As seen in fig. 27, the 2D controls (fig. 27 A and B) show a minimal expression of ZO-1, relative to the 3D models (fig. 27 C-F). This can be further attributed to the ability of astrocytes to protrude and directly interact in 3D via their endfeet with neighboring cells and proteins, leading to an enhanced expression of TJs and barrier integrity [197].

ZO-1/DAPI intensity ratio was further analyzed using ImageJ, where the obtained results validated our previous findings (fig. 28). One-way ANOVA analysis

showed that IKVAV:RGD-300  $\mu\text{M}$  and RGD-600  $\mu\text{M}$  (with/without NHA) had a significantly greater ratio of ZO-1/DAPI compared to 2D controls ( $p\text{-value}\leq 0.001$ ). Specifically, IKVAV:RGD-300  $\mu\text{M}$  and RGD-600  $\mu\text{M}$  with encapsulated NHA has the highest ZO-1/DAPI ratio among all conditions.

While these findings show the significance of our *in vitro* BBB model, the generated ZO-1 expression fails to produce a well-defined network between neighboring ECs on both 3D and 2D systems. The irregularities might be attributed to the use of ECVs, rather than primary BCECs. Gaillard et al. claims that immortalized ECs do not only fail to mimic the *in vivo* BBB ECs phenotype but also may reflect pathological properties of BBB [198].



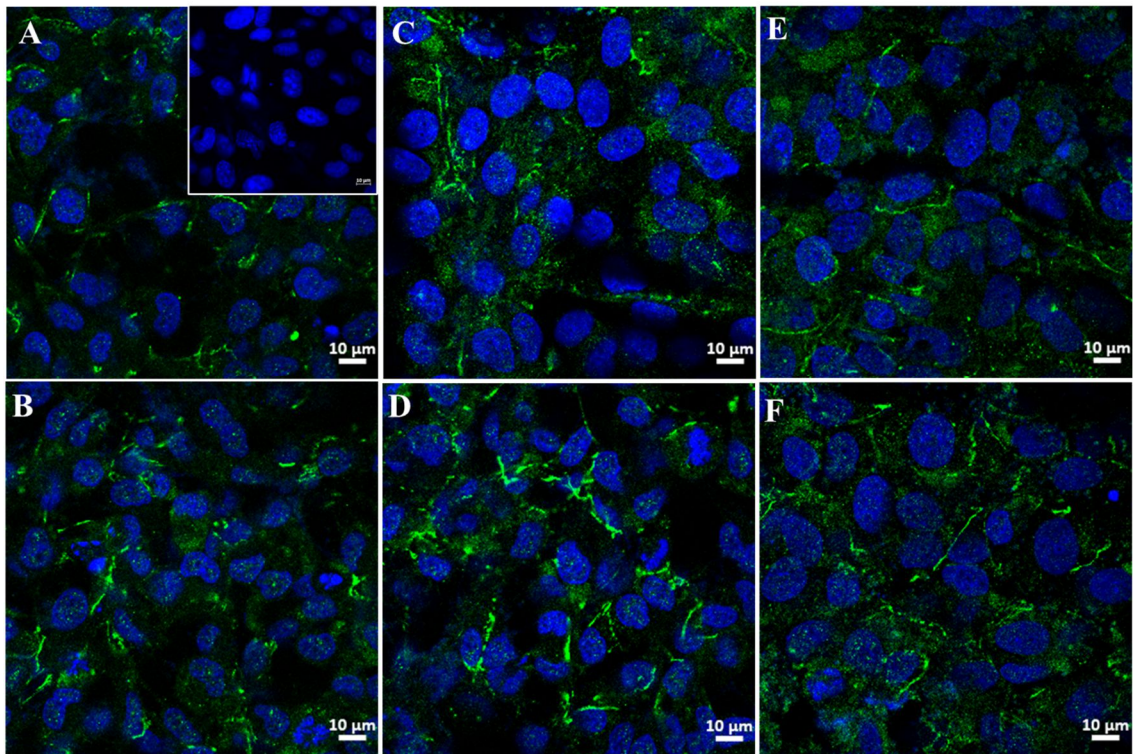


**Figure 27:** ZO-1 staining of ECVs in [A] ECV monoculture control; negative control [B] ECV and NHA co-culture control [C] RGD-600 µM control [D] IKVAV:RGD-300 µM control [E] RGD-600 µM with encapsulated astrocytes [F] IKVAV:RGD-300 µM with encapsulated NHA. Images were taken using a confocal laser scanning microscope (63x). Scale bar=10 µm, (n=2).

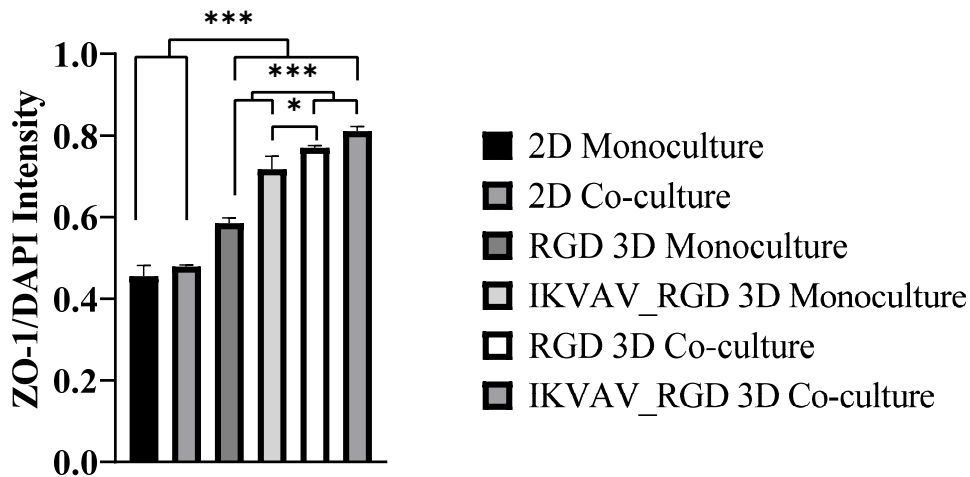


**Figure 28:** ZO-1/DAPI intensity ratio of each condition quantified using ImageJ. Functionalized PEG hydrogels with encapsulated astrocytes show the highest intensity. One-way ANOVA analysis was used to determine any statistical difference in ZO-1/DAPI intensity between samples. Results show that IKVAV:RGD-300  $\mu\text{M}$  and RGD-600  $\mu\text{M}$  (with/without astrocytes) had a significantly greater expression of ZO-1/DAPI compared to 2D controls. IKVAV:RGD-300  $\mu\text{M}$  and RGD-600  $\mu\text{M}$  with encapsulated NHA had a significantly greater expression of ZO-1/DAPI compared to 2D and 3D controls. P-value  $\leq 0.05$  was considered significant (\*). P-value  $\leq 0.001$  was marked with (\*\*\*). Error bars represent +/- SEM.

To identify the astrocytic morphology, GFAP immunostaining of astrocytic processes was performed on functionalized PEG hydrogels loaded with astrocytes and compared to the 2D co-culture control. As illustrated in fig. 29, GFAP intensity was neither significant nor differed between these conditions. GFAP/DAPI intensity ratio was further analyzed using ImageJ, where the obtained results validated these findings (fig. 30). One-way ANOVA analysis showed no significant difference in this ratio. This might be attributed to the cell passage number of NHA used in this experiment (P6-P7), as studies have shown that late passages affect the morphological, functional, and molecular properties of astrocytes [199]. However, it can be noticed that astrocytes embedded in functionalized PEG hydrogels (fig. 29A and 29B), regardless of the peptides, show an extended morphology, unlike the control where cells mostly grew in

clumps with no defined borders (fig. 29C). This can be attributed to the effect of a 3D milieu on the activity of the encapsulated astrocytes. This is consistent with a previous study, where Balasubramanian et al. found that astrocytes grown in a 3D hydrogel triggered a heterogeneous spread morphology compared to the round morphology in 2D [200].

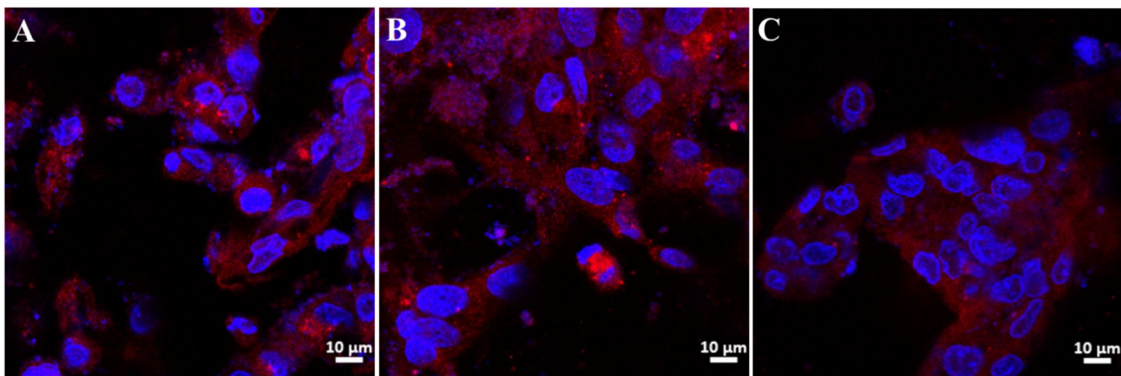


**Figure 29:** GFAP immunostaining of NHA in [A] IKVAV:RGD-300  $\mu\text{M}$  with encapsulated NHA [B] RGD-600  $\mu\text{M}$  with encapsulated astrocytes [C] ECV and NHA co-cultured on insert. Images were taken using a confocal laser scanning microscope (63x). Scale bar=10  $\mu\text{m}$ , (n=2).

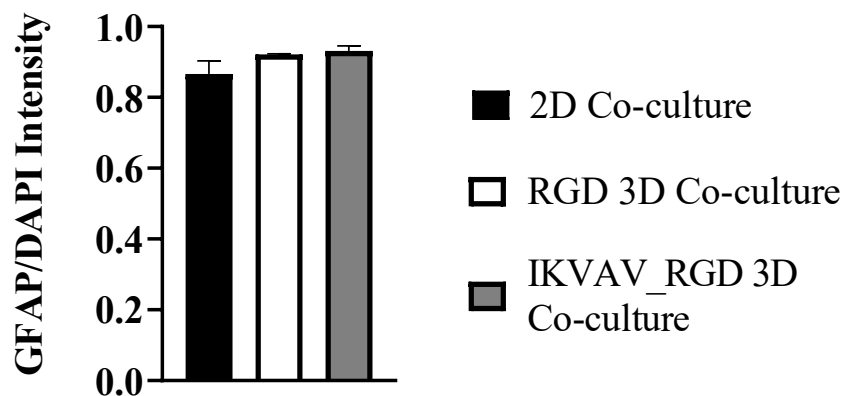


**Figure 30:** GFAP/DAPI intensity ratio of each condition quantified using ImageJ. No difference was found between samples. No significant difference was detected. Error bars represent +/- SEM.

## CHAPTER VI

### CONCLUSION

The BBB is a highly selective semipermeable interface that separates the brain from the circulatory system, protecting the brain and maintain homeostasis. Several neurological diseases have been associated with the breakdown of the BBB. For example, AD is characterized by the accumulation of amyloid- $\beta$  peptide in the brain, leading to inflammation and disruption of the BBB. The BBB integrity is maintained by the cumulative action of the NVU components on the endothelium. Downregulation of any molecule or cell can have a disastrous effect on the BBB barrier integrity. Understanding how the BBB's constituents function and interact, as well as the impairments, reveals specifically how the BBB is maintained and how neurological diseases are initiated and progressed. This is crucial for not only developing targeted treatments but also in inducing successful drug delivery across this tight barrier. There has been a growing interest in developing an *in vitro* model that bio-mimics the *in vivo* BBB in physiology and pathology. A successful model is that capable of integrating the major cell types and ECM components in a 3D milieu. PEG hydrogels are extensively used in tissue engineering, as they offer an inert, biocompatible, biodegradable, flexible, reproducible, and inexpensive 3D scaffold for cell encapsulation and peptide integration.

In this project, we developed a novel functionalized PEG hydrogel *in vitro* model of the BBB. In brief, PEG-VS was modified with laminin-mimetic peptide IKVAV and/or fibronectin-mimetic peptide RGD, and then crosslinked with MMP-sensitive peptides via a Michael-type addition of thiol. While astrocytes were encapsulated within the hydrogel, ECs seeded on top formed a monolayer. The presence

of these crucial ECM peptides, in addition to co-culturing astrocytes and ECs in a biocompatible 3D milieu, was expected to induce the *in vivo* cell-cell and cell-matrix interactions. Initially, the optimal IKVAV concentration for the viability of astrocytes was determined by a Live/Dead assay. Incorporating 300  $\mu\text{M}$  of IKVAV showed to be optimal for the survival of astrocytes. However, ECs failed to adhere to PEG hydrogels functionalized solely with IKVAV. Accordingly, only PEG hydrogels functionalized with 600  $\mu\text{M}$  RGD and a one-to-one mixture of RGD and IKVAV were further tested. To evaluate the sole and cumulative effect of IKVAV, RGD, astrocytes, and dimensionality on the barrier integrity, we assessed the activity of the endothelial monolayer at different conditions. The expression of TJs was determined qualitatively and quantitatively by assessing the TEER and Na-F permeability, and ZO-1 expression, respectively. The transcellular transport was also evaluated by EBA permeability assay. The activation and spreading of astrocytes were determined by qualitatively evaluating GFAP expression. PEG hydrogels functionalized with RGD and IKVAV (300 $\mu\text{M}$ -300 $\mu\text{M}$ ), with encapsulated astrocytes proved to have the greatest barrier integrity, reflected by highest TEER, lowest permeability, enhanced ZO-1 expression, and relatively extended GFAP expression.

Accordingly, this model presents a promising approach for bio-mimicking the BBB *in vitro* to be eventually used in neurological disease studies and offer reliable drug delivery results. To improve the barrier integrity, ECVs should be substituted with brain ECs, as it is expected to enhance the TEER, permeability, and the expression of ZO-1. The claudin-5 expression should be also assessed as it is the only identified TJ protein until today to be directly associated with the low BBB permeability [201]. In an attempt to further resemble the *in vivo* milieu, collagen-IV mimetic peptide GFOGER

will be integrated into our model to evaluate its effect on the BBB integrity. Optimizing the parameters of this model will produce a superior scaffold for understanding the BBB in physiology and pathology to develop targeted drugs and successful delivery.

## REFERENCES

1. Hoff, F., *How to Prepare Your Specimen for Immunofluorescence Microscopy*, in *leica-microsystems*. 2015.
2. (WHO), W.H.O. *The world health report 2002 - Reducing Risks, Promoting Healthy Life*. 2002; Available from: <https://www.who.int/whr/2002/en/>.
3. Feigin, V.L., et al., *Global, regional, and national burden of neurological disorders, 1990–2016: a systematic analysis for the Global Burden of Disease Study 2016*. *The Lancet Neurology*, 2019. **18**(5): p. 459-480.
4. Yao, Y. and S.E. Tsirka, *Monocyte chemoattractant protein-1 and the blood–brain barrier*. *Cellular and molecular life sciences*, 2014. **71**(4): p. 683-697.
5. Kook, S.-Y., et al., *Disruption of blood-brain barrier in Alzheimer disease pathogenesis*. *Tissue Barriers*, 2013.
6. Zenaro, E., G. Piacentino, and G. Constantin, *The blood-brain barrier in Alzheimer's disease*. *Neurobiology of Disease*, 2017.
7. Montagne, A., Z. Zhao, and B.V. Zlokovic, *Alzheimer's disease: A matter of blood–brain barrier dysfunction?* *Journal of Experimental Medicine* 2017.
8. Abbott, N.J., et al., *Structure and function of the blood–brain barrier*. *Neurobiology of disease*, 2010. **37**(1): p. 13-25.
9. Cserr, H.F. and M. Bundgaard, *Blood-brain interfaces in vertebrates: a comparative approach*. *American Journal of Physiology-Regulatory, Integrative and Comparative Physiology*, 1984. **246**(3): p. R277-R288.
10. Abbott, N.J., L. Rönnbäck, and E. Hansson, *Astrocyte–endothelial interactions at the blood–brain barrier*. *Nature reviews neuroscience*, 2006. **7**(1): p. 41.
11. Nakagawa, S., et al., *A new blood–brain barrier model using primary rat brain endothelial cells, pericytes and astrocytes*. *Neurochemistry international*, 2009. **54**(3-4): p. 253-263.
12. Bell, A.H., et al., *The neurovascular unit: effects of brain insults during the perinatal period*. *Frontiers in neuroscience*, 2020. **13**: p. 1452.
13. Wolburg, H. and A. Lippoldt, *Tight junctions of the blood–brain barrier: development, composition and regulation*. *Vascular pharmacology*, 2002. **38**(6): p. 323-337.
14. Garcia, J. and K.L. Schaphorst, *Regulation of endothelial cell gap formation and paracellular permeability*. *Journal of investigative medicine: the official publication of the American Federation for Clinical Research*, 1995. **43**(2): p. 117-126.
15. Pardridge, W.M., *Blood-brain barrier drug targeting: the future of brain drug development*. *Molecular interventions*, 2003. **3**(2): p. 90.
16. Boado, R.J., et al., *Selective expression of the large neutral amino acid transporter at the blood–brain barrier*. *Proceedings of the National Academy of Sciences*, 1999. **96**(21): p. 12079-12084.
17. Pardridge, W.M., *Biopharmaceutical drug targeting to the brain*. *Journal of drug targeting*, 2010. **18**(3): p. 157-167.
18. Bazzoni, G., *Endothelial tight junctions: permeable barriers of the vessel wall*. *THROMBOSIS AND HAEMOSTASIS-STUTTGART-*, 2006. **95**(1): p. 36.
19. Haddad-Tóvolli, R., et al., *Development and function of the blood-brain barrier in the context of metabolic control*. *Frontiers in neuroscience*, 2017. **11**: p. 224.

20. Michael V. Sofroniew corresponding and H.V. Vinters, *Astrocytes: biology and pathology*. Acta Neuropathol., 2010.
21. J.M.Herdon, M.E.Tome, and T.P.Davis, *Chapter 9 - Development and Maintenance of the Blood–Brain Barrier*, in *Primer on Cerebrovascular Diseases (Second Edition)*. 2017, Academic Press. p. 51-56.
22. Daneman, R., et al., *Pericytes are required for blood–brain barrier integrity during embryogenesis*. Nature, 2010. **468**(7323): p. 562-566.
23. Armulik, A., G. Genové, and C. Betsholtz, *Pericytes: developmental, physiological, and pathological perspectives, problems, and promises*. Developmental cell, 2011. **21**(2): p. 193-215.
24. Thomsen, M.S., L.J. Routhe, and T. Moos, *The vascular basement membrane in the healthy and pathological brain*. Journal of Cerebral Blood Flow & Metabolism, 2017. **37**(10): p. 3300-3317.
25. Rist, R.J., et al., *F-actin cytoskeleton and sucrose permeability of immortalised rat brain microvascular endothelial cell monolayers: effects of cyclic AMP and astrocytic factors*. Brain research, 1997. **768**(1-2): p. 10-18.
26. Rubin, L., et al., *A cell culture model of the blood-brain barrier*. The Journal of cell biology, 1991. **115**(6): p. 1725-1735.
27. Perrière, N., et al., *A functional in vitro model of rat blood–brain barrier for molecular analysis of efflux transporters*. Brain research, 2007. **1150**: p. 1-13.
28. Hoheisel, D., et al., *Hydrocortisone reinforces the blood–brain barrier properties in a serum free cell culture system*. Biochemical and biophysical research communications, 1998. **244**(1): p. 312-316.
29. Obermeier, B., R. Daneman, and R.M. Ransohoff, *Development, maintenance and disruption of the blood-brain barrier*. Nature medicine, 2013. **19**(12): p. 1584.
30. Helms, H.C., et al., *In vitro models of the blood–brain barrier: an overview of commonly used brain endothelial cell culture models and guidelines for their use*. Journal of Cerebral Blood Flow & Metabolism, 2016. **36**(5): p. 862-890.
31. Wilhelm, I. and I.A. Krizbai, *In vitro models of the blood–brain barrier for the study of drug delivery to the brain*. Molecular pharmaceutics, 2014. **11**(7): p. 1949-1963.
32. Bowman, P.D., et al., *Primary culture of capillary endothelium from rat brain*. In vitro, 1981. **17**(4): p. 353-362.
33. He, Y., et al., *Cell-culture models of the blood–brain barrier*. Stroke, 2014. **45**(8): p. 2514-2526.
34. Yang, S., et al., *The design of scaffolds for use in tissue engineering. Part I. Traditional factors*. Tissue engineering, 2001. **7**(6): p. 679-689.
35. Ahmed, E.M., *Hydrogel: Preparation, characterization, and applications: A review*. Journal of advanced research, 2015. **6**(2): p. 105-121.
36. Li, Y., et al., *Magnetic hydrogels and their potential biomedical applications*. Advanced Functional Materials, 2013. **23**(6): p. 660-672.
37. Drury, J.L. and D.J. Mooney, *Hydrogels for tissue engineering: scaffold design variables and applications*. Biomaterials, 2003. **24**(24): p. 4337-4351.
38. Banerjee, S.S., et al., *Poly (ethylene glycol)-prodrug conjugates: concept, design, and applications*. Journal of drug delivery, 2012. **2012**.



39. Day, J.R., et al., *The impact of functional groups of poly (ethylene glycol) macromers on the physical properties of photo-polymerized hydrogels and the local inflammatory response in the host*. *Acta biomaterialia*, 2018. **67**: p. 42-52.
40. (WHO), W.H.O. *Dementia*. 2020; Available from: <https://www.who.int/news-room/fact-sheets/detail/dementia>.
41. Moretti, R., et al., *Blood-brain barrier dysfunction in disorders of the developing brain*. *Frontiers in Neuroscience*, 2015. **9**(40).
42. Rosenberg, G.A., *Neurological Diseases in Relation to the Blood–Brain Barrier*. *Journal of Cerebral Blood Flow & Metabolism*, 2012.
43. Association, A.s. *What is Alzheimer’s Disease?* 2021; Available from: <https://www.alz.org/alzheimers-dementia/what-is-alzheimers>.
44. Aging, T.N.I.o. *Alzheimer's Disease Fact Sheet*. 2021; Available from: <https://www.nia.nih.gov/health/alzheimers-disease-fact-sheet>.
45. (WHO), W.H.O., *The top 10 causes of death*. 2020.
46. Ballabh, P., A. Braun, and M. Nedergaard, *The blood–brain barrier: an overview: structure, regulation, and clinical implications*. *Neurobiology of disease*, 2004. **16**(1): p. 1-13.
47. Begley, D.J. and M.W. Brightman, *Structural and functional aspects of the blood-brain barrier*. *Peptide transport and delivery into the central nervous system*, 2003: p. 39-78.
48. Cecchelli, R., et al., *Modelling of the blood–brain barrier in drug discovery and development*. *Nature reviews Drug discovery*, 2007. **6**(8): p. 650-661.
49. Barichello, T., et al., *An overview of the blood-brain barrier*. *Blood-Brain Barrier*, 2019: p. 1-8.
50. Wolburg, H., et al., *Brain endothelial cells and the glio-vascular complex*. *Cell and tissue research*, 2009. **335**(1): p. 75-96.
51. Baeten, K.M. and K. Akassoglou, *Extracellular matrix and matrix receptors in blood–brain barrier formation and stroke*. *Developmental neurobiology*, 2011. **71**(11): p. 1018-1039.
52. Demeule, M., et al., *Drug transport to the brain: key roles for the efflux pump P-glycoprotein in the blood–brain barrier*. *Vascular pharmacology*, 2002. **38**(6): p. 339-348.
53. Huber, J.D., R.D. Egleton, and T.P. Davis, *Molecular physiology and pathophysiology of tight junctions in the blood–brain barrier*. *Trends in neurosciences*, 2001. **24**(12): p. 719-725.
54. Anderson, J.M. and C.M. Van Itallie, *Physiology and function of the tight junction*. *Cold Spring Harbor perspectives in biology*, 2009. **1**(2): p. a002584.
55. Zhao, Z., et al., *Establishment and dysfunction of the blood-brain barrier*. *Cell*, 2015. **163**(5): p. 1064-1078.
56. Pardridge, W.M. and W.H. Oldendorf, *TRANSPORT OF METABOLIC SUBSTRATES THROUGH THE BLOOD-BRAIN BARRIER I*. *Journal of neurochemistry*, 1977. **28**(1): p. 5-12.
57. Daneman, R. and A. Prat, *The blood–brain barrier*. *Cold Spring Harbor perspectives in biology*, 2015. **7**(1): p. a020412.
58. Butt, A.M., H.C. Jones, and N.J. Abbott, *Electrical resistance across the blood-brain barrier in anaesthetized rats: a developmental study*. *Journal of Physiology* 1990.

59. Crone, C. and O. Christensen, *Electrical resistance of a capillary endothelium*. The Journal of general physiology, 1981. **77**(4): p. 349-371.
60. Butt, H.-J., K.H. Downing, and P.K. Hansma, *Imaging the membrane protein bacteriorhodopsin with the atomic force microscope*. Biophysical journal, 1990. **58**(6): p. 1473-1480.
61. Larsen, A.B., *The blood-brain barrier in vitro using primary culture: implications for studies of therapeutic gene expression and iron transport*. 2014: River Publishers.
62. Ben-Zvi, A. and S. Liebner, *Developmental regulation of barrier-and non-barrier blood vessels in the CNS*. Journal of Internal Medicine, 2021.
63. Abbott, N.J., L. Rönnbäck, and E. Hansson, *Astrocyte–endothelial interactions at the blood–brain barrier*. Nature reviews neuroscience, 2006. **7**(1): p. 41-53.
64. Shepro, D. and N.M. Morel, *Pericyte physiology*. The FASEB Journal, 1993. **7**(11): p. 1031-1038.
65. Armulik, A., et al., *Pericytes regulate the blood–brain barrier*. Nature, 2010. **468**(7323): p. 557-561.
66. Dohgu, S., et al., *Brain pericytes contribute to the induction and up-regulation of blood–brain barrier functions through transforming growth factor- $\beta$  production*. Brain research, 2005. **1038**(2): p. 208-215.
67. Hori, S., et al., *A pericyte-derived angiopoietin-1 multimeric complex induces occludin gene expression in brain capillary endothelial cells through Tie-2 activation in vitro*. Journal of neurochemistry, 2004. **89**(2): p. 503-513.
68. Yurchenco, P.D. and J.C. Schittny, *Molecular architecture of basement membranes*. The FASEB Journal, 1990. **4**(6): p. 1577-1590.
69. Kim, S.-H., J. Turnbull, and S. Guimond, *Extracellular matrix and cell signalling: the dynamic cooperation of integrin, proteoglycan and growth factor receptor*. The Journal of endocrinology, 2011. **209**(2): p. 139-151.
70. MALINDA, K.M., et al., *Identification of laminin  $\alpha 1$  and  $\beta 1$  chain peptides active for endothelial cell adhesion, tube formation, and aortic sprouting*. The FASEB Journal, 1999. **13**(1): p. 53-62.
71. Durbeej, M., *Laminins*. Cell and tissue research, 2010. **339**(1): p. 259-268.
72. Yousif, L.F., J. Di Russo, and L. Sorokin, *Laminin isoforms in endothelial and perivascular basement membranes*. Cell adhesion & migration, 2013. **7**(1): p. 101-110.
73. Hohenester, E. and P.D. Yurchenco, *Laminins in basement membrane assembly*. Cell adhesion & migration, 2013. **7**(1): p. 56-63.
74. Sixt, M., et al., *Endothelial cell laminin isoforms, laminins 8 and 10, play decisive roles in T cell recruitment across the blood–brain barrier in experimental autoimmune encephalomyelitis*. The Journal of cell biology, 2001. **153**(5): p. 933-946.
75. Stratman, A.N., et al., *Pericyte recruitment during vasculogenic tube assembly stimulates endothelial basement membrane matrix formation*. Blood, The Journal of the American Society of Hematology, 2009. **114**(24): p. 5091-5101.
76. Aumailley, M. and N. Smyth, *The role of laminins in basement membrane function*. Journal of anatomy, 1998. **193**(1): p. 1-21.
77. Gautam, J., X. Zhang, and Y. Yao, *The role of pericytic laminin in blood brain barrier integrity maintenance*. Scientific reports, 2016. **6**(1): p. 1-13.

78. Wei, Y., et al., *Hyaluronic acid hydrogels with IKVAV peptides for tissue repair and axonal regeneration in an injured rat brain*. Biomedical Materials, 2007. **2**(3): p. S142.
79. Pöschl, E., et al., *Collagen IV is essential for basement membrane stability but dispensable for initiation of its assembly during early development*. Development, 2004. **131**(7): p. 1619-1628.
80. Tilling, T., et al., *Basement membrane proteins influence brain capillary endothelial barrier function in vitro*. Journal of neurochemistry, 1998. **71**(3): p. 1151-1157.
81. Song, J., et al., *Endothelial basement membrane laminin 511 contributes to endothelial junctional tightness and thereby inhibits leukocyte transmigration*. Cell reports, 2017. **18**(5): p. 1256-1269.
82. Song, J., et al., *Extracellular matrix of secondary lymphoid organs impacts on B-cell fate and survival*. Proceedings of the National Academy of Sciences, 2013. **110**(31): p. E2915-E2924.
83. Yao, Y., et al., *Astrocytic laminin regulates pericyte differentiation and maintains blood brain barrier integrity*. Nature communications, 2014. **5**(1): p. 1-12.
84. Miyagoe, Y., et al., *Laminin  $\alpha 2$  chain-null mutant mice by targeted disruption of the Lama2 gene: a new model of merosin (laminin 2)-deficient congenital muscular dystrophy*. FEBS letters, 1997. **415**(1): p. 33-39.
85. Chen, Z.-L., et al., *Ablation of astrocytic laminin impairs vascular smooth muscle cell function and leads to hemorrhagic stroke*. Journal of Cell Biology, 2013. **202**(2): p. 381-395.
86. Menezes, M.J., et al., *The extracellular matrix protein laminin  $\alpha 2$  regulates the maturation and function of the blood-brain barrier*. Journal of Neuroscience, 2014. **34**(46): p. 15260-15280.
87. Negah, S.S., et al., *Transplantation of human meningioma stem cells loaded on a self-assembling peptide nanoscaffold containing IKVAV improves traumatic brain injury in rats*. Acta biomaterialia, 2019. **92**: p. 132-144.
88. Nomizu, M., et al., *Structure-activity study of a laminin  $\alpha 1$  chain active peptide segment Ile-Lys-Val-Ala-Val (IKVAV)*. FEBS letters, 1995. **365**(2-3): p. 227-231.
89. Edgar, D., R. Timpl, and H. Thoenen, *The heparin-binding domain of laminin is responsible for its effects on neurite outgrowth and neuronal survival*. The EMBO journal, 1984. **3**(7): p. 1463-1468.
90. Lin, X., et al., *Enhancement of cell attachment and tissue integration by a IKVAV containing multi-domain peptide*. Biochimica et Biophysica Acta (BBA)-General Subjects, 2006. **1760**(9): p. 1403-1410.
91. Grant, D.S., et al., *Interaction of endothelial cells with a laminin A chain peptide (SIKVAV) in vitro and induction of angiogenic behavior in vivo*. Journal of cellular physiology, 1992. **153**(3): p. 614-625.
92. Nakamura, M., et al., *Promotion of angiogenesis by an artificial extracellular matrix protein containing the laminin-1-derived IKVAV sequence*. Bioconjugate chemistry, 2009. **20**(9): p. 1759-1764.
93. Dean III, J.W., K.C. Culbertson, and A.M. D'Angelo, *Fibronectin and laminin enhance gingival cell attachment to dental implant surfaces in vitro*. International Journal of Oral & Maxillofacial Implants, 1995. **10**(6).

94. Zollinger, A.J. and M.L. Smith, *Fibronectin, the extracellular glue*. Matrix Biology, 2017. **60**: p. 27-37.
95. Pankov, R. and K.M. Yamada, *Fibronectin at a glance*. Journal of cell science, 2002. **115**(20): p. 3861-3863.
96. Patten, J. and K. Wang, *Fibronectin in development and wound healing*. Advanced Drug Delivery Reviews, 2020.
97. Gui, L., et al., *Identification of the heparin-binding determinants within fibronectin repeat IIII*. Journal of Biological Chemistry, 2006. **281**(46): p. 34816-34825.
98. Sottile, J. and D.C. Hocking, *Fibronectin polymerization regulates the composition and stability of extracellular matrix fibrils and cell-matrix adhesions*. Molecular biology of the cell, 2002. **13**(10): p. 3546-3559.
99. Erat, M.C., et al., *Implications for collagen binding from the crystallographic structure of fibronectin 6FnII–2FnII7FnI*. Journal of Biological Chemistry, 2010. **285**(44): p. 33764-33770.
100. Alam, N., et al., *The integrin—growth factor receptor duet*. Journal of cellular physiology, 2007. **213**(3): p. 649-653.
101. Ruoslahti, E., *Fibronectin and its receptors*. Annual review of biochemistry, 1988. **57**: p. 375-413.
102. Ruoslahti, E., *RGD and other recognition sequences for integrins*. Annual review of cell and developmental biology, 1996. **12**(1): p. 697-715.
103. Hautanen, A., et al., *Effects of modifications of the RGD sequence and its context on recognition by the fibronectin receptor*. Journal of Biological Chemistry, 1989. **264**(3): p. 1437-1442.
104. Baneyx, G., L. Baugh, and V. Vogel, *Coexisting conformations of fibronectin in cell culture imaged using fluorescence resonance energy transfer*. Proceedings of the National Academy of Sciences, 2001. **98**(25): p. 14464-14468.
105. Ohashi, T., D.P. Kiehart, and H.P. Erickson, *Dynamics and elasticity of the fibronectin matrix in living cell culture visualized by fibronectin—green fluorescent protein*. Proceedings of the National Academy of Sciences, 1999. **96**(5): p. 2153-2158.
106. Wang, J. and R. Milner, *Fibronectin promotes brain capillary endothelial cell survival and proliferation through  $\alpha 5\beta 1$  and  $\alpha v\beta 3$  integrins via MAP kinase signalling*. Journal of neurochemistry, 2006. **96**(1): p. 148-159.
107. George, E.L., et al., *Defects in mesoderm, neural tube and vascular development in mouse embryos lacking fibronectin*. Development, 1993. **119**(4): p. 1079-1091.
108. Pasqualini, R., E. Koivunen, and E. Ruoslahti, *A peptide isolated from phage display libraries is a structural and functional mimic of an RGD-binding site on integrins*. The Journal of cell biology, 1995. **130**(5): p. 1189-1196.
109. Hudson, B., S.T. Reeder, and K. Tryggvason, *Type IV collagen: structure, gene organization, and role in human diseases: molecular basis of Goodpasture and Alport syndromes and diffuse leiomyomatosis*. The Journal of biological chemistry (Print), 1993. **268**(35): p. 26033-26036.
110. Sado, Y., et al., *Organization and expression of basement membrane collagen IV genes and their roles in human disorders*. The Journal of Biochemistry, 1998. **123**(5): p. 767-776.

111. Paulsson, M., *Basement membrane proteins: structure, assembly, and cellular interactions*. Critical reviews in biochemistry and molecular biology, 1992. **27**(1-2): p. 93-127.
112. Thomsen, M.S., et al., *Synthesis and deposition of basement membrane proteins by primary brain capillary endothelial cells in a murine model of the blood–brain barrier*. Journal of neurochemistry, 2017. **140**(5): p. 741-754.
113. Gould, D.B., et al., *Role of COL4A1 in small-vessel disease and hemorrhagic stroke*. New England Journal of Medicine, 2006. **354**(14): p. 1489-1496.
114. Alamowitch, S., et al., *Cerebrovascular disease related to COL4A1 mutations in HANAC syndrome*. Neurology, 2009. **73**(22): p. 1873-1882.
115. Dong, L., et al., *Neurologic defects and selective disruption of basement membranes in mice lacking entactin-1/nidogen-1*. Laboratory investigation, 2002. **82**(12): p. 1617-1630.
116. Kang, S.H. and J.M. Kramer, *Nidogen is nonessential and not required for normal type IV collagen localization in Caenorhabditis elegans*. Molecular biology of the cell, 2000. **11**(11): p. 3911-3923.
117. Bader, B.L., et al., *Compound genetic ablation of nidogen 1 and 2 causes basement membrane defects and perinatal lethality in mice*. Molecular and cellular biology, 2005. **25**(15): p. 6846-6856.
118. Mokkaapati, S., et al., *Basement membranes in skin are differently affected by lack of nidogen 1 and 2*. Journal of Investigative Dermatology, 2008. **128**(9): p. 2259-2267.
119. Wolburg, H., et al., *Agrin, aquaporin-4, and astrocyte polarity as an important feature of the blood-brain barrier*. The Neuroscientist, 2009. **15**(2): p. 180-193.
120. Burgess, R.W., W.C. Skarnes, and J.R. Sanes, *Agrin isoforms with distinct amino termini: differential expression, localization, and function*. The Journal of cell biology, 2000. **151**(1): p. 41-52.
121. Barber, A.J. and E. Lieth, *Agrin accumulates in the brain microvascular basal lamina during development of the blood-brain barrier*. Developmental dynamics: an official publication of the American Association of Anatomists, 1997. **208**(1): p. 62-74.
122. Gesemann, M., et al., *Agrin is a high-affinity binding protein of dystroglycan in non-muscle tissue*. Journal of Biological Chemistry, 1998. **273**(1): p. 600-605.
123. Roberts, J., M.P. Kahle, and G.J. Bix, *Perlecan and the blood-brain barrier: beneficial proteolysis?* Frontiers in pharmacology, 2012. **3**: p. 155.
124. Göhring, W., et al., *Mapping of the binding of platelet-derived growth factor to distinct domains of the basement membrane proteins BM-40 and perlecan and distinction from the BM-40 collagen-binding epitope*. European journal of biochemistry, 1998. **255**(1): p. 60-66.
125. Hallmann, R., et al., *Expression and function of laminins in the embryonic and mature vasculature*. Physiological reviews, 2005. **85**(3): p. 979-1000.
126. Deguchi, Y., et al., *Internalization of basic fibroblast growth factor at the mouse blood–brain barrier involves perlecan, a heparan sulfate proteoglycan*. Journal of neurochemistry, 2002. **83**(2): p. 381-389.
127. Knox, S. and J. Whitelock, *Perlecan: how does one molecule do so many things?* Cellular and Molecular Life Sciences CMLS, 2006. **63**(21): p. 2435-2445.

128. Costell, M., et al., *Perlecan maintains the integrity of cartilage and some basement membranes*. The Journal of cell biology, 1999. **147**(5): p. 1109-1122.
129. Witt, K.A., et al., *Effects of hypoxia-reoxygenation on rat blood-brain barrier permeability and tight junctional protein expression*. American Journal of Physiology-Heart and Circulatory Physiology, 2003. **285**(6): p. H2820-H2831.
130. Fischer, S., et al., *Hypoxia induces permeability in brain microvessel endothelial cells via VEGF and NO*. American Journal of Physiology-Cell Physiology, 1999. **276**(4): p. C812-C820.
131. Mark, K.S., et al., *Nitric oxide mediates hypoxia-induced changes in paracellular permeability of cerebral microvasculature*. American Journal of Physiology-Heart and Circulatory Physiology, 2004. **286**(1): p. H174-H180.
132. Mark, K.S. and T.P. Davis, *Cerebral microvascular changes in permeability and tight junctions induced by hypoxia-reoxygenation*. American Journal of Physiology-Heart and Circulatory Physiology, 2002. **282**(4): p. H1485-H1494.
133. van Bruggen, N., et al., *VEGF antagonism reduces edema formation and tissue damage after ischemia/reperfusion injury in the mouse brain*. The Journal of clinical investigation, 1999. **104**(11): p. 1613-1620.
134. Abbott, N.J., *Inflammatory mediators and modulation of blood-brain barrier permeability*. Cellular and molecular neurobiology, 2000. **20**(2): p. 131-147.
135. Katsu, M., et al., *Hemoglobin-induced oxidative stress contributes to matrix metalloproteinase activation and blood-brain barrier dysfunction in vivo*. Journal of Cerebral Blood Flow & Metabolism, 2010. **30**(12): p. 1939-1950.
136. Mun-Bryce, S. and G.A. Rosenberg, *Matrix metalloproteinases in cerebrovascular disease*. Journal of Cerebral Blood Flow & Metabolism, 1998. **18**(11): p. 1163-1172.
137. Heo, J.H., et al., *Matrix metalloproteinases increase very early during experimental focal cerebral ischemia*. Journal of Cerebral Blood Flow & Metabolism, 1999. **19**(6): p. 624-633.
138. Brkic, M., et al., *Friends or foes: matrix metalloproteinases and their multifaceted roles in neurodegenerative diseases*. Mediators of inflammation, 2015. **2015**.
139. Ruhul Amin, A., et al., *Secretion of matrix metalloproteinase-9 by the proinflammatory cytokine, IL-1 $\beta$ : a role for the dual signalling pathways, Akt and Erk*. Genes to Cells, 2003. **8**(6): p. 515-523.
140. Rosell, A., et al., *MMP-9-positive neutrophil infiltration is associated to blood-brain barrier breakdown and basal lamina type iv collagen degradation during hemorrhagic transformation after human ischemic stroke*. Stroke, 2008. **39**(4): p. 1121-1126.
141. Abbruscato, T.J., et al., *Nicotine and cotinine modulate cerebral microvascular permeability and protein expression of ZO-1 through nicotinic acetylcholine receptors expressed on brain endothelial cells*. Journal of pharmaceutical sciences, 2002. **91**(12): p. 2525-2538.
142. Seleman, M., et al., *Impact of P-glycoprotein at the blood-brain barrier on the uptake of heroin and its main metabolites: behavioral effects and consequences on the transcriptional responses and reinforcing properties*. Psychopharmacology, 2014. **231**(16): p. 3139-3149.
143. He, J. and F.T. Crews, *Increased MCP-1 and microglia in various regions of the human alcoholic brain*. Experimental neurology, 2008. **210**(2): p. 349-358.

144. Pimentel, E., et al., *Effects of drugs of abuse on the blood-brain barrier: a brief overview*. *Frontiers in Neuroscience*, 2020. **14**.
145. Rosenberg, G.A., *Neurological diseases in relation to the blood–brain barrier*. *Journal of Cerebral Blood Flow & Metabolism*, 2012. **32**(7): p. 1139-1151.
146. Cucullo, L., et al., *The role of shear stress in Blood-Brain Barrier endothelial physiology*. *BMC neuroscience*, 2011. **12**(1): p. 1-15.
147. Naik, P. and L. Cucullo, *In vitro blood–brain barrier models: current and perspective technologies*. *Journal of pharmaceutical sciences*, 2012. **101**(4): p. 1337-1354.
148. Neuhaus, W., et al., *A novel flow based hollow-fiber blood–brain barrier in vitro model with immortalised cell line PBMEC/C1–2*. *Journal of biotechnology*, 2006. **125**(1): p. 127-141.
149. Griep, L.M., et al., *BBB on chip: microfluidic platform to mechanically and biochemically modulate blood-brain barrier function*. *Biomedical microdevices*, 2013. **15**(1): p. 145-150.
150. Booth, R. and H. Kim, *Characterization of a microfluidic in vitro model of the blood-brain barrier ( $\mu$ BBB)*. *Lab on a Chip*, 2012. **12**(10): p. 1784-1792.
151. Augustine, R., et al., *Gelatin-Methacryloyl Hydrogel based in vitro blood brain barrier model for studying breast cancer associated brain metastasis*. *Pharmaceutical Development and Technology*, 2021: p. 1-26.
152. Khan, F., et al., *Versatile biocompatible polymer hydrogels: scaffolds for cell growth*. *Angewandte Chemie International Edition*, 2009. **48**(5): p. 978-982.
153. Billiet, T., et al., *A review of trends and limitations in hydrogel-rapid prototyping for tissue engineering*. *Biomaterials*, 2012. **33**(26): p. 6020-6041.
154. Hoffman, A.S., *Hydrogels for biomedical applications*. *Advanced drug delivery reviews*, 2012. **64**: p. 18-23.
155. Chai, Q., Y. Jiao, and X. Yu, *Hydrogels for biomedical applications: their characteristics and the mechanisms behind them*. *Gels*, 2017. **3**(1): p. 6.
156. Thomson, R., et al., *Biodegradable polymer scaffolds to regenerate organs*. *Biopolymers* *ii*, 1995: p. 245-274.
157. Wong, W.H. and D.J. Mooney, *Synthesis and properties of biodegradable polymers used as synthetic matrices for tissue engineering*, in *Synthetic biodegradable polymer scaffolds*. 1997, Springer. p. 51-82.
158. Lee, K.Y. and D.J. Mooney, *Hydrogels for tissue engineering*. *Chemical reviews*, 2001. **101**(7): p. 1869-1880.
159. Ratner, B.D., et al., *Biomaterials science: an introduction to materials in medicine*. 2004: Elsevier.
160. Karimi, Z., L. Karimi, and H. Shokrollahi, *Nano-magnetic particles used in biomedicine: Core and coating materials*. *Materials Science and Engineering: C*, 2013. **33**(5): p. 2465-2475.
161. Hinds, K., *Protein conjugation, cross-linking, and PEGylation*. *biomaterials for Delivery and Targeting of Proteins and Nucleic Acids*, 2005: p. 119-185.
162. Filpula, D. and H. Zhao, *Releasable PEGylation of proteins with customized linkers*. *Advanced drug delivery reviews*, 2008. **60**(1): p. 29-49.
163. Suk, J.S., et al., *PEGylation as a strategy for improving nanoparticle-based drug and gene delivery*. *Advanced drug delivery reviews*, 2016. **99**: p. 28-51.

164. Lutolf, M. and J. Hubbell, *Synthesis and physicochemical characterization of end-linked poly (ethylene glycol)-co-peptide hydrogels formed by Michael-type addition*. *Biomacromolecules*, 2003. **4**(3): p. 713-722.
165. Tan, H., et al., *Novel multiarm PEG-based hydrogels for tissue engineering*. *Journal of Biomedical Materials Research Part A: An Official Journal of The Society for Biomaterials, The Japanese Society for Biomaterials, and The Australian Society for Biomaterials and the Korean Society for Biomaterials*, 2010. **92**(3): p. 979-987.
166. Ranganathan, N., et al., *Synthesis and properties of hydrogels prepared by various polymerization reaction systems*. Springer International Publishing: Cham, Switzerland, 2018.
167. Zalipsky, S., *Functionalized poly (ethylene glycols) for preparation of biologically relevant conjugates*. *Bioconjugate chemistry*, 1995. **6**(2): p. 150-165.
168. Metters, A. and J. Hubbell, *Network formation and degradation behavior of hydrogels formed by Michael-type addition reactions*. *Biomacromolecules*, 2005. **6**(1): p. 290-301.
169. Park, Y., et al., *Bovine primary chondrocyte culture in synthetic matrix metalloproteinase-sensitive poly (ethylene glycol)-based hydrogels as a scaffold for cartilage repair*. *Tissue engineering*, 2004. **10**(3-4): p. 515-522.
170. Han, J., J.-O. Park, and S. Park, *Development of active controllable tumor targeting bacteriobot*, in *Microbiorobotics*. 2017, Elsevier. p. 39-60.
171. Sigma-Aldrich. *4arm-PEG20K-Vinylsulfone*. 2021; Available from: <https://www.sigmaaldrich.com/catalog/product/aldrich/jka7025?lang=en&region=LB>.
172. Russell, L.N. and K.J. Lampe, *Oligodendrocyte precursor cell viability, proliferation, and morphology is dependent on mesh size and storage modulus in 3D poly (ethylene glycol)-based hydrogels*. *ACS Biomaterials Science & Engineering*, 2017. **3**(12): p. 3459-3468.
173. Zustiak, S.P., et al., *Hydrolytically degradable poly (ethylene glycol) hydrogel scaffolds as a cell delivery vehicle: characterization of PC12 cell response*. *Biotechnology progress*, 2013. **29**(5): p. 1255-1264.
174. Lam, J., et al., *Hydrogel design of experiments methodology to optimize hydrogel for iPSC-NPC culture*. *Advanced healthcare materials*, 2015. **4**(4): p. 534-539.
175. Tran, S.-L., et al., *Trypan blue dye enters viable cells incubated with the pore-forming toxin HlyII of Bacillus cereus*. *PloS one*, 2011. **6**(9): p. e22876.
176. Sarina Harris Ma, et al., *An endothelial and astrocyte co-culture model of the blood–brain barrier utilizing an ultra-thin, nanofabricated silicon nitride membrane*. *Lab on a Chip*, 2005.
177. Decherchi, P., P. Cochard, and P. Gauthier, *Dual staining assessment of Schwann cell viability within whole peripheral nerves using calcein-AM and ethidium homodimer*. *Journal of neuroscience methods*, 1997. **71**(2): p. 205-213.
178. Maryam Amini, Jonny Hisdal, and H. Kalvøy, *Applications of Bioimpedance Measurement Techniques in Tissue Engineering*. *Journal of Electrical Bioimpedance*, 2018.
179. Kozler, P. and J. Pokorny, *Altered blood-brain barrier permeability and its effect on the distribution of Evans blue and sodium fluorescein in the rat brain*



- applied by intracarotid injection. *Physiological research*, 2003. **52**(5): p. 607-614.
180. Saunders, N.R., et al., *Markers for blood-brain barrier integrity: how appropriate is Evans blue in the twenty-first century and what are the alternatives?* *Frontiers in neuroscience*, 2015. **9**: p. 385.
  181. Smith, R., et al., *Diagnostic Approaches Techniques in Concussion/Mild Traumatic Brain Injury: Where are we?*, in *Neurosensory Disorders in Mild Traumatic Brain Injury*. 2019, Elsevier. p. 247-277.
  182. Jongpaiboonkit, L., W.J. King, and W.L. Murphy, *Screening for 3D environments that support human mesenchymal stem cell viability using hydrogel arrays*. *Tissue Engineering Part A*, 2009. **15**(2): p. 343-353.
  183. Gronthos, S., et al., *Integrin-mediated interactions between human bone marrow stromal precursor cells and the extracellular matrix*. *Bone*, 2001. **28**(2): p. 174-181.
  184. Hassan, W., Y. Dong, and W. Wang, *Encapsulation and 3D culture of human adipose-derived stem cells in an in-situ crosslinked hybrid hydrogel composed of PEG-based hyperbranched copolymer and hyaluronic acid*. *Stem cell research & therapy*, 2013. **4**(2): p. 1-11.
  185. Macarak, E. and P. Howard, *Adhesion of endothelial cells to extracellular matrix proteins*. *Journal of cellular physiology*, 1983. **116**(1): p. 76-86.
  186. Salasznyk, R.M., et al., *Adhesion to vitronectin and collagen I promotes osteogenic differentiation of human mesenchymal stem cells*. *Journal of Biomedicine and Biotechnology*, 2004. **2004**(1): p. 24-34.
  187. Nuttelman, C.R., M.C. Tripodi, and K.S. Anseth, *Synthetic hydrogel niches that promote hMSC viability*. *Matrix biology*, 2005. **24**(3): p. 208-218.
  188. Zhang, Y., et al., *Porcine brain microvessel endothelial cells as an in vitro model to predict in vivo blood-brain barrier permeability*. *Drug metabolism and disposition*, 2006. **34**(11): p. 1935-1943.
  189. Lee, S.-W., et al., *SSECKS regulates angiogenesis and tight junction formation in blood-brain barrier*. *Nature medicine*, 2003. **9**(7): p. 900-906.
  190. Hawkins, B.T., S. Grego, and K.L. Sellgren, *Three-dimensional culture conditions differentially affect astrocyte modulation of brain endothelial barrier function in response to transforming growth factor  $\beta$ 1*. *Brain research*, 2015. **1608**: p. 167-176.
  191. Cai, Y., et al., *TGF- $\beta$ 1 prevents blood-brain barrier damage and hemorrhagic transformation after thrombolysis in rats*. *Experimental neurology*, 2015. **266**: p. 120-126.
  192. Hamann, G.F., et al., *Mild to moderate hypothermia prevents microvascular basal lamina antigen loss in experimental focal cerebral ischemia*. *Stroke*, 2004. **35**(3): p. 764-769.
  193. Wang, C.X. and A. Shuaib, *Critical role of microvasculature basal lamina in ischemic brain injury*. *Progress in neurobiology*, 2007. **83**(3): p. 140-148.
  194. Wu, J., et al., *Ang-(1-7) exerts protective role in blood-brain barrier damage by the balance of TIMP-1/MMP-9*. *European journal of pharmacology*, 2015. **748**: p. 30-36.
  195. DEL ZOPPO, G.J., R. VON KUMMER, and G.F. HAMANN, *Ischaemic damage of brain microvessels: inherent risks for thrombolytic treatment in stroke*. *Journal of Neurology, Neurosurgery & Psychiatry*, 1998. **65**(1): p. 1-9.

196. Gardner, T.W., et al., *Astrocytes increase barrier properties and ZO-1 expression in retinal vascular endothelial cells*. Investigative ophthalmology & visual science, 1997. **38**(11): p. 2423-2427.
197. Almutairi, M.M., et al., *Factors controlling permeability of the blood–brain barrier*. Cellular and molecular life sciences, 2016. **73**(1): p. 57-77.
198. Gaillard, P.J., et al., *Establishment and functional characterization of an in vitro model of the blood–brain barrier, comprising a co-culture of brain capillary endothelial cells and astrocytes*. European journal of pharmaceutical sciences, 2001. **12**(3): p. 215-222.
199. Bang, M., et al., *Late Passage Cultivation Induces Aged Astrocyte Phenotypes in Rat Primary Cultured Cells*. Biomolecules & Therapeutics, 2021. **29**(2): p. 144.
200. Balasubramanian, S., et al., *Three-dimensional environment sustains morphological heterogeneity and promotes phenotypic progression during astrocyte development*. Tissue Engineering Part A, 2016. **22**(11-12): p. 885-898.
201. Nitta, T., et al., *Size-selective loosening of the blood-brain barrier in claudin-5–deficient mice*. The Journal of cell biology, 2003. **161**(3): p. 653-660.

